Title

Characterization of a Nylon-6/Gaseous Oxygen Hybrid Rocket Performance with Hydrogen versus Methane-Based Torch Igniter System

Author

Gonzalez, Ricardo Emmanuel

Publication Date

2024

Peer reviewed|Thesis/dissertation

Characterization of a Nylon-6/Gaseous Oxygen Hybrid Rocket Performance with Hydrogen versus Methane-Based Torch Igniter System

By

Ricardo Emmanuel Gonzalez

Thesis

Submitted in partial satisfaction of the requirements for the degree of

Master of Science

in

Mechanical and Aerospace Engineering

in the

Office of Graduate Studies

of the

University of California

Davis

Approved:

Paul Erickson, Chair

Zahra Sadeghizadeh

Francis Assadian

Committee in Charge

2024

Contents

List of Figures

List of Tables

Abstract

Characterization of a Nylon-6/Gaseous Oxygen Hybrid Rocket Performance with Hydrogen versus Methane-Based Torch Igniter System

Hybrid rockets have recently become a more and more desirable method for small satellite propulsion, due to their lack of safety issues compared to their liquid and solid rocket counterparts. A major reason for this is because the fuel and oxidizer are both separated by distance and state when stored in a hybrid rocket. This also makes it relatively more difficult to ignite and start up the rocket. While many igniter systems have been invented, currently no reliable, self-igniting system has been flown. Recently, a Hydrogen-Oxygen torch was designed, built, and tested in UC Davis' Energy Research Lab. Methane is typically used in torch igniters for lab-scale testing of hybrid rocket motors. A side-by-side comparison on the same igniter system between Hydrogen and Methane as the igniter fuel was done to investigate which, if any, fuel can exhibit better transient and/or steady state performance. Due to the higher heat of combustion, adiabatic flame temperatures and theoretical characteristic exhaust velocities when reacting with Oxygen, Hydrogen was found to have more reliable and repeatable ignition transients. The solid fuel regression rates were also found to be higher when using Hydrogen despite competition to burn with Oxygen between Hydrogen and the solid Nylon-6 fuel. These performance benefits come at the cost of being less volumetrically efficient than Methane as Hydrogen has a significantly smaller density at a given temperature and pressure.

Acknowledgments

From the initial literature review, project planning, designing the experiment, to building and running the experiment, and writing the thesis presented here, seeing this project through to the end was no easy undertaking, and certainly not possible without the help of those mentioned here.

First and foremost, I would like to acknowledge and thank my advising professor, Dr. Paul A. Erickson. He never failed to provide technical insight and support when I needed it and provided helpful advice throughout the entire process. His contributions extend beyond the academic realm, by making sure I, and my fellow labmates, always remember to take breaks, enjoy life, and not lose our way during our academic pursuits.

This work would not have been possible by the person who started it all, Kellen K. Ochi. Not only was he the (former) student who first started the hybrid rocket research campaign in the Energy Research Lab, he also provided invaluable support, having gone through this entire process first and with no predecessor. Much of the rocket hardware used in this experiment was designed by him, taking an enormous workload off and enabling the study contained in this thesis.

Next, I would like to thank the rest of the past and current Energy Research Lab members for their contributions in helping to build, troubleshoot, and run the experiment infrastructure and hardware. Austin Cameron, Armando Gomez Hernandez, Chibuike Agba, Michael Horton, Allyson Clague, Hieu Bui, Yen Chun Chou, and the rest of the Energy Research Lab members not named here, their contributions allowed the rocket to feel the warmth of its flames and for me to feel the warmth of their generosity. This is indeed not "my rocket" nor "Ricky's" rocket, but OUR rocket.

As has already been shown "it takes a village". That is what the Diane Bryant Engineering Student Design Center (ESDC) manager Jose Mojica said when I acknowledged his leadership during the remodeling and set up of the new workshop. Likewise he and the rest of staff of the ESDC, David Kehlet, Joshua Ira, and Michael Fish are part of the "village" for this project. They provided assistance, tools, and manufacturing wisdom that supported this project in a way that no one else at the university could.

I would like to thank all the students I had the pleasure of teaching during my time as a Teaching Assistant. Some say the best way to learn is to teach. I certainly learned a lot from my students and, more importantly, they provided me with the motivation to keep going when difficulties presented themselves.

I would also like to thank the rest of the committee members, professors Francis Assadian and Zahra Sadeghizadeh, for their time and effort in following the project and reviewing the final thesis manuscript.

Finally, these acknowledgements would not be complete without mention of my friends and family, for not only encouraging me to keep going and initiating discussions about the research but also for making lasting memories and making my graduate school experience some of the best days of my life so far.

Nomenclature

Physical Variables

Δm_f	Fuel Grain Mass Change, kg
$\dot{m}$	Mass Flow Rate, $\frac{kg}{sec}$
$\dot{m}_f$	Fuel Mass Flow Rate, $\frac{kg}{sec}$
$\dot{m}_{ox}$	Oxidizer Mass Flow Rate, $\frac{kg}{sec}$
$\dot{r}$	Regression Rate, $\frac{cm}{sec}$
$\overline{\dot{m}_{ox}}$	Time-Averaged Oxidizer Mass Flow Rate, $\frac{kg}{sec}$
$\overline{\dot{m}}_p$	Time-Averaged Propellant Mass Flow Rate, $\frac{kg}{sec}$
$\overline{\dot{r}}$	Time-Space Averaged Regression Rate, $\frac{cm}{sec}$
$\overline{G_{ox}}$	Time-Space Averaged Oxidizer Mass Flux, $\frac{kg}{m^2 sec}$
$\overline{P}_o$	Time-Averaged Combustion Chamber Pressure, Pa
ϕ	Equivalence Ratio
ρ_f	Solid Fuel Density, $\frac{kg}{m^3}$
τ	First Order System Time Constant, sec
A_e	Nozzle Exit Area, m^2
a_o	Regression Rate Scale Factor, $\frac{cm^{3n} sec^{n-1}}{kg^n}$
A_t	Nozzle Throat Area, m^2
c^*	Characteristic Exhaust Velocity of Propellants, $\frac{m}{sec}$
C_f	Thrust Coefficient

D	Digitally-Mapped Data Output Value
F	Thrust Force, N
G	Signal Gain
g_o	Earth Gravity Acceleration, $\frac{m}{sec^2}$
G_{ox}	Oxidizer Mass Flux, $\frac{kg}{m^2 sec}$
I_{sp}	Specific Impulse, sec
k	Ratio of Specific Heats
K_a	Flow Meter K-factor
K_c	Transducer Voltage to Unit Conversion Factor, unit/V
L	Fuel Grain Length, m
m_p	Propellant Mass Consumed, kg
Ma_e	Nozzle Exit Mach Number
n	Regression Rate Burn Exponent
P_a	Ambient Pressure, Pa
P_e	Exit Pressure, Pa
P_o	Combustion Chamber Pressure, Pa
q	Pressure-Based Regression Rate Burn Exponent
R	Gas Constant, $\frac{J}{kgK}$
r	Instantaneous Fuel Port Radius, m
r_f	Final Fuel Port Radius, m
r_i	Initial Fuel Port Radius, m

S_L Laminar Flame Speed, cm/sec

t Time, sec

t_b Burn Time, sec

T_o Combustion Chamber Temperature, K

v_e Exit Velocity, $\frac{m}{sec}$

V_r Voltage Range, V

Chemical Species

ABS Acrylonitrile Butadiene Styrene

CH_4 Methane

GO_x Gaseous Oxygen

H_2 Hydrogen

HDPE High-Density Polyethylene

HP Hydrogen Peroxide

HTPB Hydroxyl-Terminated Polybutadiene

LO_x Liquid Oxygen

N_2O Nitrous Oxide

PMMA Poly-methyl Methacrylate

Chapter 1

Introduction

1.1 General Rocket Principles

1.1.1 Fundamental Mechanics

Rockets rely on Newton's second law in order to create the thrust used to propel the vehicle and its payload forward. Propellant is brought to a high pressure through a chemical reaction, usually combustion between a fuel and an oxidizer, and expanded through a nozzle to be ejected out of the vehicle at supersonic velocities[1]. The equal and opposite force imparted on the exiting propellant is experienced by the rocket and this reaction force is what becomes the thrust.

According to the rocket equation

$$F = \dot{m}v_e + (P_e - P_a)A_e \tag{1.1}$$

the total thrust, F, is generated from two mechanisms, the momentum of the exiting propellants, or exhaust, and the pressure difference between the nozzle exit pressure and ambient pressure. The first term of the rocket equation includes the propellant exit velocity, v_e and total propellant mass flow rate, $\dot{m}$. With the understanding that a force is simply the time derivative of the momentum of a system, the multiplication of these two terms is the change in momentum of the propellants and accordingly called the momentum thrust. The second term of the rocket equation includes static pressure of the propellants at the nozzle exit (P_e), ambient pressure (P_a), and nozzle exit area (A_e). When the two pressures are not equal, the pressure difference creates a force of which the magnitude

is the product of the nozzle exit area and the pressure difference. As shown in equation 1.1 when the ambient pressure is smaller than nozzle exit pressure, the pressure thrust contribution is in the same direction as the momentum thrust.

A simple analysis of the rocket equation with varying the ambient pressure values or nozzle exit areas while obeying adiabatic and isentropic flow in the nozzle shows that the maximum thrust is achieved when the pressure thrust contribution is zero. Considering this, rocket engine designers must consider the environment in which the engine will be used. For example, for launch vehicle systems, the ambient pressure will be constantly decreasing as the vehicle increases its altitude and an optimal design point can therefore be difficult to find. However, for satellite propulsion systems in space, the ambient pressure will always be constant at vacuum and therefore an optimal design point is easier to find.

1.1.2 Design Considerations and Performance Metrics

Rockets are complex vehicles with many design considerations. Some commonly desired characteristics include high performance, storability of propellants, non-toxicity of propellants, safe to handle, and start, stop, restart, and throttle capabilities[1, 2]. When it comes to high performance, the rocket must first meet the design specifications. Of course with any engineering endeavor, the goal is to do so with an optimized design that can achieve the desired performance efficiently. For rocket motors, this means having a high thrust coefficient, specific impulse, and characteristic exhaust velocity, the meanings of which will be discussed in the next paragraph. Storability of propellants is also an important consideration because this can affect ground handling and transportation time and costs, design difficulty and complexity, and even selection of launch opportunities. To a similar extent, toxicity, or rather non-toxicity, of propellants is an important factor because this can also increase ground handling and transportation time and costs due to strict regulations. Toxic propellants can also yield harmful products in the combustion reaction that can have adverse effects on the environment. The storability and toxicity of propellants also tie into how safe it is to handle the rocket motor. Easily storable and non-toxic propellants are safer to handle, but also (where with respect to each other) the propellants are stored, and in what state they are stored in affect how safe it is to

handle the rocket. The location and state of propellants depend on the rocket configuration (solid, liquid, or hybrid) which will be discussed in more detail in the next section. Finally, start, stop, restart, and throttle capabilities are important especially for missions that require multiple firings and/or varying but precisely controlled thrust. The need for start, stop, and restart capabilities in small satellite propulsion applications is one of the fundamental reasons for the study being presented in this thesis.

As mentioned in the previous paragraph, high performing rockets should have a large thrust coefficient, specific impulse, and characteristic exhaust velocity. The thrust coefficient is essentially a measure of a nozzle's effectiveness in expanding the high-pressure combustion products and in turn increasing the exit velocity, and is given by equation 1.2

$$C_f = \frac{F}{A_t P_o} \tag{1.2}$$

where A_t is the nozzle throat area and P_o is the pressure in the combustion chamber. It should be noted that this is a simplified equation for the determination of thrust coefficient, but used when finding the value experimentally. The longer, theoretical version of the equation for which the one presented here is based off of, is a function of more variables such as the nozzle exit area, nozzle exit pressure, ratio of specific heats of exhaust gases, and more.

The specific impulse (Isp) is a measure of the motor effectiveness with respect to a unit mass of propellant consumed, synonymous to the miles per gallon of a car. It is the total impulse divided by the total mass of propellant used, given by equation 1.3

$$I_{sp} = \frac{\int F dt}{m_p g_o} \tag{1.3}$$

where m_p is the total mass of propellant (both fuel and oxidizer) consumed and g_o is $9.81 m/sec^2$. Even though rockets operating in outer space experience a different acceleration from Earth's gravity, the constant g_o remains the same value in order to maintain a normalized and comparable performance metric.

Lastly, and probably the most important measure of performance is the characteristic exhaust velocity, or c* (c-star). The c* is a measure of the propellants effectiveness in converting the potential chemical energy into kinetic energy, creating the high-pressure

and hot combustion products that propel the rocket. The c* is given by equation 1.4[1] and is independent of the nozzle geometry and is a better measure of the propellant performance, combustion chamber design and, for liquid and hybrid rockets, propellant injector design.

$$c^* = \frac{\sqrt{kRT_o}}{k\sqrt{\frac{2}{k+1}^{\frac{k+1}{k-1}}}} \tag{1.4}$$

In equation 1.4, k is the ratio of specific heats of the exhaust, R is the gas constant of the exhaust, and T_o is the combustion chamber temperature.

1.2 Hybrid vs Solid and Liquid Rockets

To begin narrowing the scope of this work, the three main rocket configurations will be discussed in the next section and introduced here. It was previously mentioned that propellant storability and how safe it is to handle the rocket motor depend largely on where and in what state the propellants are stored in. This also determines the rocket configuration, where in a liquid rocket engine the fuel and oxidizer are stored in the liquid state. As the name implies when the fuel and oxidizer stored as solids they make up a solid rocket motor. This work will focus on the use of hybrid rockets where the fuel or oxidizer is stored as a solid, and the other of the two is stored as a liquid or gas. The next section will provide a brief introduction to each of the three configurations and provide rationale for the selection of investigating the hybrid rocket configuration.

1.2.1 Solid and Liquid Rockets

In solid rocket motors, the fuel and oxidizer are both stored in the solid state. Because of this, the propellants are premixed into a solid cylindrical propellant grain and stored directly in the combustion chamber. Preselected and desired operating oxidizer to fuel ratios determine how much of each propellant is mixed into different regions of the propellant grain. The center of this propellant grain is hollow to allow the fuel and oxidizer to ablate, pyrolyze into gas, mix, and engage in the combustion reaction. This hollow volume is known as the combustion port. Only the propellant on the surface exposed to the combustion port can burn. The originally inert propellant grain is usually ignited

by a "one-shot" pyrotechnic charge and the resulting combustion reaction provides the activation energy to the rest of the propellant grain to maintain the combustion reaction throughout the duration of the burn. This method of propellant storage, ignition, and motor operation makes for mechanically simple vehicle designs as there is no need for pipes, valves, and other plumbing-related hardware to transport and/or pressurize the propellants. On the other hand, once propellant grain has been cast and set, it becomes dangerous to handle and transport since an accidental ignition by any means will cause the entire propellant grain to burn and potentially explode. The continuous burning until end of operation makes ignition a relatively easy one-time process, but makes throttling capabilities extremely limited and completely removes start, stop, restart capabilities except in rare cases where sections of the propellant grain are separated by structural members. Limited throttling capability can be achieved by carefully selecting an initial combustion port cross section shape so that the cross section shape, and thus amount of exposed propellant and resulting combustion reaction, creates a desired thrust profile.

In liquid rocket engines, the fuel and oxidizer are both stored in the liquid state. Unlike in solid rocket motors, the fuel and oxidizer are stored separately in tanks that need to support the propellant storage pressure and/or insulate the propellants if they need to be stored cryogenically. Since the propellants are not stored in the combustion chamber extra hardware for fluid lines are required, making the designs much more mechanically complex than solid rocket motors. This opens the door to a multitude of design decisions that need to be made, the most important of which is how the propellants will be brought to the desired chamber pressure from the storage tank pressures. Some liquid rocket engines rely on a completely pressure-fed system where the storage tanks are initially at a much larger pressure than the desired combustion chamber. This makes the fluid lines relatively more simple than engines that use turbomachinery to pressurize the propellants, but comes with reduced performance and heavier pressure-bearing hardware. For liquid rocket engines that use turbomachinery to bring the propellants up to the desired chamber pressure, the fluid lines become much more complex, and the designer is faced with deciding what combustion cycle to use. Different combustion cycles such as the expander cycle, or the

staged combustion cycle use different methods to power the turbomachinery, and preheat the propellants at different points in the fluid lines, if at all. A schematic of a basic liquid rocket engine with a simplified representation of turbomachinery, where the pumps are usually powered by turbines, is shown in figure 1.1. Propellant injector design to ensure proper mixing and atomization pose further design challenges. Further discussion about the design of liquid rocket engines is beyond the scope of this work.

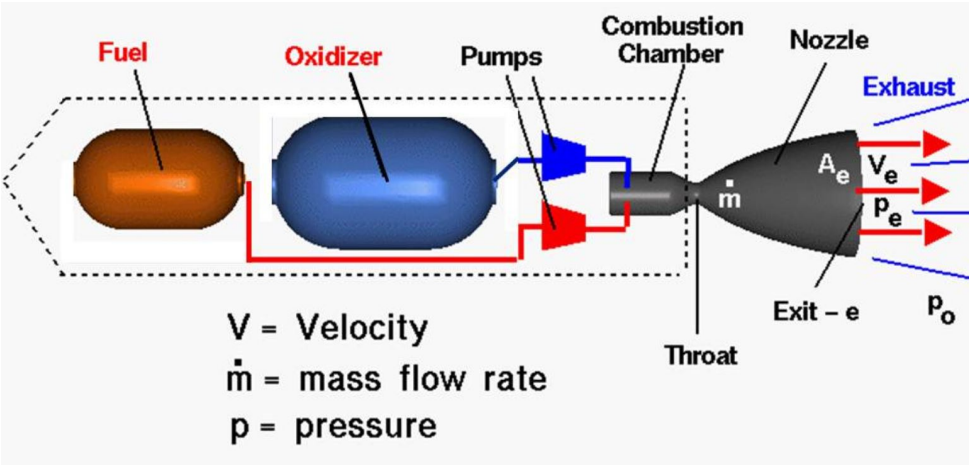

Figure 1.1. Schematic of Simplified Representation of Liquid Rocket Engine[3]

From what has been discussed, it can be seen that handling, transporting, and operating liquid rocket engines is just as, if not more, difficult than solid rocket motors. Highly pressurized propellants prone to leaking can cause unintended detonation and pose extreme explosion hazards. Where liquid rockets are advantageous over solid rocket motors is in the start, stop, restart, and throttle capabilities. The thrust can be varied by controlling the mass flow rate of propellants into the combustion chamber using control valves in the fluid lines. The valves being able to fully shut and then open again allow for full stop and restart capabilities.

1.2.2 Hybrid Rockets

The previous subsection will be used as the reference for what advantages and disadvantages utilizing hybrid rocket propulsion present. The most significant and obvious advantage that hybrid rocket motors have is the safety in ground handling and transportation, and in-situ operation. This is due to the fact that the fuel and oxidizer are

stored separately and in different states. The most common combination of propellant storage is a solid fuel grain in the combustion chamber with the oxidizer stored as a liquid or gas in a separate tank. Due to the rarity of the opposite configuration with a solid oxidizer grain and the fuel stored as a liquid or gas in a separate tank, this opposite configuration is commonly referred to as a "reverse hybrid rocket"[4].

Regardless of which propellant is in the solid or fluid state, this configuration requires less plumbing and pressure vessel hardware than a liquid rocket engine making the design more mechanically simple. Figure 1.2 shows a basic schematic of a pressure-fed hybrid rocket motor. This should be compared with figure 1.1. Of course, this means that the design is mechanically more complex than solid rocket motors which can be seen as the trade off cost for a safer motor. Furthermore, with the use of a control valve in the fluid propellant line, start, stop, restart, and throttle capabilities are possible. It has been found in the literature that hybrid motors can throttle over a larger range of thrust values when compared to liquid rocket engines of the same thrust class[5].

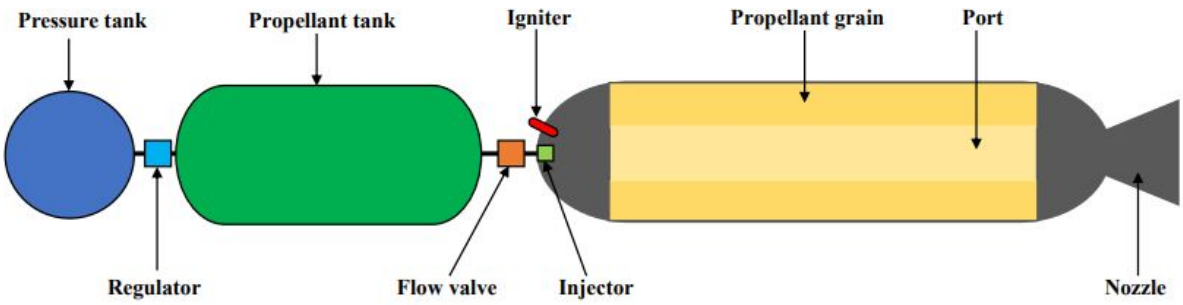

Figure 1.2. Schematic of Typical Pressure-Fed Hybrid Rocket Engine[6]

While hybrid motors present safety, design, and capability advantages, this comes at the price of reduced performance. For example, solid motors and liquid engines typically have a larger specific impulse of similarly sized hybrid motors. One reason for this is the reduced fuel regression rate observed in hybrid rocket motors which typically tends to be around 25-30% lower than solid rocket motors[1]. The regression rate, an important factor in determining performance, is the rate at which the surface exposed to the combustion port recedes or "regresses". This rate is expressed as distance per unit time that the

surface moves. Another downside is that while the carefully synthesized mixture in solid motors, and mass flow rate control through individual valve actuation in liquid engines allow for each to have direct control over the oxidizer to fuel ratio in the combustion reaction, this ratio changes over time as a result of the change in exposed fuel to the combustion port in hybrid motors. This is known as the oxidizer to fuel ratio shift phenomenon. Little research has been conducted in creating and implementing an oxidizer to fuel ratio and thrust control law with a more complex oxidizer injector resulting in a multiple input multiple output system[7] but this technology is still far from reaching maturity.

The discussion of hybrid rocket advantages and disadvantages compared to solid motors and liquid engines would not be complete without mentioning the ignition problem. The increased safety hybrid motors have, makes ignition incredibly more difficult and tackling this problem forms the purpose of this study. Meanwhile, with solid rocket motors, a single pyrotechnic charge is sufficient for the initial combustion of the propellant grain and in liquid rocket engines, the propellants expand into the gas phase and in some cases atomize as they pass through the injector and into the combustion chamber where a spark plug can easily ignite the mixture. Further technical discussion about igniting hybrid motors, as well as the oxidizer to fuel ratio shift phenomenon will be presented in the next chapter.

Figure 1.3 summarizes some of the differences and similarities between solid, liquid, and hybrid rockets in a Venn diagram.

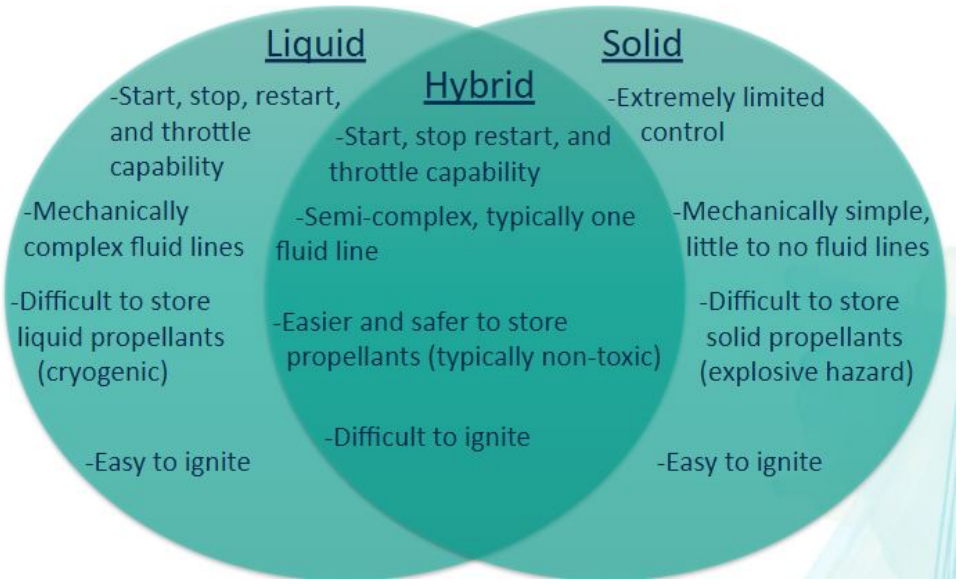

Figure 1.3. Venn Diagram of Qualitative Comparison of Solid, Liquid, and Hybrid Rockets

1.3 Hybrid Rocket Applications

Throughout the literature and in real missions flown, there are various applications for hybrid rocket motors. While they can be used for the same applications as their solid and liquid rocket counterparts, the advantages of hybrid rockets make them more suitable for some applications, while the disadvantages make liquid or solid rockets the better choice for other applications. In short, hybrid rocket motors can be used and/or have been used in launch vehicles, lander vehicles, and small satellite propulsion for various objectives.

1.3.1 Launch and Lander Vehicles

When it comes to launch vehicles, hybrid rocket-based launch vehicles are not nearly as common as launch vehicles powered by liquid or solid rockets. This is due to the reduced performance that hybrid rockets exhibit. This application of rocket propulsion typically requires the most amount of thrust output which can call for extremely large chamber pressures. In order to pressurize the combustion chamber, liquid rocket engines rely on complex combustion cycles, as described earlier, to power the turbomachinery that pressurizes the propellants. In a hybrid system, because only one propellant is stored in a liquid or gas state, there would be no way to power turbomachinery to bring it up to

pressure[4]. Extra propellant would be required to power the turbomachinery, or thicker and heavier tank and plumbing hardware would be necessary for a completely pressure fed system. That last point, coupled with the already reduced performance hybrid rockets have make liquid rocket engines the better choice for this application. Solid rocket motors operate with higher regression rates than hybrid rocket motors, which leads to higher thrust output.

This is not to say that hybrid rocket motors cannot be used to power launch vehicles on other planets or moons. A joint effort by NASA facilities at JPL, Marshall Space Flight Center, Langley, Ames, and White Sands Testing facility, as well as private companies, Whittinghill Aerospace, Space Propulsion Group, Parabilis Space Technologies, and the Aerospace Corporation, with Purdue University and Penn State University spent four years raising the technological readiness level of a Mars Ascent Vehicle (MAV) hybrid rocket propulsion system[8]. The final design as of the publishing of the referenced paper is shown in figure 1.4. Space Propulsion Group, Parabilis Space Technologies, and Marshall Space Flight Center all worked on design and characterization of the fuel grain by assessing feasibility of long term storage and harsh temperature conditions, conducting regression rate testing, and coming up with the casting method of the solid fuel grain. Meanwhile, Penn State and Purdue University developed and tested a hypergolic ignition system and Whittinghill Aerospace focused on the full scale vehicle design and designed a motor to meet the vehicle's requirements.

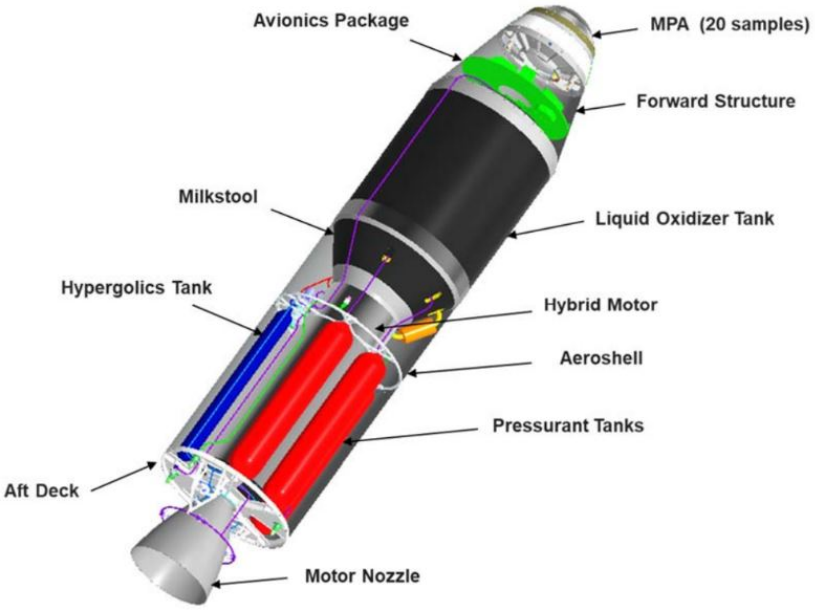

Figure 1.4. Final Design Concept of a Hybrid Rocket Motor-Powered Mars Ascent Vehicle[8]

Hybrid motors can also be used on lander vehicles in places where the gravity is lower than that of Earth. Researchers from the Korea Aerospace University developed and tested a $200N$ throttleable hybrid rocket lunar lander system capable of achieving a landing velocity of $1.01m/sec$ from initial testing. This system was split into four motors, consisting of high-density polyethylene (HDPE) fueled motors, each producing $50N$ of nominal thrust[9].

1.3.2 Small Satellite Propulsion

Hybrid rocket motors might be better suited for spacecraft, smallsat, and/or cubesat propulsion applications. Their inherent safety makes them viable options for propulsion systems on smallsats or cubesats that rely on rideshare opportunities to get into space. Being secondary payloads, they usually have little to no control over their orbit and would require some form of propulsion to get into the desired orbit[10]. Once in orbit, hybrid rockets can be used to maintain the orbit as well. Other functions such as interplanetary travel, orbit insertion, attitude control, and even desaturation of other attitude control actuators can be done. Suborbital vehicles used for space tourism, such as SpaceShipOne and SpaceShipTwo from Virgin Galactic can benefit immensely from the use of hybrid

rocket motors. The safety of hybrid rocket motors goes hand in hand with the increased safety requirements of civilian-carrying vehicles.

Some examples of hybrid rocket motors designed for these functions come from the Institute of Aviation in Warsaw (shown in figure 1.5) Poland, NASA Ames, NASA JPL, and Sapienza University of Rome.

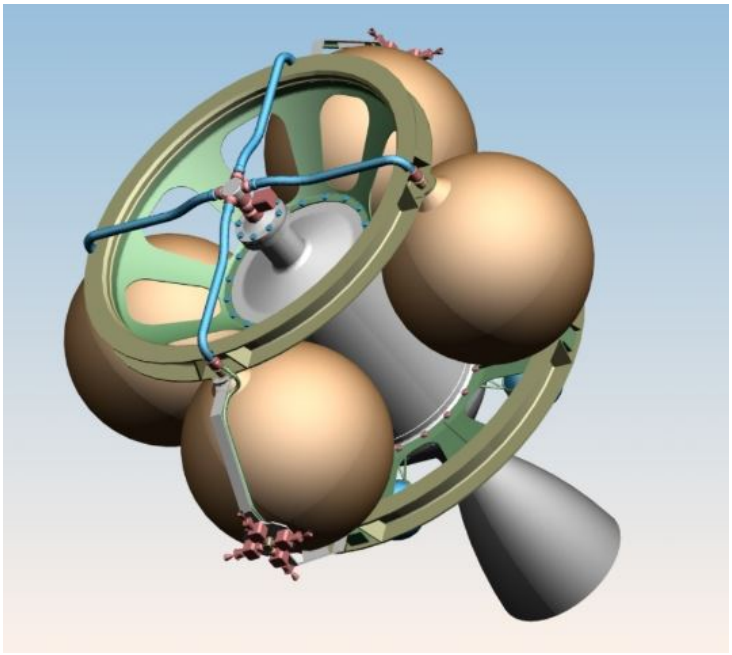

Figure 1.5. CAD Model of $200kg$ Small Satellite Hybrid Rocket Motor from Institute of Aviation in Warsaw[11]

The hybrid motor design from the Institute of Aviation in Warsaw was made to meet the station-keeping requirements of a $200kg$ small satellite. This motor was powered by a fuel mixture containing 75% Hydroxyl-Terminated Polybutadiene (HTPB) and 25% Aluminum particles, and used High-Test Peroxide (HTP, Hydrogen Peroxide concentration in excess of 80%) as the oxidizer. This motor was capable of producing 260-420N of thrust and used catalytic decomposition of Hydrogen Peroxide (HP) as the igniter system[11]. Development efforts at Ames Research Center produced a primary small satellite thruster capable of producing $25N$ of thrust and achieving a vacuum-specific Isp of $247sec$. Powered by polymethyl methacrylate (PMMA) fuel, Nitrous Oxide (N_2O) oxidizer, and an ethylene-N_2O torch igniter, this motor would function as the primary thruster for orbit maneuvering and maintenance functions[12]. A $44.4N$ ($10lbf$), PMMA/gaseous oxidizer

(GO_x)-powered motor was developed at NASA JPL for orbit insertion of an interplanetary cubesat. The motivation for this project was to avoid a fly-by observation mission such as the InSight mission with the Mars CubesatOne (MarCO) and enter Mars orbit to allow for longer observation time in the mission[13]. Finally, the hybrid motor developed at Sapienza University of Rome was also designed for Mars orbital insertion of an interplanetary cubesat[14]. The cubesat for this motor was twice the size of the cubesat of the JPL design and this resulted in a designed motor capable of producing $580N$ of thrust, evenly distributed among four primary thrusters, powered by Paraffin Wax fuel and N_2O oxidizer. Tables 1.1 and 1.2 summarize the relevant information and some performance metrics of the hybrid motors discussed.

Table 1.1. Summary of SmallSat Hybrid Motor Specifications, 1

	Warsaw SmallSat Motor[11]	JPL 12U CubeSat Motor[13]
Motor Function	Orbit Maintenance	Orbit Insertion
Igniter System	HP Catalytic Decomposition	Methane-Oxygen Torch
Fuel	75% HTPB, 25% Aluminum	PMMA
Oxidizer	HTP	GO_x
Thrust (N)	260-420	44.4
I_{sp} (sec)	No Data	311
Chamber Pressure (MPa)	1.00	1.38

Table 1.2. Summary of SmallSat Hybrid Motor Specifications, 2

	Ames SmallSat Motor[12]	Rome 24U CubeSat Motor[14]
Motor Function	Orbit Maneuvering	Orbit Insertion
Igniter System	Ethylene-N_2O Torch	N_2O Catalytic Decomposition
Fuel	PMMA	Paraffin
Oxidizer	N_2O	N_2O
Thrust (N)	25	145
I_{sp} (sec)	247	293
Chamber Pressure (MPa)	0.90	2.00

1.4 Purpose and Scope

Now that the motivation for using hybrid rocket motors has been established, the next chapter will discuss in more detail the fundamentals of hybrid rocket combustion and modeling. The ignition problem that hybrid rocket motors face will be introduced as well. The working concepts behind different ignition systems, such as torch igniters, throughout the literature will also be presented.

The main purpose of this study is to characterize the startup transient and steady state performance of a Nylon 6-Gaseous Oxygen hybrid rocket motor over a range of different input variables. A direct side-by-side comparison of a torch igniter comparing different fuels has not been done in the literature, so the different performance effects when using Hydrogen vs Methane as fuel for the ignition source will be quantified. Chapter three will introduce a rough expectation of performance for each igniter fuel based on theoretical considerations such as calculated combustion temperatures and efficiencies. The domain for the statistical design of experiments created will also be introduced.

Chapters four and five will provide information on the experimental setup, including descriptions of hardware, the piping system and electrical systems as well as the data collection and analysis methods. The final two chapters will present the results and provide a discussion of conclusions and recommendations for future work.

Chapter 2

Literature Review

In this chapter, a more detailed technical discussion about the complexities of the combustion process in the hybrid rocket motor found from theoretical and experimental means throughout the literature will be presented. Various ignition systems will also be discussed.

2.1 Hybrid Rocket Internal Combustion

Three main components will form the basis of the hybrid rocket internal combustion discussion. First, hybrid rocket motors undergo turbulent boundary layer combustion during normal operation. Second, the rate at which fuel is introduced to the combustion reaction and therefore the "oxidizer to fuel ratio shift phenomenon" is dependent on an empirically-derived regression model. Finally, the inherent safety advantages that hybrid motors have make igniting the motor much more difficult than their solid and liquid rocket counterparts.

2.1.1 Turbulent Boundary Layer Combustion

In hybrid rocket motors, because the fuel already exists in the combustion chamber as a solid and the oxidizer is injected as a gas, the gaseous oxidizer flows over the solid fuel wall resulting in turbulent boundary layer combustion. The fuel enters the combustion process by ablating from the wall with a velocity perpendicular to the main flow of the oxidizer. The active combustion zone, which can be interpreted as the flame sheet, develops where

the oxidizer to fuel ratio of the mixing propellants is within the operating flammability limits. The shape of this flame sheet matches the shape of the boundary layer. The heat from the flame sheet becomes the heat source to ablate, or more accurately, pyrolyze, the fuel from the wall and is transferred through radiation and convection. The term 'pyrolyze' or pyrolysis refers to the process of the fuel undergoing both the physical sublimation from solid to gas and the chemical change from long hydrocarbon polymer chains to individual combustible monomers.

Upon the turbulent boundary layer combustion process being initiated, the position of the flame sheet is not initially fixed. The velocity component of the fuel ablating from the wall pushes the flame sheet away from the wall and slightly reduces the heat transfer rate to the fuel wall. With this reduction of heat the amount of fuel pyrolyzed from the fuel surface is reduced and this wall blowing effect decreases. This causes the flame sheet to move back closer to the fuel wall surface. This back and forth goes on until the flame sheet settles in an equilibrium position. It has been found that, depending on the propellants used, the flame sheet position settles at around 10-20% of the boundary layer thickness from the wall surface[15].

Because of how the propellants are introduced to the combustion zone, it can be seen that the area above the flame sheet (further from the solid fuel surface) is in lean conditions while the area below the flame sheet (closer to the solid fuel surface) is in fuel rich conditions. To fully describe the turbulent boundary layer combustion environment, the fuel, oxidizer, and product concentrations and temperature values can be plotted as a function of vertical position from the fuel wall, with the positive direction moving away from the fuel surface as shown in figure 2.1. The oxidizer concentration gradient is always positive as the concentration of oxidizer is always increasing as the vertical position moves away from the wall surface. It would then follow that the fuel concentration gradient is always negative. As the vertical position from the fuel wall increases, the fuel concentration is always decreasing. Because combustion is only occurring within the flame sheet, it can be seen that the product concentration gradient is negative above the flame sheet and positive below the flame sheet. Finally, the temperature gradient matches in

pattern with the product concentration, with some treating the maximum point within the flame sheet as a discontinuity.

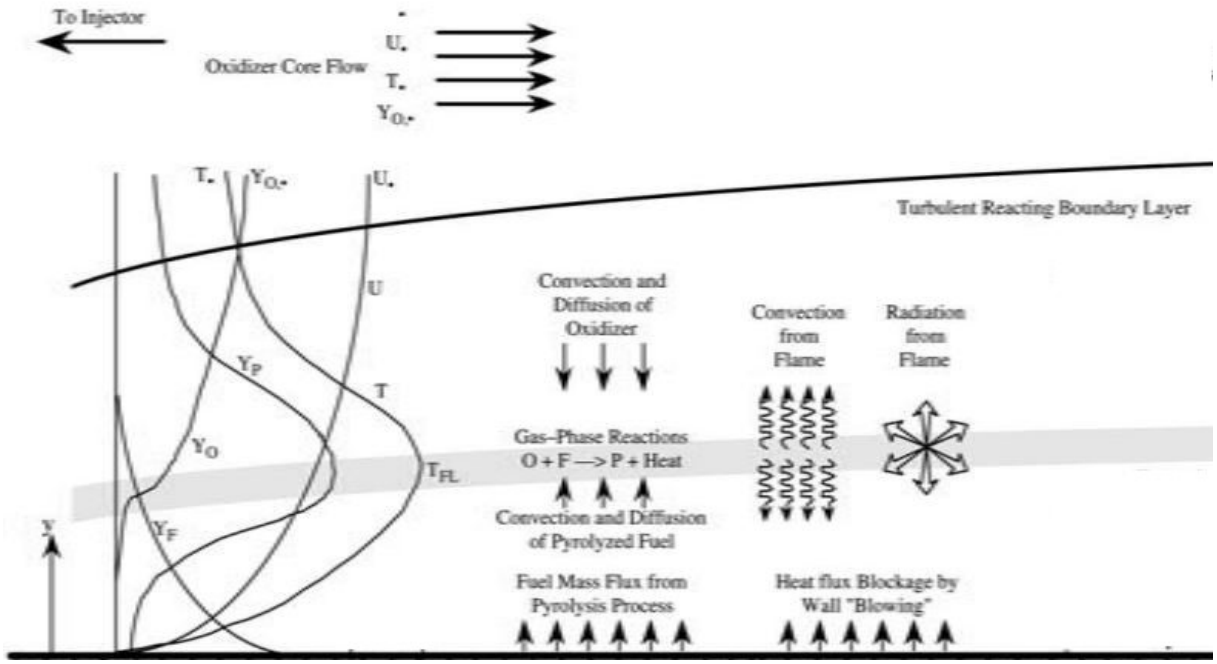

Figure 2.1. Turbulent Boundary Layer Combustion Mechanisms[16]

On the left-hand-side of the figure, the propellant concentration and temperature distributions as functions of vertical position from the wall are shown with the concentrations of the products, oxidizer, and fuel denoted by 'Y_P', 'Y_O', and 'Y_F' respectively. The temperature distribution is denoted by 'T' with the maximum temperature shown as the flame temperature at T_{FL}.

The unique combustion process for hybrid rockets previously described results in the propellants reacting in a diffusion, rather than premixed, flame. The diffusion flame sheet is indicated in the figure above by the shaded gray line in the middle of the boundary layer. This is the main reason why combustion efficiencies in hybrid motors are lower than in liquid and solid rockets with the consequence being reduced performance, as pointed out in the previous chapter. There are other factors that contribute to this lowered combustion efficiency such as the mechanics of turbulent boundary layer diffusion making it difficult for the oxidizer to enter the fuel rich boundary layer in the first place. Because of this, the steady state combustion in hybrid motors is actually always slightly fuel-rich, rather

than at stoichiometric conditions. Until now, the description of the combustion process has been treated as a turbulent boundary layer flow over a flat surface, when in reality the flow more closely resembles that of a fluid flowing through a pipe. This means that at some point along the length of the fuel grain, the turbulent boundary layer can become fully developed, which has been reported to be about 40 to 100 diameters along the length of the fuel grain. However, hybrid motor designs found throughout the literature do not have fuel grain lengths that reach these values and therefore, a core flow of oxidizer passes through the entire length of the fuel grain unreacted, further contributing to the low combustion efficiency. Disrupting the core flow in a post combustion chamber however, can mix this core flow with unburned fuel and increase the combustion efficiency close to theoretical limits.

It might be logical to think, then, that reducing the oxidizer flow rate can minimize the theorized unreacted core flow, which leads to the necessary discussion of the cooking and flooding limits of operation. Unlike the lean and rich flammability limits of a general combustion reaction, the cooking and flooding limits are the minimum and maximum oxidizer flow rates where the hybrid motor can operate reliably. The low oxidizer mass flux limit has been called the cooking limit because at these conditions heat transfer to the fuel surface and therefore regression rates are low. This can cause thermal waves to penetrate deep into the fuel grain charring and melting, or "cooking" the fuel material below the surface, which then leads to undesirable and non-uniform operation as the fuel surface regresses to the "cooked" portions of the fuel. On the other hand, the high oxidizer mass flux limit is called the flooding limit because beyond this limit, the flame propagation becomes too slow to keep up with the velocity of the oxidizer and the combustion stops. The motor is then considered to be flooded with too much oxidizer. Near the flooding limits, combustion becomes controlled by kinetics rather than diffusion resulting in lower observed efficiencies. These cooking and flooding limits depend on the propellants used, for example, highly reactive propellant combinations typically have higher flooding limits. While problems operating near or at these limits are scarce in the literature, it is still noteworthy for future designers to consider[16].

Some final turbulent boundary layer combustion characteristics to consider are the acceleration of the core flow across the length of the fuel grain, combustion port surface roughness and shape effects, wall deformation, and solid fuel additives. As will be treated in greater detail in the next section, the regression rate of fuel in the hybrid motor depends only on the local oxidizer mass flux according to the widely accepted empirically-derived regression model given by equation 2.1. While the oxidizer mass flux at the front end of fuel grain can be controlled, this is not the case across the length of the fuel grain. Introduction of varying amounts of fuel along the oxidizer flow path accelerates the core flow thus changing the local mass flux of oxidizer.

Surface roughness and fuel port shape can also significantly affect the performance of hybrid motors. Higher surface roughness can potentially induce more mixing and enhanced heat transfer. On a larger scale changing the fuel port shape altogether can improve the overall combustion performance as studies from Utah State University and Chinese Academy of Sciences demonstrated increased fuel regression rates of about 16-60% and 20% in helical-shaped fuel ports when compared to a straight cylindrical fuel port[17, 18]. Examples of such fuel ports are shown in the figure below.

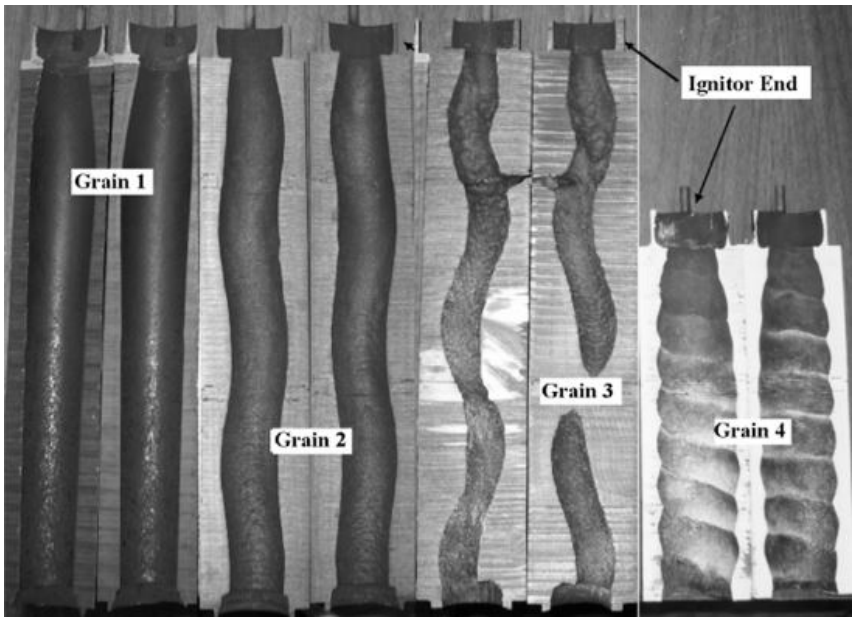

Figure 2.2. Post-burn Straight vs Helical Fuel Ports[17]

Powdered metal-based fuel additives can have a number of significant effects on the

performance of hybrid motors by changing the fuel enthalpy of gasification, total latent heat[19], and in the case of paraffin wax that forms a liquid melt layer before becoming a gas, the melting enthalpy[20]. Fuel additives can also enhance regression rates by introducing a significant radiative heat transfer component to the fuel surface directly resulting in an increase of up to 50% in the mass burning rate in one study[7]. The heavier metallic particles also increase the overall fuel density and mass flow rate of exiting products, increasing the thrust and motor volumetric efficiency.

2.1.2 Solid Fuel Regression

Since the rate at which fuel is introduced to the combustion is dependent on the burn characteristics of the two propellants, it has been, until recently[21, 22], impossible to actively control the instantaneous oxidizer to fuel ratio. The regression rate of fuel, and thus the mass flux of fuel into the combustion process can be predicted using the widely accepted empirically-derived fuel regression model of the form:

$$\dot{r} = a_o G_{ox}^n \tag{2.1}$$

where $\dot{r}$ is the fuel regression rate and G_{ox} is the oxidizer mass flux. The empirically derived constants a_o and n are the regression rate scale factor and burn exponent. These constants vary with different fuel/oxidizer combinations. Table 2.1 shows a selection of the regression rate equation constants for different fuel/oxidizer combinations[23]. This equation implies that the regression rate is independent of chamber pressure and only depends on the oxidizer mass flux. Through a detailed study of fuel regression mechanisms, it can be mathematically shown that the solid fuel degradation is purely a thermally induced process and independent of chamber pressure[24].

Table 2.1. Regression Rate Coefficients for Various Fuel/Oxidizer Combinations[23]

Fuel/Oxidizer Combination	a_o	n
HTPB/LO_x	0.0146	0.681
HDPE/LO_x	0.0098	0.620
Paraffin/LO_x	0.0488	0.620
Paraffin/N_2O	0.0491	0.500
ABS/GO_x-98mm	0.0480	0.450
ABS/GO_x-38mm	0.0550	0.200

The last two entries in table 2.1 were found through direct experimentation in reference [23] and used a 98mm and 38mm diameter motor respectively. The regression model curves using equation 2.1 are plotted in figure 2.3.

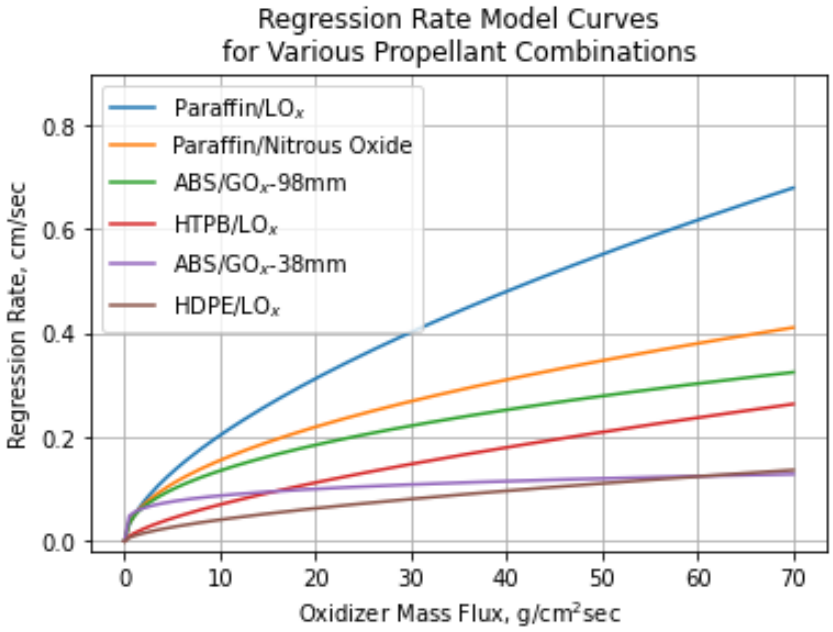

Figure 2.3. Regression Rate Model Curves for Various Propellant Combinations, adapted from[23]

Using this relationship can help designers determine fuel port specifications such as the length of the fuel port (or fuel grain) and initial diameter to produce a desired thrust profile. The determination of the constants a_o and n can be the subject of entire book

chapters as there are various methods used in the literature. The authors of [13] caution that designers should take careful consideration when using published values from sources that do not sufficiently document the steps taken to obtain those values. Here, four methods to obtain the coefficients will be described. It should be noted that all the methods presented assume a cylindrical fuel port, spatial independence of regression rate (i.e. the regression rate is not a function of position along the fuel port), and the fuel grain burns uniformly over the entire duration of the burn.

The first method, presented in [25] begins with equation 2.1 with the oxidizer mass flux term represented as the oxidizer mass flow rate over the circular fuel port cross section area so that 2.1 becomes

$$\dot{r} = a_o(\frac{\dot{m}_{ox}}{\pi r^2})^n \tag{2.2}$$

where r is instantaneous fuel port radius and $\dot{m}_{ox}$ is the mass flow rate of the oxidizer. All terms are then brought to the left side of the equation and integrated, to obtain

$$(\frac{r_f^{2n+1} - r_i^{2n+1}}{2n+1})(\frac{\pi^n}{a_o \dot{m}_{ox}^n}) = t_b \tag{2.3}$$

where r_f and r_i and the final and initial fuel port radii, and t_b is the total burn time. The final fuel port radius is found by using the measured mass difference of the fuel grain from before and after the burn, fuel density, and calculating the resulting fuel port radius making the assumption that the fuel burned evenly across the entire fuel port surface in a cylindrical shape. Equation 2.9 at $t = t_b$ is used for this calculation. The right hand side of equation 2.3 is just the total burn time, so since all the variables except a_o and n are known, a non-linear curve fit can be applied using data from multiple tests. The authors used the *fminsearch* Matlab built-in function.

The next method also comes from [25] and uses the time-spaced average regression rate to create a line of best fit for the equation

$$\log(\overline{\dot{r}}) = n \log(\overline{G_{ox}}) + \log(a_o) \tag{2.4}$$

where $\overline{\dot{r}}$ is the time-space average regression rate calculated from

$$\overline{\dot{r}} = \frac{r_f - r_i}{t_b} \tag{2.5}$$

and $\overline{G_{ox}}$ is the average oxidizer mass flux found by

$$\overline{G_{ox}} = \frac{4\overline{\dot{m}_{ox}}}{(r_f + r_i)^2} \tag{2.6}$$

The authors of [25] found that for their data with PMMA fuel, the space-time averaged method predicted larger burn exponents n, and produced larger error residuals. Three additional methods of averaging the oxidizer mass flow rate for this method were proposed and also used with the data and produced regression model coefficients that were much closer in value to each other than with the non-linear curve fit method.

The third method from [23] uses the industry standard NASA Chemical Equilibrium Applications program (CEA)[26] to find the time history of the mass flow rate of fuel. This is found by taking the difference between the product mass flow rate through the nozzle exit and measured oxidizer mass flow rate. The product mass flow rate is found using the chamber pressure data via the equation

$$\dot{m} = A_t \frac{P_o}{\sqrt{T_o}} \sqrt{\frac{k}{R} (\frac{2}{k+1})^{\frac{k+1}{k-1}}} \tag{2.7}$$

It should be noted that the variable for the mass flow rate of the combustion product is the same physical variable as $\dot{m}$ used in equation 1.1. The combustion chamber temperature, gas constant, and ratio of specific heats are found using CEA, while the throat area and combustion chamber pressure are directly measured. Then, the fuel regression rate, expressed as the fuel mass flow rate divided by density and burn area of the fuel is given by the equation

$$\dot{r} = \frac{\dot{m}_f}{2\pi\rho_f r L} \tag{2.8}$$

where ρ_f is the density of the solid fuel, $\dot{m}_f$ is the mass flow rate of the fuel, and L is the length of the fuel grain. This equation can be rearranged and integrated to find the instantaneous fuel port radius as a function of time shown below

$$r(t) = \sqrt{r_i^2 + \frac{\int_0^t \dot{m}_f dt}{\pi\rho_f L}} \tag{2.9}$$

The oxidizer mass flux can then be found by dividing the measured oxidizer mass flow rate by the instantaneous fuel port area which is a function of equation 2.9. The oxidizer mass

flux and regression rate as functions of time can then be plotted against each other and be curve fitted to estimate the constants a_o and n. It should be noted that for equation 2.9, when $t = t_b$ the variable for the measured change in fuel grain mass can be used Δm_f where

$$\Delta m_f = \int_0^{t_b} \dot{m}_f dt \tag{2.10}$$

The final method presented in this section involves selecting a known burn exponent. Then, a fourth order Runge-Kutta scheme is applied to equation 2.1 to solve for the fuel port radius and fuel mass flow rate at every time step. Using equation 2.8 in the form

$$\dot{m}_f = 2\pi\rho_f r L\dot{r} \tag{2.11}$$

the mass flow rate of fuel is numerically integrated to find the total mass of fuel burned. This process is repeated and the scale factor is iterated until the integrated fuel mass flow equals the measured mass burned[12].

Although it is widely accepted in the literature to make the assumption that the fuel burns evenly and uniformly across the entire fuel grain surface, qualitative analyses have shown that this is not the case. The authors of [25] then propose a pressure-dependent relationship for regression rate and oxidizer mass flux of the form

$$\dot{r} = a_o G_{ox}^n \overline{P}_o^q \tag{2.12}$$

where $\overline{P}_o$ is the time-averaged combustion chamber pressure and q is the pressure-based burn exponent. In this equation a_o would have different units than in equation 2.1. Although a scalar value is used when evaluating equation 2.12, actual pressure variations along the fuel grain surface could then account for nonuniform burning rates across the fuel surface. Others have created more detailed, position-dependent fuel regression models such as the one presented in [27].

To conclude the discussion of regression rate modeling and analysis, the oxidizer to fuel ratio shift phenomenon and the significance of the burn exponent, n, must be recognized. As mentioned in the previous chapter, one of the disadvantages of hybrid rocket motors is the inability to directly control the oxidizer to fuel ratio over the course of the burn.

Since the fuel port ratio changes naturally over the course of the burn, the amount of fuel introduced to the combustion reaction changes[28]. It was found in [23] that for fuel/oxidizer combinations with a burn exponent of $n > 0.50$, the oxidizer to fuel ratio shift phenomenon adheres to the commonly observed steady increase in oxidizer to fuel ratio over the course of a burn. On the other hand, fuel/oxidizer combinations with a burn exponent of $n < 0.50$ will exhibit the opposite effect and have the oxidizer to fuel ratio steadily decrease over the course of the burn. Although rare, if $n = 0.50$ exactly, the oxidizer to fuel ratio will remain constant. It can be seen from the third column in table 2.1, that the oxidizer to fuel ratio typically increases for various fuel/oxidizer combinations while on the other hand, when ABS is used the oxidizer to fuel ratio decreases over the course of the burn.

2.1.3 Ignition Problem

The keystone of hybrid rocket safety is the stability and isolation of the fuel and oxidizer. This also makes igniting the motor a difficult task. The propellants essentially have a larger "activation energy" to ignite compared to the propellants in solid and liquid rockets. However, once combustion is initiated, the heat of already ablated fuel reacting with the flowing oxidizer sustains combustion.

The heat required to ignite a hybrid motor is the sum of the heat needed for: 1) raising the temperature of the solid fuel, 2) depolymerization of solid fuel hydrocarbon chains, 3) sublimating the solid fuel[15], and in some cases such as using Paraffin wax, 4) melting then vaporizing the fuel.

The difficulty in reliably, safely, and efficiently igniting hybrid rocket motors is the reason this form of propulsion has not seen widespread use in actual flight[29]. Designing and analyzing hybrid rocket motor ignition systems is an active area of research. Studies on various ignition systems have been compiled in the next section to discuss the advantages and drawbacks of different types of ignition systems.

2.2 Ignition Methods

The most common ignition systems found throughout the literature include pyrotechnic charges, laser igniters, catalyzed mono propellants, and methane-oxygen torches. Discussion on which beneficial traits each of the ignition systems have and don't have will be presented. Ideally, a good ignition system will be non-toxic, reliable, durable (can be reignited many times with little to no system degradation), and safe to operate. Good ignition systems will also have low mass, low mechanical complexity, and repeatable transient behavior and performance. Low power consumption is also a desirable feature.

2.2.1 Pyrotechnic Charges

Pyrotechnic igniters are simply explosive charges that, when activated, can provide the heat necessary to pyrolyze the solid fuel of a hybrid motor. While this method is probably the easiest way to provide the most amount of energy to the fuel grain, it is accompanied with many issues. The first issue is that pyrotechnic charges are usually designed to be used only once and therefore are not long-lasting, and remove restart capabilities from the motor[30]. Hybrid motors in lab settings can use pyrotechnics as the hardware can be replaced manually between experiments, for example, a lab-scale hybrid motor from the University of Arkansas at Little Rock used hobby solid rockets as a pyrotechnic-like ignition source replacement when other ignition materials ran out[31]. Replacement of pyrotechnic charges is not possible during flight. The explosive nature of pyrotechnic charges and risk of accidental detonation from hazards of electromagnetic radiation to ordnance eliminate them from use on potential small satellite or cubesat missions that rely on being placed as secondary payloads for other missions since it would pose a danger to the primary payload[30].

2.2.2 Laser Ignition

Due to continuous miniaturization of electronics and semiconductors, laser ignition in various aerospace applications has been steadily gaining popularity since the early 1990's. Now, with hybrid motors gaining popularity as a propulsion system for small satellites, this ignition method has been considered for the application of igniting hybrid motors.

A high energy laser concentrating 1-10 Watts of power to an area on the order of $1mm^2$ can cause a laser-induced flash pyrolysis event that ablates high-temperature carbon-based particles from the fuel. When a small area of fuel is pyrolyzed, a cavity in the fuel surface is formed that, when oxidizer flows over it, creates a re-circulation zone that allows the energy-carrying carbon particles to mix with the main oxidizer flow. These carbon particles then carry the energy to the rest of the propellant bulk flow[32].

Some of the benefits of this ignition method is that lasers have been found to be a reliable source of ignition energy[32]. They also require the least amount of mechanical complexity compared to other ignition methods such as the catalytic ignition, and torches that will be described later, as all these require extra hardware for precombustion propellant treatment. Lasers are also low energy with tests demonstrating reliable ignition for $200ms$ pulses resulting in $2.2J$ of total ignition energy at atmospheric pressure, and 50 ms pulses resulting in $0.6J$ of ignition energy in vacuum conditions[33]. Lasers are durable as they can be powered on reliably for thousands of hours[34]. One of the main drawbacks with this ignition method, however, is the inability to repeat ignition transients. The tests in [33] also found that because the fuel surface regresses away from the focal point of the laser with each burn, the ignition delay for each successive burn would steadily increase as the laser intensity would decrease. After looking at a basic schematic for how the laser igniter works in figure 2.4, it is easy to see how the regressing surface fuel, getting further away from the laser's focal point, can change the energy profile delivered to the fuel surface and therefore change the igniter's performance over time.

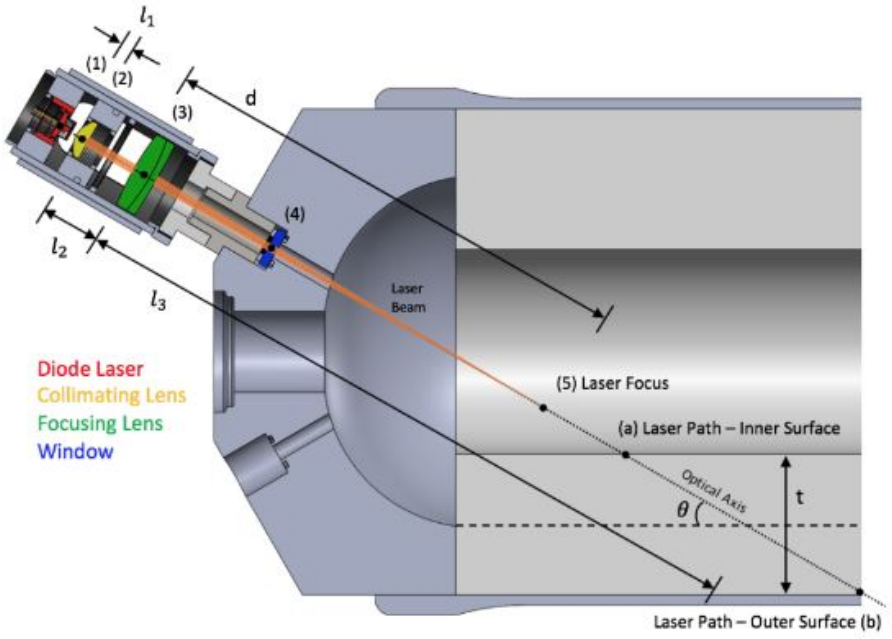

Figure 2.4. Laser Igniter Schematic[34]

2.2.3 Catalytic Ignition

A catalytic ignition system works by reducing the activation energy of the decomposition reaction of a propellant. A graphical representation of this reduction in activation energy is shown in figure 2.5. When the activation energy is lowered, and the decomposition reaction occurs, heat is released as a product. This heat release then goes into heating and pyrolyzing the solid fuel grain. The proposed hybrid propulsion design from [11] uses this method of ignition by decomposing high concentration Hydrogen Peroxide flowing through a steel-ceramic-platinum catalyst bed consisting of 43 substrate sheets. Adding many sheets for the flowing propellant to pass through can introduce significant pressure drops[35].

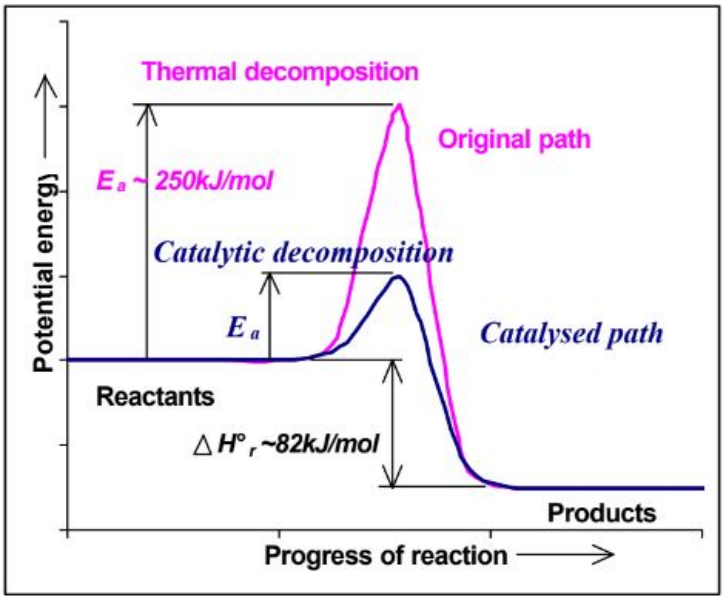

Figure 2.5. Graphical Representation of Catalytic Reduction in Activation Energy[36]

A system developed at Purdue University relied on a more compact, and light-weight consumable catalytic bed (CCB) embedded into the fore-end of the fuel grain. The engine was then "slam started" when Hydrogen Peroxide, used as the oxidizer, came into contact with the CCB. While this system was extremely light-weight, used no electrical power, and even demonstrated repeatable transient behavior, it was not explicitly stated how many restarts this CCB was capable of, or if the entire material was consumed in one firing[37].

With the exception of the last system discussed, catalytic ignition systems typically require relatively larger mass than other ignition systems, using either dense and toxic substrates, or high-surface configurations[36]. They also provide poor, although in most cases consistent, transient behavior with some reporting up to 3 minutes of catalyst bed heating time.

2.2.4 Utah State University Arc Igniter

While every other method of ignition discussed has decades of research behind the mechanisms and heritage in other aerospace applications, the novel ABS (Acrylonitrile Butadiene Styrene) Arc Igniter developed at Utah State University has only recently been invented about ten years ago at the time of this writing. After discovering unique elec-

trostatic breakdown properties specifically in Fused-Deposition-Modeling (FDM) printed ABS, an igniter was developed that takes advantage of the heat generated and hydrocarbon vapor produced by the electric arcing between printed ABS layers[38] as shown in figure 2.6. The heated hydrocarbon vapor mixes and reacts with the flowing oxidizer. This initial reaction provides the heat required to pyrolyze the rest of the fuel grain surface and initiate motor operation. The electrical arcing across the printed ABS layers follows similarly but not exactly as predicted by Paschen's law when a voltage is applied to the "mini fuel grain"[39]. The development of this igniter started off as a "strap-on" system added to the motor's injector cap before directly adding electrical leads into the fully integrated precombustion chamber downstream of the oxidizer injector[40].

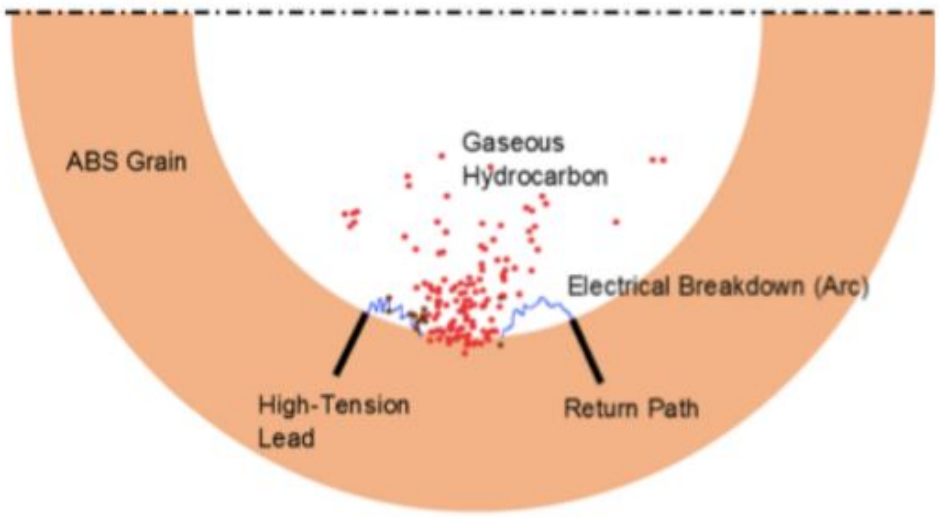

Figure 2.6. Visual Representation of ABS Arc Igniter Mechanism[38]

This ignition system overcomes many of the problems encountered when working with other ignition systems. It does not use toxic propellants, it is long-lasting with some tests reporting up to 27 consecutive firings[38], and it is mechanically simpler in that it does not require hardware for extra plumbing. It is also lower power with flight tests done on a Terrier-Malamute Sounding rocket, spending 200 seconds in hard-vacuum conditions above the Von-Karman line, recording 1-3 Watts of power draw. It can also be compact with the entire flight test hardware consisting of two 6-N thrusters fitting in a cylindrical volume with 12 inch diameter and a height of 10.75 inches[41]. Considering voltage was

applied to the electrical leads in the fuel grain on the order of one second or less, the total ignition energy would result in less than 1-3 Joules.

2.2.5 Methane-Oxygen Torch and Glow Plug Igniters

The Methane-Oxygen torch igniter has significant heritage in other aerospace applications such as in liquid rocket engines[42]. One reason for this is reliability as spark plugs have been developed over the decades to a high level of reliability[43]. Recently, various hybrid motor design and development projects have employed the use of a Methane-Oxygen igniter[13, 18, 25, 43–48].

The Methane-Oxygen torch igniter is similar to the ignition in the cylinder of a four-stroke internal combustion engine for automobiles where the mixed fuel and oxidizer in gaseous state undergo combustion activated by heat added from a spark plug. For hybrid rocket motors, only a small amount of externally-stored gaseous fuel is injected into the main oxidizer flow and the heat produced from this brief combustion pyrolyzes the solid fuel and initiates combustion of the main fuel with the flowing oxidizer. Methane torch igniters can be reliable, operating in relatively large oxidizer to fuel ratios with some reporting successful ignition for oxidizer to fuel mass ratios of 2.97-31.6[43] and 5-60% of methane by volume[44]. The injector design from [44] employs swirl injection of the oxidizer around a core flow of methane, as shown in figure 2.7 where the oxidizer enters through the helical injector at 2 and the fuel through the axial injector at 3. This injection method has been found to introduce film cooling of the precombustion chamber walls and reduced competition between igniter fuel and main solid fuel to react with oxidizer flow.

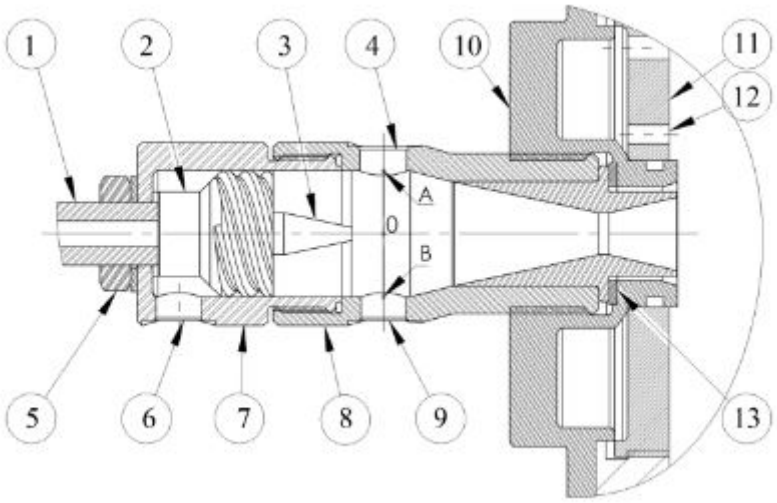

Figure 2.7. Cross Section View of Swirl Injector for Methane-Oxygen Torch Igniter[44]

The Methane-Oxygen torch ignition system poses many benefits through the use of non-toxic propellants, requiring low power for the spark plug, long lasting operation as long as fuel supply lasts, and reliable operation. One of the studies referenced found that when a Methane-Oxygen torch was used on the exact same hybrid motor system that the laser ignition system from [33, 34] was used on, the torch resulted in a consistent and smaller ignition delay by about $700ms$[45]. The obvious disadvantage of this system is the added hardware mass and mechanical complexity introduced by accommodating plumbing for the igniter fuel, as well as a storage tank.

A glow plug igniter has also been tested in the literature. The underlying concept of operation is the same as with the torch igniter but instead of a spark plug, a metal glow plug is heated to temperatures in excess of 1000 C. The glow plug igniter developed at NASA Glenn Research Center was found to be unreliable at times, and took over 7 seconds for the plug to heat up to maximum temperature, before it could be used to ignite the propellants[49].

2.2.6 Hydrogen-Oxygen Torch

The operation of the Hydrogen-Oxygen torch is exactly the same as with the Methane-Oxygen torch. With the exception of one recent study[50] a Hydrogen-Oxygen torch has

not seen use as a hybrid rocket motor igniter. The experiments in [50] found that within a certain design space, increasing the mass flow rate and duration would increase the time-space averaged regression rate.

The Hydrogen-Oxygen torch igniter designed in [50] was inspired by an existing Hydrogen-Oxygen torch from NASA Lewis (now Glenn) Research center to ignite liquid-propellant rocket engines. This igniter further demonstrates the reliability of a torch igniter system (regardless of the fuel used) by operating for 100 firings before degradation was observed on the spark plug, and a total of 400 successful firings despite the observed degradation[51].

Chapter 3

Theoretical Approach

In this chapter, rationale for predicted performance of Hydrogen and Methane will be explained through consideration of their combustion characteristics such as flame speeds, adiabatic flame temperatures, combustion efficiencies, flammability limits, and ignition energy. Further discussion about the igniter fuel storage characteristics and availability will serve as a primer for the discussion of the results to assess whether (if it is indeed the case) any observed performance enhancements may be worth poor storage and availability. Finally, the statistical design of experiments (DOE) created to conduct this study will be presented.

3.1 Propellant Combustion Characteristics

3.1.1 Flame Speeds

The flame speed, a representation of the rate at which the flame of a combustion reaction propagates throughout a fuel and oxidizer mixture, will be used as the first indicator to assess igniter fuel performance. At standard temperature and pressure, the laminar flame speeds of Methane and Hydrogen are $36.2 cm/sec$ and $219.7 cm/sec$ respectively[52]. Figure 3.1 shows the flame speeds of various fuels for varying oxidizer to fuel ratios.

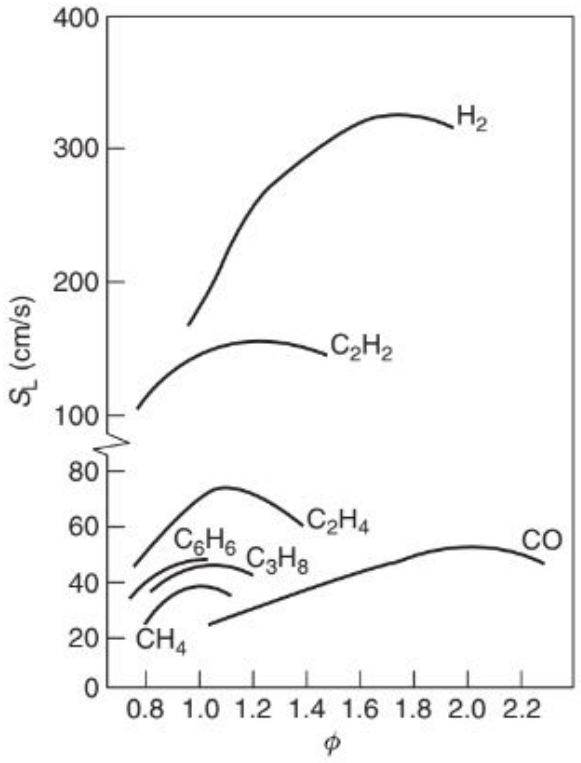

Figure 3.1. Laminar Flame Speeds vs Equivalence Ratio (ϕ) for Various Fuels[52]

The range of laminar flame speeds for methane is roughly 20-40cm/sec while the range for Hydrogen is roughly 160-320cm/sec. Although these are flame speeds in the laminar flow regime and combustion in the hybrid rocket motor takes place in the turbulent boundary layer, these metrics are still valid since the flame speed in turbulent flow conditions are a function of the laminar flame speed, denoted by the variable S_L, and "turbulence intensity" (U'). Many models to relate the laminar and turbulent flame speeds have been proposed and figure 3.2 shows a general relationship between the two.

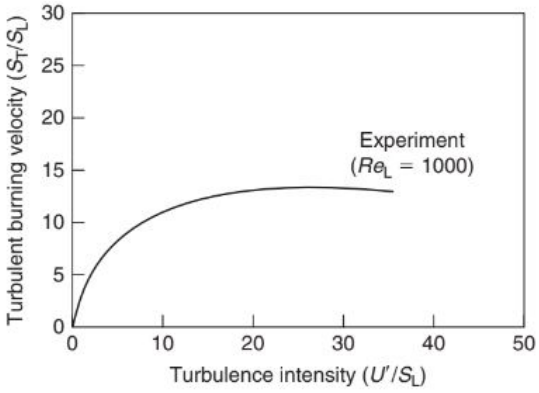

Figure 3.2. General Turbulent Flame Speed as Function of Laminar Flame Speed[52]

With faster flame speeds for Hydrogen, this could potentially translate to shorter ignition latencies and a more uniform initial pyrolysis of the fuel grain surface. As the flame propagates faster the energy required to pyrolyze the solid fuel could be delivered faster, which could also prove to be helpful in the event of cold starts, which is not only possible but likely that the fuel grain can reach extremely low temperatures in space. Other studies have found that faster flame propagation through Hydrogen enrichment yielded more stable and even burns in a Wankel rotary engine due to reduced wall-quenching effects[53, 54]. It should be noted, however, that the flame only propagates where the fuel-oxidizer mixture is within the flammability limits. Therefore if the igniter fuel has not had time to fill up the fuel port before the spark plug is ignited, then the flame speed could potentially have little to no effect on the ignition latency.

3.1.2 Adiabatic Flame Temperatures

It has already been established that the heat transfer rate to the fuel surface is directly related to the rate of pyrolysis of the fuel[55]. It is a basic principle of heat transfer that the rate at which heat is delivered is dependent on the temperature gradient between the two points heat is traveling through. The difference in temperature between the ignited mixture and the fuel grain surface will determine the heat transfer rate and therefore the initial pyrolysis rate of the fuel. Figures 3.3 below shows the adiabatic flame temperatures for the Hydrogen-Oxygen and Methane-Oxygen reactions for varying equivalence ratios.

The equivalence ratio being the ratio between the oxidizer to fuel ratio at stoichiometric conditions and the actual oxidizer to fuel ratio. The NASA CEA program was used to calculate the adiabatic flame temperatures shown. These calculations are done at atmospheric pressure at sea level since, for the experiments in this study, the ignition event will occur at that pressure, roughly $101.3kPa$.

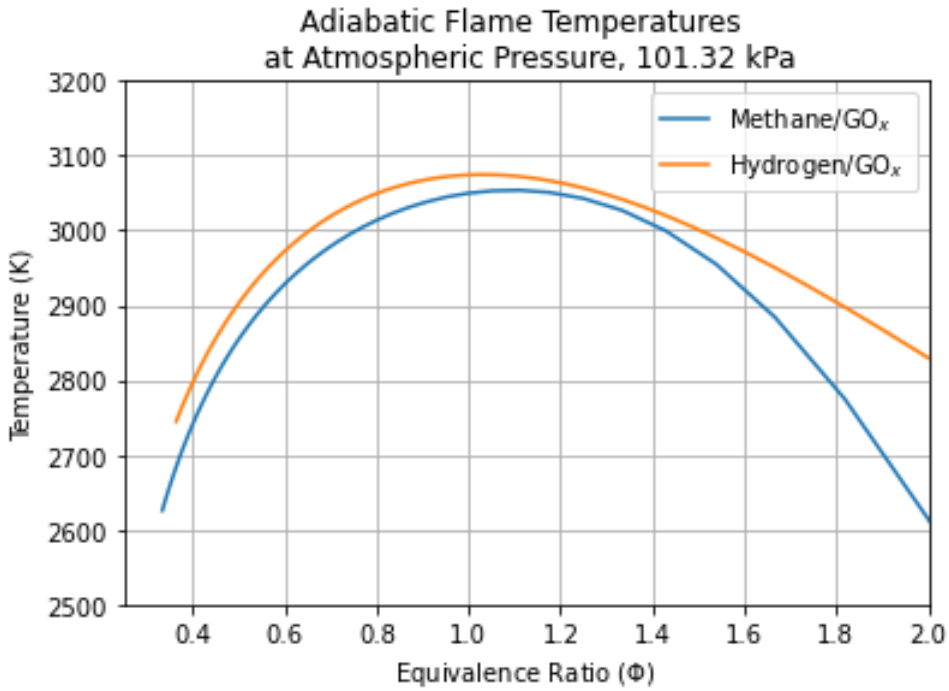

Figure 3.3. Flame Temperatures for Hydrogen and Methane

It can be seen that the for a given equivalence ratio, the difference in combustion temperature with oxygen between Hydrogen and Methane are never more than $50K$ apart except at equivalence ratios greater than 1.6. However at different equivalence ratios such as between $\phi = 0.50$ and $\phi = 0.67$ the combustion temperature difference is greater than $100K$ for both fuels. Therefore it is likely the ignition characteristics and pyrolysis rate of the solid fuel will be a stronger function of operating equivalence ratio rather than fuel used.

3.1.3 Combustion Efficiency (c*)

To gain more insight into what to expect for the transient performance, the c* for the ignition event was calculated using CEA[56] and plotted over varying mass-based oxidizer to fuel ratios. For these calculations, it was assumed they would take place at the expected operating chamber pressure of $1.03MPa$ ($150psia$). During the start-up transient, both the igniter fuel and the Nylon-6 main fuel will be mixing and burning with the incoming gaseous oxygen. To account for this, fuel mixtures with varying weight percentages of each component were input into the CEA program to see how different amounts of igniter fuel would alter the nominal performance compared to when only the Nylon-6 fuel is burning.

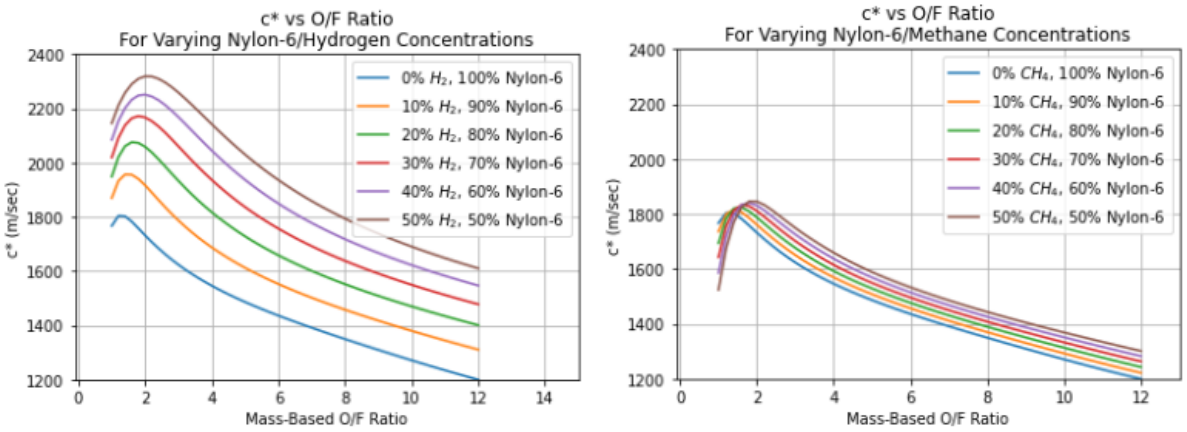

Figure 3.4. c* For Various Hydrogen/Nylon-6 (left) and Methane/Nylon-6 (right) Mixtures

Figure 3.4 shows a side by side comparison of the effect of adding different amounts of the igniter fuel. Increments of 10% mixture by weight were evaluated until each fuel made up 50% of the mixture. At no point during operation should the mixture percent for the igniter fuel exceed 50%. As a reference point, the reaction with Nylon-6 only with gaseous oxidizer was plotted on both graphs, with the maximum c* found to be 1,803m/sec. When adding Hydrogen, as shown on the graph to the left, the maximum c* increased by about 8.5% to 1,956m/sec for a 10% Hydrogen mixture, while the addition of the same weight percent of Methane increased the maximum c* value by less than 1% to 1,816m/sec. This trend continues for increasing amounts of igniter fuel added, with the maximum c* for 50% Hydrogen being 2,318m/sec, and 1,845m/sec for 50% Methane.

Clearly, Hydrogen is better than Methane at bringing the combustion chamber to a higher pressure and converting the stored chemical energy into kinetic energy.

3.1.4 Ignition Energy, Heat of Combustion, and Diffusion Velocity

The ignition energy, heat of combustion, and diffusion velocity of Hydrogen and Methane may also contribute effects to the transient performance of the hybrid rocket motor. Table 3.1 summarizes these values for Hydrogen and Methane. While the minimum ignition energy of a fuel depends on not only the chemical properties but the thermal environment as well, for the same scenario, [57] reports Methane having more than ten times larger minimum ignition energy at $0.29mJ$ than Hydrogen at $0.02mJ$. This means, with using the same igniter system for both fuels, it will be much easier to ignite the Hydrogen-Oxygen torch than the Methane-Oxygen torch. At normal operating conditions, this should not affect the reliability of the ignition system, but during flight if the spark plug begins to degrade and output less energy, Hydrogen will still have a better chance to ignite than Methane.

Table 3.1. Selected Combustion Properties of Hydrogen and Methane

	Hydrogen	Methane
Ignition Energy (mJ)	0.02	0.29
Heat of Combustion (kJ/g)	120	50
Diffusion Velocity (m/sec)	2.00	0.51

The heat of combustion, or lower heating value is the amount of energy available from a fuel when it undergoes a combustion reaction. For Hydrogen this is $120kJ/g$ and for Methane it is $50kJ/g$. This further supports the c^* star results from before, as the greater amount of heat available goes into creating higher pressure combustion products[57]. The diffusion velocity, which is dependent on the size of the molecule, determines how quickly the molecule can diffuse through a gaseous environment. In air at normal temperature and pressure ($293.15K$, and $101.3kPa$) the diffusion velocities for Hydrogen and Methane are on the order of $2.00m/sec$ and $0.51m/sec$ respectively [57]. This is important because

as mentioned in the discussion about flame speeds, the flame can only propagate at the flame speed if there is an adequate fuel and oxidizer mixture ratio, determined by the flammability limits which will be discussed next. Since Hydrogen can diffuse through the flow of gaseous oxygen faster than Methane, the case for expecting shorter ignition latency from using Hydrogen is further supported. Also, it is possible that Hydrogen could infiltrate the turbulent boundary layer better than Methane and displace gaseous Nylon-6 molecules and induce better mixing than without the presence of the igniter fuel.

3.1.5 Flammability Limits

Finally, the flammability limits, while possibly having little to no effect on the performance, need to be considered. The flammability limits will, however, determine the minimum and maximum amount of igniter fuel that can be used for a given mass flow rate of gaseous oxygen. According to the Limits of Flammability of Gases and Vapors from the United States Bureau of Mines[58], the lower and upper flammability limits for both Hydrogen and Methane in Oxygen for downward propagation through a cylindrical tube of 5.08 cm (2.00 in) diameter are as shown in table 3.2. These values were selected as the geometry for where these limits were determined match closely with the geometry of the igniter used in this study. These values are expressed in volume percent of fuel and closely match reported values from Combustion by Glassman[52].

Table 3.2. Flammability Limits of Hydrogen and Methane (% by Volume Fuel)

	Bureau of Mines[58]		Combustion[52]	
Limit	Lower	Upper	Lower	Upper
Hydrogen	9-10	92-94	4	96
Methane	5.15	60.5	5	61

As will be discussed more in the next section, Hydrogen is less dense than Methane, so it is possible a smaller mass of Hydrogen would be needed for successful ignition of the motor compared to Methane. This could translate to mass savings for the propulsion designer, at the cost of lower volumetric efficiency.

3.2 Propellant Storage and Availability

To analyze how much igniter fuel can be stored, data for Hydrogen and Methane fluid properties from the US National Institute of Standards and Technology (NIST)[59] at various temperatures and pressures were collected and plotted. Figure 3.5 shows the density of Hydrogen over different storage pressures at $120K$ and $400K$ as well as for Methane at $200K$ and $400K$. These temperatures were selected based on expected minimum and maximum values for geostationary orbit temperature cycling[60]. The range is $120K$ to $400K$ but since the density of Methane at $120K$ for the pressure range used is relatively large (on the order of 410-420kg/m^3), $200K$ was selected to plot to better visualize the data. The tank pressure range considers a lower limit based on being able to roughly maintain choked flow across the injector at the expected operating chamber pressure of this experiment ($1.03MPa$) and an upper limit based on the design of a cubesat propellant tank from Valcor[61] from July 2020 and is rated to store propellants at $6.20MPa$ ($900psia$).

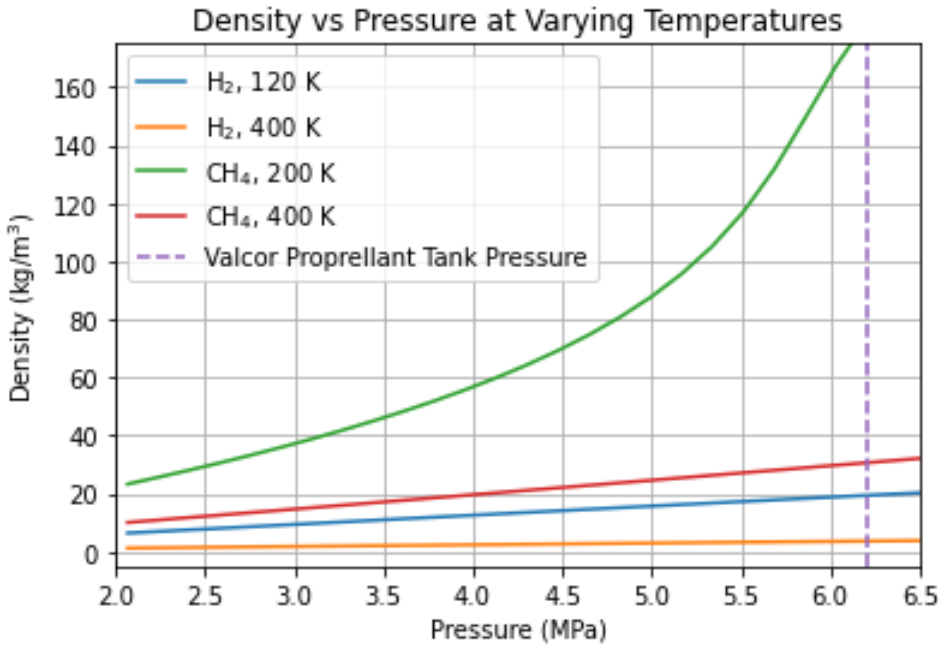

Figure 3.5. Hydrogen and Methane Storage Properties

Clearly, for the same temperature and pressure range, Methane has a larger density

by almost a whole order of magnitude yielding a larger volumetric efficiency and more ignitions per unit volume of igniter fuel storage. If the number of expected ignitions for a mission is known, then using the amount of igniter mass used for one ignition event could be used to properly size and minimize the tank's volume and weight. Taking the worst case scenario into consideration, at $400K$ tank temperature, the density of Hydrogen at $6MPa$ is only $3.5kg/m^3$ versus Methane's $30.0kg/m^3$. On the lower temperature side, at $6MPa$, the density of Hydrogen at $120K$ is still only $18.9kg/m^3$ while for Methane at $200K$ the density is $167.1kg/m^3$. Of course it would not be wise to fill up the tank to the latter state for either fuel because any increases in temperature would increase the pressure potentially past a tank's maximum pressure such as Valcor's $6.20MPa$ in this example.

If one were to take the horizontal grid lines as lines of constant propellant mass for a given tank volume, then it can be seen that the pressure sensitivity with respect to changes in temperature is greater for Methane than for Hydrogen. This could correlate to the need for a more precisely designed thermal management system if storing Methane. On the other hand, if the igniter fuel and main oxidizer were to be stored as liquids, a better thermal management system for a Hydrogen tank would be necessary as the boiling point is only $20K$, while the boiling point of Methane, at $112K$, is closer not only to the range of expected temperatures in GEO orbit, but also the boiling point temperature of Oxygen $(90K)$[62]. The final storage consideration is the molecule size. Because Hydrogen is so small, it is more prone to leaking as experienced with the Centaur upper stage rocket[63].

As for propellant availability, Hydrogen is the most abundant element on Earth and approximately 50% of the global demand can be produced via methods using sustainable energy[57]. On the other hand, Methane can be produced in-situ where carbon dioxide is available in the environment by reacting it with Hydrogen to produce Methane and water through the Sabatier process[64, 65]. The water produced can be electrolyzed to produce Oxygen and Hydrogen to be recycled back into the Sabatier reaction. So designers should consider potentially using Hydrogen for missions that would not land on extraterrestrial worlds such as observation satellites or interplanetary satellites. For applications such as

a Mars ascent vehicle, the ability to produce Methane in-situ and not carry it from Earth would potentially be more beneficial.

3.3 Statistical Design of Experiments

In order to get the most information while using the least amount of experiments, two factorial experiment designs as described by Lawson and Erjavec[66] were created to observe the effects that the chosen independent variables have on the performance of the hybrid rocket motor (dependent variables).

3.3.1 Independent Variables

The chosen independent variables, besides the fuel type used, are igniter operating equivalence ratio and fuel grain condition. A high and low value for each variable was selected and all values are summarized in table 3.3.

Table 3.3. Statistical DOE Independent Variables

Variable	Low Value	High Value
Fuel Type	Methane	Hydrogen
Equivalence Ratio	0.50	0.67
Fuel Grain Condition	Used	Fresh

This design space selected yields a 2^3 factorial experiment. However, due to limited resources, specifically in the number of Nylon-6 fuel grains available, a 2^1 factorial experiment to explore the effects of using a fresh versus used fuel grain was done. Then, using only used fuel grains from then on out, a 2^2 factorial experiment to examine the effects and interactions between varying the igniter fuel and the operating equivalence ratio. Essentially, only the latter factorial experiment would be run, however due to the reusing of fuel grains for subsequent runs, the first 2^1 was created to ensure that results found during the experiment campaign are indeed due to varying the fuel or equivalence ratio and not because of the fuel grain condition changing (i.e. surface charring, changing initial fuel port area, etc.).

The values for the equivalence ratio were selected based on the adiabatic flame temper-

atures found in section 3.1.2. Due to potential competition between the igniter fuel and Nylon-6 fuel species to react with the oxidizer, fuel-lean igniter equivalence ratios were desired, and to hopefully see if the greater than $100K$ combustion temperature difference would cause any effects, the equivalence ratios of 0.50 and 0.67 were selected. Varying the equivalence ratio would be accomplished by changing the mass flow rate of the igniter fuel while keeping a nominal oxidizer mass flow rate constant at $22g/sec$. The resulting mass flow rates for each igniter fuel at each equivalence ratio is summarized in Table 3.4.

Table 3.4. Igniter Fuel Mass Flow Rate

Fuel	Flow Rate at $\phi = 0.50$ (g/sec)	Flow Rate at $\phi = 0.67$ (g/sec)
Hydrogen	1.375	1.843
Methane	2.750	3.685

3.3.2 Dependent Variables

The measured dependent variables will be the thrust and chamber pressure time histories for each of the sixteen total runs. These data will be then used to determine the regression rate, ignition latency, c*, and specific impulse. It will be these four variables derived from the collected data that will be used as the result values to calculate the effects and interactions of the independent variables in the factorial experiment design.

3.3.3 Run Order

In order to reduce the effect of external factors and drift over time from internal effects, the run configurations were randomized as much as possible and the order is presented in table 3.5. Of course, every run for configuration "A" needed to be run first because that was the configuration with the "Fresh" fuel grain factor. Then, to complete the first 2^1 factorial experiments, the "E" configuration needed to be run. The "A" and "E" configurations have the same variable levels except for the fuel grain condition.

Table 3.5. Randomized DOE Run Order

Order Number	Configuration Name	Fuel Type	Eq. Ratio	Fuel Grain Condition
1	A-1	Hydrogen	0.50	Fresh
2	A-2	Hydrogen	0.50	Fresh
3	A-3	Hydrogen	0.50	Fresh
4	A-4	Hydrogen	0.50	Fresh
5	E-1	Hydrogen	0.50	Used
6	E-2	Hydrogen	0.50	Used
7	E-3	Hydrogen	0.50	Used
8	E-4	Hydrogen	0.50	Used
9	F-1	Methane	0.67	Used
10	H-1	Methane	0.50	Used
11	G-1	Hydrogen	0.67	Used
12	G-2	Hydrogen	0.67	Used
13	F-2	Methane	0.67	Used
14	H-2	Methane	0.50	Used
15	H-3	Methane	0.50	Used
16	G-3	Hydrogen	0.67	Used
17	F-3	Methane	0.50	Used

In summary, the first 8 runs were used in the first factorial experiment, resulting in a replicability of each configuration of 4. Runs 6-17 were used in the second factorial experiment. With 12 total runs and 4 different configurations, this factorial experiment had a replicability of 3.

Chapter 4

Experimental Setup and Operation

4.1 Test Stand and Rocket Hardware

The test stand where the rocket motor and sensors were mounted was built using steel slotted L-angle bars. The test stand was a rectangular prism with length, width, and height of $30in$, $24in$, and $16in$. Steel slotted flat bars were added at angles on the side faces of the test stand to add structural rigidity. The truss structure to support the thrust of the rocket was also mounted to the test stand. The truss structure was $6in$ wide and $10in$ tall with multiple thrust-bearing structural members added at various angles. The strength of the truss structure was verified by flipping the test stand on its side, and adding a static load of twice the expected thrust force using weights at the point where the thrust would be applied to the truss structure.

The rocket hardware consisted of the rails, sliders, motor case, nozzle mount block, injector block, and graphite nozzle. All the components were the same as the parts used in the previous hydrogen-torch igniter tests[50, 67] with the exception of the graphite nozzle. The motor case was held by compression between the injector block and nozzle mount block, which were mounted to the sliders and inserted onto the rails to allow one degree of freedom of the rocket's movement in the direction of the thrust.

The injector block was a 304 Stainless Steel block with two fluid inlets and two fluid outlets as shown in figure 4.1. The first inlet in the upper portion of the figure was for the axially injected oxidizer and the second inlet on the upper right side of the block

was for the radially injected Hydrogen and in this case Methane as well. The first outlet on the lower right portion of the cross section was the pressure transducer port and the second outlet at the bottom of the figure was for the oxidizer and combustion products of the ignition event to exit into the main combustion chamber. The port on the left accommodated the spark plug used during ignition.

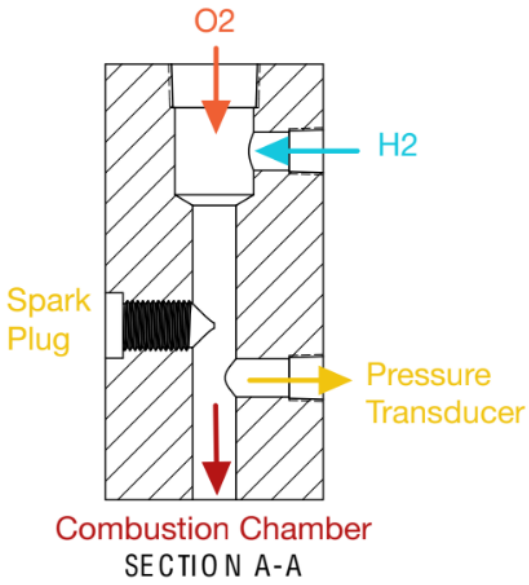

Figure 4.1. Cross Section of Injector Block[67]

The graphite nozzle was almost identical to the nozzle used prior, with the exception of the throat and exit diameters. The outer form and dimensions remained the same to be able to interface properly with the nozzle mount block. Using the desired operating pressure of $1.03MPa$ $(150psia)$ and the exit pressure taken to be $101.325kPa$ $(14.7psia)$ the exit to throat area ratio for the nozzle was found using the equations[68]

$$\frac{P_o}{P_e} = [1 + \frac{1}{2}(k-1)Ma_e^2]^{\frac{k}{k-1}} \tag{4.1}$$

$$\frac{A_e}{A_t} = \frac{1}{Ma_e}[\frac{1 + \frac{1}{2}(k-1)Ma_e^2}{\frac{1}{2}(k+1)}]^{\frac{k+1}{2(k-1)}} \tag{4.2}$$

where Ma_e is the Mach number of the exhaust at the nozzle exit. The exit to throat area ratio was calculated to be 1.95. The throat diameter was then calculated based on mass flow rates that could be achieved with the available piping equipment and expected

chamber pressure using equation 2.7. The resulting throat and exit diameters were found to be $7.62mm$ and $10.64mm$ respectively. These values are expressed in inches in the nozzle cross section shown in figure 4.2.

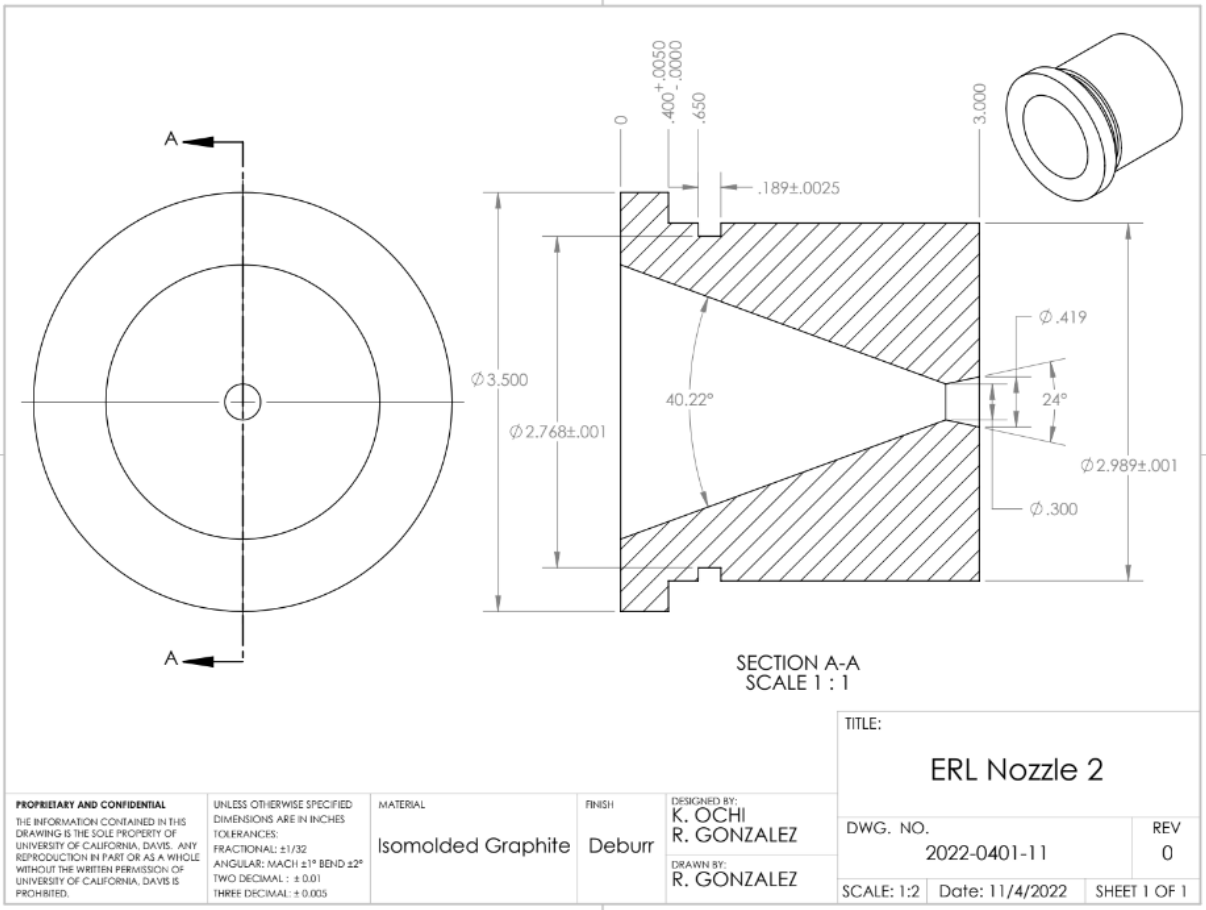

Figure 4.2. Nozzle Cross Section View

4.2 Piping and Instrumentation

In order to supply the oxidizer and igniter fuel gases to the solid fuel grain inside the hybrid motor, the following piping configuration was set up as shown in figure 4.3.

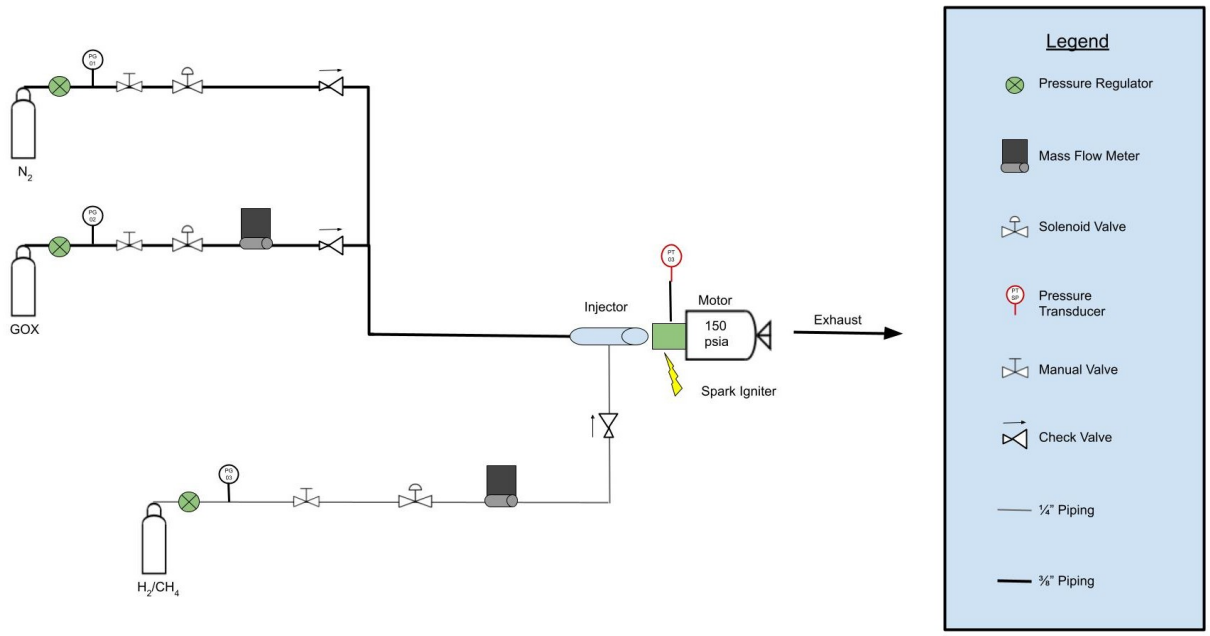

Figure 4.3. Piping and Instrumentation Diagram

The oxygen tank is connected to the injector block with 3/8" diameter piping. Immediately downstream of the tank valve is a pressure regulator where the outlet pressure would be adjusted to achieve the desired oxidizer flow rate. A manually operated hand valve after the regulator was placed in the line to ensure gas can flow only when the operators were absolutely ready to fire the motor. An electronically-controlled normally-closed (NC) solenoid valve was placed in the line followed by an Aalborg GFM77 gas flow meter to remotely open and close the oxidizer flow line and measure the oxidizer's mass flow rate. The gas flow meter is capable of measuring flow rates up to 1,000L/min. Finally, before reaching the injector block, a check valve rated for two time's the expected operating chamber pressure was placed in the oxidizer line to prevent back flow of propellants that could potentially combust with the oxygen upstream in the pipe.

The igniter fuel line is identical to the oxidizer line with the exception of using 1/4" piping to accommodate a smaller mass flow required. When a different igniter fuel is needed as indicated by the run order in table 3.5 the regulator can be easily switched between the two different fuel tanks. Finally, a nitrogen line was added so that the motor can be thoroughly flushed and any remaining flames could be smothered to safely confirm

the conclusion of each motor firing. The nitrogen line is also identical to the oxidizer line except for the fact that the nitrogen flow rate does not need to be measured, so the gas flow meter was not included. The nitrogen line runs parallel to the oxidizer line and attaches downstream of the check valves in each line. This way, any oxygen in the motor or piping up until the check valve will be pushed out of the system.

An Omega PX931-500AV pressure transducer was attached to the injector block as indicated in figure 4.1 to measure the chamber pressure during operation. The pressure transducer measures absolute pressure from 0-3.45MPa (0-500$psia$). To measure the thrust produced by the motor, an Omega LC304-500 compression load cell capable of measuring compression loads from 0-2,224N (0-500lbf), was mounted to the thrust-bearing truss structure.

4.3 Electrical and Software Systems

Three different circuits for data acquisition, solenoid valve control, and spark plug operation were constructed.

4.3.1 Data Acquisition

The data acquisition circuit was designed in-house and used an Arduino Uno microcontroller board to read the analog voltage outputs from the two gas flow meters, pressure transducer, and compression load cell. The output of the two gas flow meters were 0-5V analogue signals that scale linearly with the measured flow rate. The Arduino Uno's analogue input pins are capable of measuring analogue signals in this range with 8-bit precision so, as shown in the circuit schematic in figure 4.4 the signal outputs of the flow meters were connected to two of the Arduino's analogue input pins, denoted as 'A1' and 'A3'. A 12V DC adapter plug was used to power the flow meters.

The output for the pressure transducer and load cell were 0-30mV and 0-20mV respectively, so in order to amplify the output signals, increase resolution, and reduce noise, an AdaFruit ADS 1115 analogue-to-digital converter (ADC) was used to process the signals before being read by the Arduino processor. The maximum gain of the ADC is 16 and offers 16-bit precision. The analogue input range of the ADS 1115 ADC is +/- 4.096V

and the gain of 16 only brings the maximum signal output of the pressure transducer and load cell to $0.480V$ and $0.320V$ respectively resulting in an effective precision of 3,840 bits and 2,560 bits. The resulting resolution is then $896Pa$ $(0.13psia)$ and $0.87N$ $(0.20lbf)$. The pressure transducer and load cell were each powered by a $10V$ DC adapter plug. The ADC was powered by the $5V$ power output of the Arduino board and used the same internal clock as well. The serial clock and serial data lines between the ADC and Arduino boards were connected via the 'SCL' and 'SDA' pins. The digital pin on the Arduino board labeled 'D2' was connected to the Arduino board used for valve timing and control (not shown in figure 4.4.

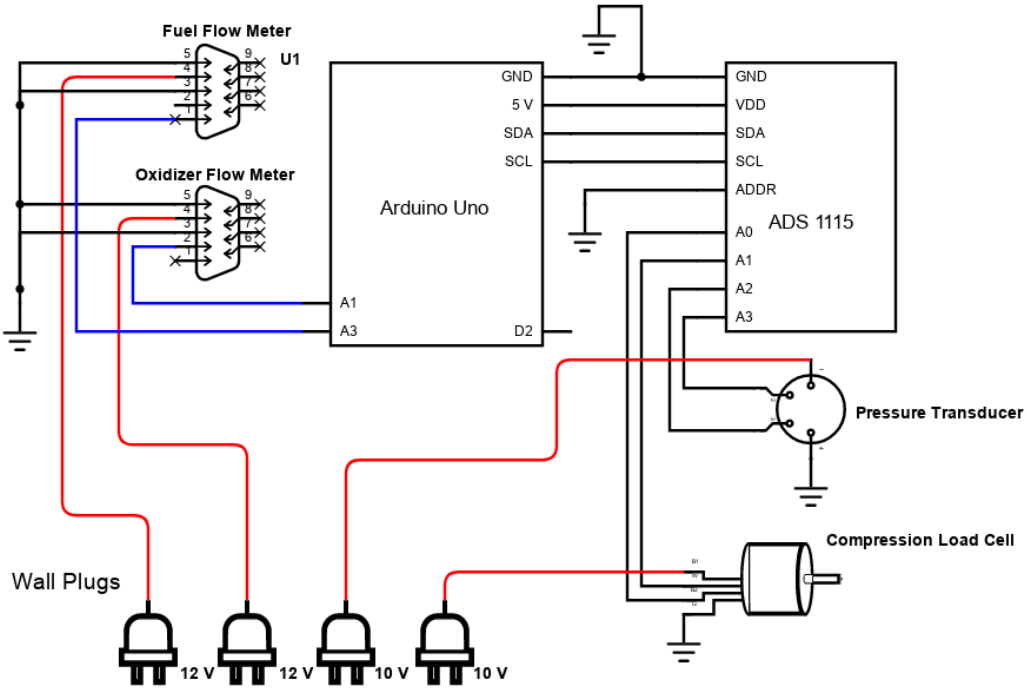

Figure 4.4. Schematic of Instrumentation Circuit

Finally, the Arduino board was connected to the main computer via a USB-A to printer cable to carry the digital data. The open-source serial communication interfacing program PuTTY was then used to log the transducer data from the Arduino, which was pre-programmed to send the data in comma-separated value format (CSV). The logged data was then saved for software-based post processing. The data acquisition program

written and uploaded to the Arduino Uno board is presented in appendix F.

4.3.2 Solenoid Valve Timing and Actuation

The solenoid valve timing and actuation was also designed in house and used a separate Arduino Uno board. The reason for using a different Arduino board was because when both the data acquisition and valve timing and actuation programs were uploaded to the same board, the processes carried out by the latter program would interfere with the timing of the data acquisition sampling rate. When both programs were separated into different boards, the timing issues were resolved.

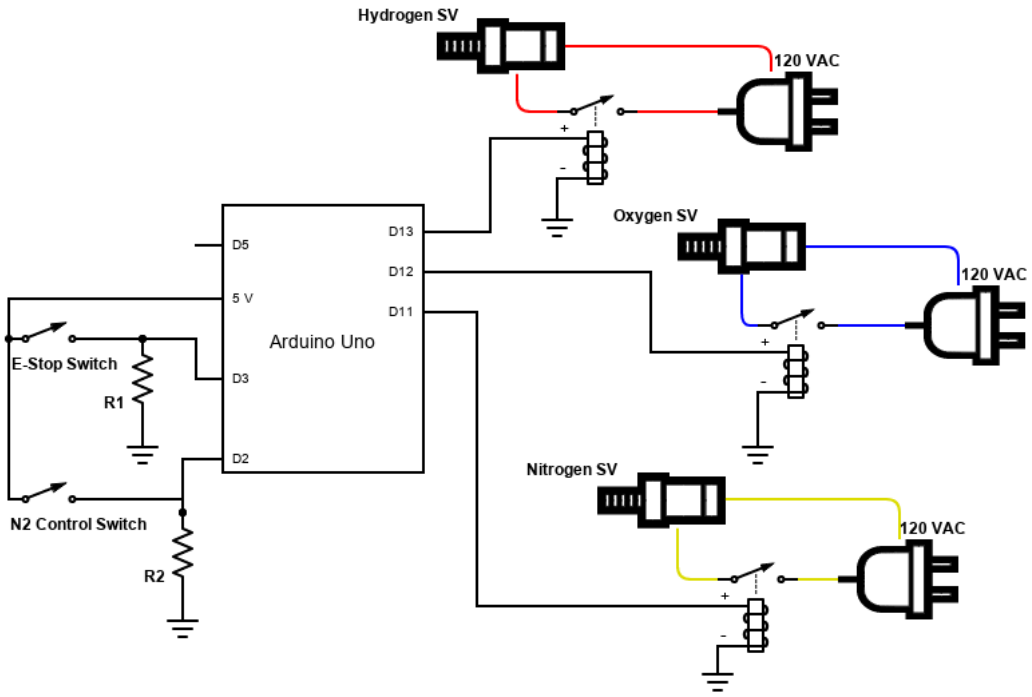

Figure 4.5. Schematic of Solenoid Valve Control Circuit

The solenoid valves used run on $120V$ AC. The valves were accordingly powered by connecting to a standard $120V$ AC wall outlet plug. The circuit between the wall plug and each valve was open at a solid state relay as shown on the right hand side of figure 4.5. The other side of the solid state relay receives direct current signals up to $5V$, so one lead was connected to a digital output pin on the Arduino board, and the other lead was connected to ground. The digital pins were then programmed to output a high signal and

therefore close the relay on the AC voltage side and thus turn on and open the solenoid valve, at specific points in time. The timing for the opening and closing of the valves is described in section 4.4.

Two additional digital pins were set as input pins and used to add manual operation capabilities. Each pin was tied to ground via a resistor and connected to the $5V$ supply across a switch. The first feature added was an emergency stop switch (E-Stop). When digital pin 'D2' was shorted to the $5V$ input (closing the E-Stop) switch, the high signal would cause the program to immediately cut any valve actuation signals coming from the output digital pins ('D11', 'D12', and 'D13'), thereby closing all valves. Shortly after, a signal is sent to open the nitrogen valve. This way, all propellants would stop flowing into the combustion chamber and Nitrogen would flow into the combustion chamber to stop the combustion and quench any remaining flames. The second feature added was manual operation of the Nitrogen-line solenoid valve. When the N2 Control Switch was closed, the $5V$ signal into digital pin 'D3' would cause the program to send a signal to open the Nitrogen valve. The valve could then be closed by opening the switch. This feature was only enabled when the program entered a "stand-by" mode. The program would enter the stand-by mode only after normal operation of the static firing sequence finished, or the E-Stop switch had been activated.

Finally, the digital pin 'D5' on this board was programmed as an output and connected to the digital pin 'D2' of the data acquisition board in figure 4.4. Shortly before the ignition event, the output pin would be set to high. This high signal would then be read by the digital pin on the instrumentation circuit Arduino board and trigger the microprocessor to start recording data. Both Arduino boards were also connected to the same ground to ensure the correct voltage potential was being written and read by both boards.

4.3.3 Spark Plug

The circuit for the spark plug, as shown in figure 4.6, was the same as used in the previous Hydrogen-Oxygen torch igniter testing campaign[50, 67].

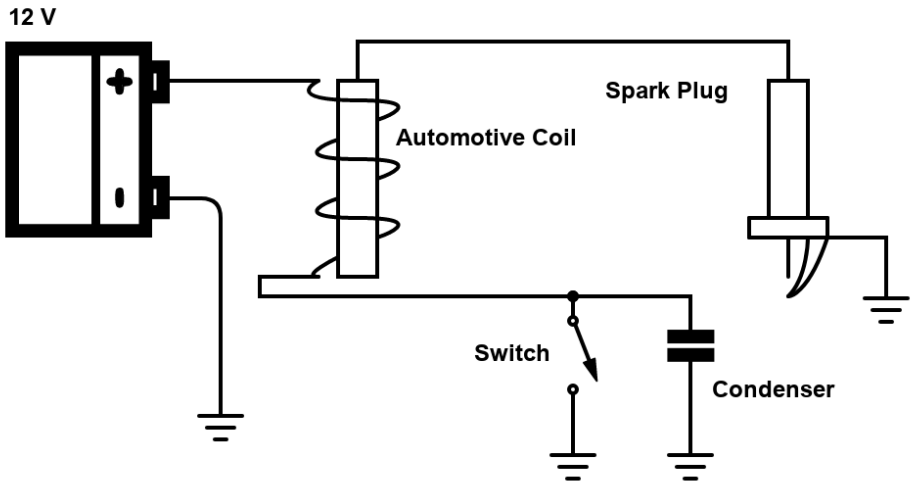

Figure 4.6. Schematic of Spark Plug Circuit

When the $12V$ battery was connected to ground via the switch, the current running through the automotive coil would induce voltages great enough to cause arcing across the spark leads to occur. The condenser was essentially a capacitor that would prevent the switch leads to spark when closing the switch. All the parts used were commercial-off-the-shelf.

4.4 Static Firing Operation

The Arduino Uno board used in the solenoid valve timing and control circuit was programmed to send the valve command signals according to the static firing sequence schedule. Upon powering the Arduino board, the pre-programmed timer would initialize at t-10 seconds where t=0 seconds is defined as the beginning of the ignition event. The programmed timer was a counter that was triggered by a $200Hz$ timer interrupt. The counter would correspondingly increment the elapsed time by 5 milliseconds. At t-2 seconds the command signal to open the oxygen solenoid valve was sent, and the signal to trigger the start of data logging was sent to the Arduino board in the instrumentation circuit. At t=0, the command signal to open the igniter fuel line was sent. In between the two previous events, manual operation of the spark plug began, this way, at t=0 all three things necessary for the ignition event (oxidizer, fuel, ignition heat source) were present

and defined as the beginning of the ignition event.

At t+2.5 seconds, the command signal to keep the igniter fuel solenoid valve was turned off. To have a burn of 10 seconds, the command signal to keep the oxidizer solenoid valve open was turned off at t+10 seconds followed by opening the nitrogen solenoid valve for an additional 10 seconds. Once the nitrogen solenoid valve was closed, the programmed valve control sequence entered manual mode where the nitrogen valve was able to be operated by the nitrogen valve control switch. This way, more nitrogen could be used to further flush the system as needed to ensure the fuel grain was no longer able to ignite.

Chapter 5

Data Collection and Analysis Methods

5.1 Pressure, Thrust, and Mass Flow Rate Calculation

As mentioned in the previous chapter the Arduino Uno board used in the instrumentation circuit sent the logged data to the main computer in CSV format. A python script was written to parse the file and extract the data into vector arrays. The data, however, was stored as the digitally-mapped integer value of the corresponding analogue signal at the time each data sample was taken. So, in order to convert the data to the physically measured units, equation 5.1 was used for the pressure transducer and load cell.

$$P_o = \frac{DV_rK_c}{G(2^{15})} \tag{5.1}$$

The digital integer (D) was first converted to the corresponding analogue voltage by multiplying by the voltage range (V_r), and dividing by the bit precision of the ADC. It should be noted that the ADC could read from positive $4.096V$ to -$4.096V$, so to account for the fact that negative voltages would not be read, the equivalent precision was 15 bits rather than 16 if the full range was utilized. Then, multiplying the conversion factor (K_c) from voltage to pressure for the pressure data (and likewise voltage to force for the load cell) and dividing by the gain applied (G) the real measured unit values

were obtained. The conversion factor from voltage to pressure was found by dividing the maximum pressure value the transducer was capable of reading by the excitation voltage and transducer voltage sensitivity value. The same calculation was done to find the conversion factor from voltage to force for the load cell. The relevant data for the pressure transducer and load cell could be found in the data sheets in appendix C and D. In equation 5.1 since pressure is used as an example, from the transducer data sheet K_c would be equal to $115 MPa/V$ (16,667$psia/V$). The conversion factor for the load cell is 111,205N/V (25,000lbf/V).

To convert the digital integers of the mass flow meter outputs into mass flow rates, the raw data was first converted into the corresponding analogue voltage by multiplying the maximum readable voltage and dividing by the bit precision value, which in the case of the analogue input pins for the Arduino Uno board would be 8 bits. Then the conversion factor from voltage to liters per minute was multiplied. This conversion factor was just the quotient of the maximum measurable flow rate ($1000 L/min$) and maximum output voltage ($5V$). To convert the values into a mass flow rate of grams per second the density of the gas was multiplied and divided by 60 to convert the time unit from minutes to seconds. Finally, the results needed to be multiplied by the manufacturer-specified 'K-factor' (K_a) because the flow meters were calibrated with a different gas. These values and an example calculation using the K-factor can be found in appendix E.

$$\dot{m}_g = \frac{V_r K_c \rho_g K_a}{60 \times (2^8)} \tag{5.2}$$

In equation 5.2 the subscripts for the mass flow rate and density of 'g' was used to denote any individually flowing gas.

5.2 Regression Rate, Characteristic Exhaust Velocity, and Specific Impulse Calculation

Once the raw data was converted into the relevant units, the hybrid rocket motor performance metrics could be calculated. These performance metrics are the regression rate, characteristic exhaust velocity (c*), and specific impulse (I_{sp}).

The regression rate would be characterized using the time-space average calculated by equation 2.5. Equation 2.9 at $t = t_b$ would be used to find the final radius. Both equations are presented again below for reference.

$$r_f = r(t_b) = \sqrt{r_i^2 + \frac{\Delta m_f}{\pi \rho_f L}}$$

$$\overline{\dot{r}} = \frac{r_f - r_i}{t_b}$$

The equations to find the c* and specific impulse have already been introduced in section 1.1.2. The definition of specific impulse will be shown again here for convenience.

$$I_{sp} = \frac{\int F dt}{m_p g_o}$$

where the integral of the thrust data would be evaluated numerically using the trapezoidal rule. Equation 1.4 for c* was the theoretical version of the equation used for analysis such as in the CEA program. The experimental version of the equation would be used and is defined as

$$c^* = \frac{A_t \overline{P_o}}{\overline{\dot{m}_p}} \tag{5.3}$$

where $\overline{\dot{m}_p}$ is the time-averaged propellant flow rate. In order to find the time-averaged propellant flow rate, the mean oxidizer flow over the course of the burn measured by the gas flow meter would be added to the total measured mass difference of the fuel grain after the burn, normalized by the burn time, in other words:

$$\overline{\dot{m}_p} = \overline{\dot{m}_{ox}} + \frac{\Delta m_f}{t_b} \tag{5.4}$$

5.3 Determination of Ignition Latency

It can be seen that the pressure history of rockets typically look similar to the step response of a first order system. This response is given by the equation

$$B(t) = B_{ss}(1 - e^{t/\tau}) \tag{5.5}$$

where τ is the time constant of the system, B is some arbitrary output variable, and B_{ss} is the steady state value of the output. The definition of the time constant in a first order system is the time it takes for the response output to change by approximately 63.2% of the difference between the initial and steady state value. An example of a first order system response is shown in figure 5.1.

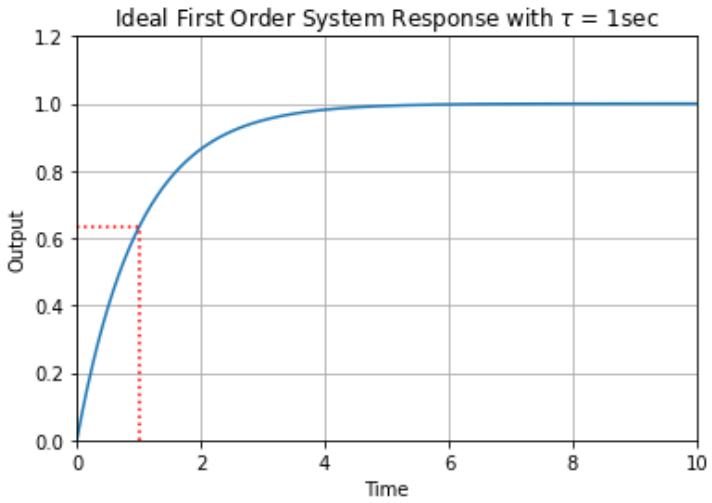

Figure 5.1. Example of First Order Step Response

As indicated by the red dotted lines, at a time value equal to the time constant, the output is at 63.2% of the difference between the initial and steady state values. Because of this similarity in appearance between typical chamber pressure time history data and an ideal first order system response, the "time constant" of the motors pressure rise is defined as the ignition latency. This is the same method of determining ignition latency as in[29].

A python script using the curve fit function from the 'scipy.optimize' library was written to fit the collected pressure data into a first order function. The curve fitting function returns equation coefficients in which the time constant variable in the first order response function could be extracted.

Chapter 6

Results and Discussion

After finishing the experiment campaign, all the data was collected and analyzed by the methods presented in the previous chapter. Then, the effects, interactions, and signal-to-noise ratios for each variable with respect to a different rocket performance metric were calculated as outlined by the methods in [66]. The signal-to-noise ratio for all the performance metrics are summarized in the table below.

Table 6.1. Signal-to-Noise Ratios for all Independent Variables and Rocket Performance Metrics

Variable Label	E_1	E_2	E_3	$I_{1,2}$
Nylon-6 Flow Rate	9.168	-3.456	6.992	-0.210
Regression Rate	7.770	-4.882	22.552	-3.588
Steady State Pressure	0.490	0.090	4.618	-0.074
Maximum Pressure	8.588	1.576	-10.622	-3.378
Steady State c^*	1.398	-2.044	7.334	-2.234
Maximum c^*	6.406	-0.589	-5.554	-2.632
τ_r	-4.472	-0.586	-1.823	3.798
τ_f	-6.704	0.966	-0.956	-0.320
Ignition Delay	-3.772	-0.158	-2.148	0.902

In the first row of the table, the variable 'E_1' is for the effect of the fuel type used, either Hydrogen or Methane. 'E_2' is the effect of equivalence ratio, 'E_3' is the effect of fuel grain

condition, and finally 'I_{12}' is the interaction between the fuel type and equivalence ratio variables. The cells highlighted in green are significant to a 95% confidence level. The significance of each effect or interaction is determined by comparing the signal-to-noise ratio with the corresponding value in the student t-table[69].

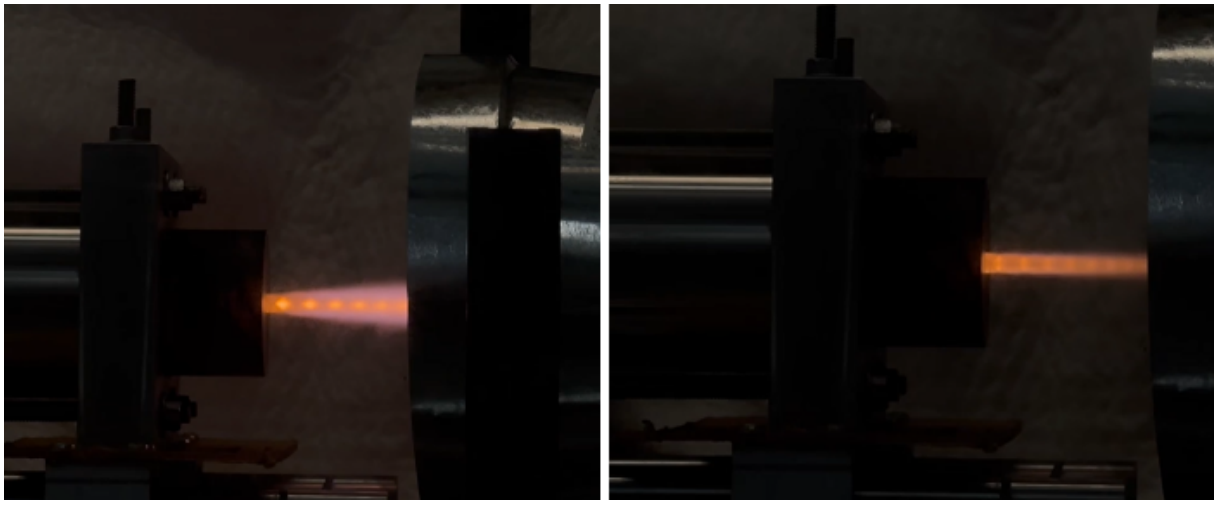

Figure 6.1. Experiment Run H-2 at t< 2.5*sec* (left) and t> 2.5*sec* (right)

During the experiment, the phenomenon of having an initially larger chamber pressure during the ignition event compared to the steady state operation was observed. This confirms trends that were observed in the previous Hydrogen torch experiments [50]. Figure 6.1 shows the same rocket firing at two time steps. The widening under expanded flame is clearly visible and visually larger than the close-to-isentropically expanded flame later on the right hand side. All the pressure plots showed the initial pressure rise to be higher than the steady state operating pressure for the hybrid motor with the corresponding pressure plot for the flames in figure 6.1 shown below. It appears that the motor operates with two first order responses, with the final steady state value changing due to changing conditions. In this case the changing conditions is having the igniter fuel flowing to the igniter fuel not flowing.

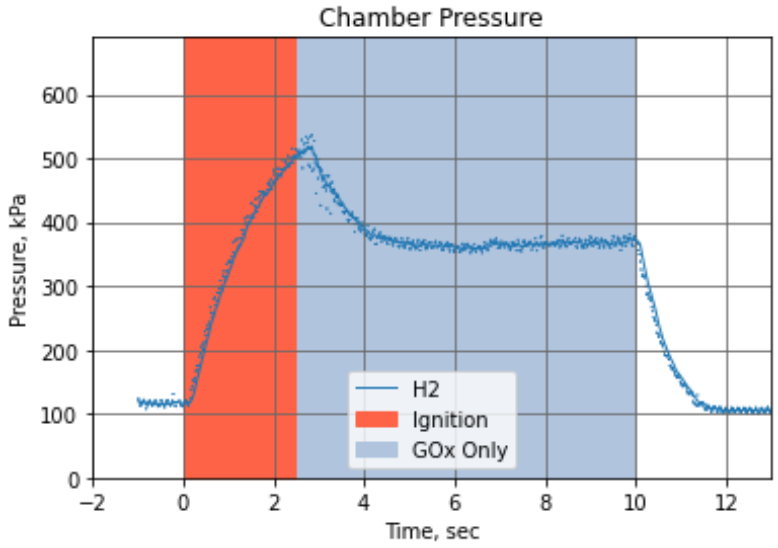

Figure 6.2. Pressure Plot for Experiment Run H-2

Because of this phenomenon, instead of finding one time constant for the pressure rise, the data were split into two sections, and two time constants, one for the rising portion and one for the falling portion, were found. The results for this are displayed as τ_r for the rising portion time constant and τ_f for the falling portion time constant in table 6.1.

Unfortunately, due to unknown issues, when running the data acquisition, the force transducer was unable to output reliable data, and also disrupted the output of the pressure transducer's data. When the force transducer was removed from the system, everything functioned as expected. Thankfully, all of the expected data analysis could still be done. The only performance metric that would not be evaluated is the specific impulse and thrust.

6.1 Regression Rate Performance

6.1.1 Effect of Fuel Type on Regression and Nylon-6 Flow Rate

According to table 6.1, the regression rate was affected by all variables. The SNRs show that the regression rates tended to be higher when using Hydrogen. This makes sense because Hydrogen can burn hotter and with more energy than Methane, thus providing more heat to the Nylon-6 surface to pyrolyze as predicted in Chapter 3. Table 6.2 summarizes the average linear regression rates for the four configurations.

Table 6.2. Average Regression Rate For Each Run Configuration

Configuration	Fuel	ϕ	Regression Rate (cm/sec)
E	Hydrogen	0.50	0.00735
F	Methane	0.50	0.00514
G	Hydrogen	0.67	0.00570
H	Methane	0.67	0.00489

The regression rates found in configuration 'E' were found to be significantly larger than the other configurations. This is an unfortunate consequence of the limited fuel grains available. Since all the runs for the 'E' configuration needed to be run first, they all had larger initial fuel port radii and therefore smaller fuel port areas. For constant Oxygen mass flow rates across all the tests, this meant the oxidizer mass flux, in which the regression rate is highly dependent, was much larger for the runs in configuration 'E'.

To work around this flaw, the time-averaged Nylon-6 flow rates were compared to remove the initial fuel port radius dependence. The results showed that using Hydrogen for ignition still burns and pyrolyzes more solid fuel than Methane, with a positive and statistically significant SNR of 9.168. The average Nylon-6 flow rate for all the runs with Hydrogen was $3.197 g/sec$, and $2.760 g/sec$ when Methane was used. Again, the results for the amount of Nylon-6 pyrolyzed agrees with the predictions made in Chapter 3.

6.1.2 Effect of Fuel Grain Condition on Regression and Nylon-6 Flow Rate

The regression rate was most significantly affected by the fuel grain condition. The regression rate being significantly affected by the fuel grain condition makes sense because of the oxidizer flux dependence and fresh fuel grains having smaller fuel port areas as explained previously. To illustrate this point further, table 6.3 shows the regression rates of individual tests along with the initial fuel port radius for each test. The particular set of runs presented in the table were selected because all the tests were conducted on the same fuel grain.

Table 6.3. Initial Fuel Port Radius and Regression Rate Data

Run	Initial Fuel Port Radius (cm)	Regression Rate (cm/sec)
A-3	1.293	0.01181
E-3	1.828	0.00744
G-1	2.068	0.00633
G-2	2.305	0.00552
G-3	2.432	0.00525

Again, to work around this flaw, the Nylon-6 flow rate for the 'A' configuration and 'E' configuration were compared and presented in the table below.

Table 6.4. Average Nylon-6 Flow Rate Data For Fuel Grain Condition Study

Configuration	Fuel	ϕ	Fuel Grain Condition	Nylon-6 Flow Rate (g/sec)
A	Hydrogen	0.50	Fresh	3.638
E	Hydrogen	0.50	Used	3.288

The average of Nylon-6 flow rates for all the runs in the 'A' configuration was larger than the average for the runs in the 'E' configuration, with the SNR from table 6.1 indicating that this difference was statistically significant. It appears that not only the regression rate is affected by initial size of the fuel port radius but also the sheer amount of solid fuel pyrolyzed.

6.1.3 Effect of Equivalence Ratio on Regression and Nylon-6 Flow Rate

Contrary to what was expected and the results from [50] the effect of the equivalence ratio showed that with a smaller equivalence ratio (more lean and further from stoichiometric conditions) the regression rates and base Nylon-6 flow rates were greater than when a larger equivalence ratio was used.

Table 6.5. Average Nylon-6 Flow Rate for Each Run Configuration

Configuration	Fuel	ϕ	Nylon-6 Flow Rate (g/sec)
E	Hydrogen	0.50	3.288
F	Methane	0.50	2.837
G	Hydrogen	0.67	3.107
H	Methane	0.67	2.683

As shown in the table above, comparing configurations E and G, the flow rate of Nylon-6 is larger with the 0.50 equivalence ratio. The same trend is observed with the two Methane configurations F and H.

6.2 Pressure and Characteristic Exhaust Velocity (c^*)

Although the thrust force was not able to be measured, the chamber pressure and c^* are good indicators of what the thrust could be, at least to reference between tests. According to table 6.1 varying the equivalence ratio for both Methane and Hydrogen had no statistically significant effect on the minimum or maximum pressure or c^*.

6.2.1 Effect of Fuel Type on Pressure and c^*

The choice of igniter fuel was statistically insignificant on the steady state chamber pressure and c^* which makes sense because during the steady state burn the igniter fuel was not flowing and therefore not taking part in the combustion process. When looking at the peak chamber pressure and c^* when the igniter fuel was taking part in the combustion, igniting the motor with Hydrogen had a significant effect in generating a larger peak pressure.

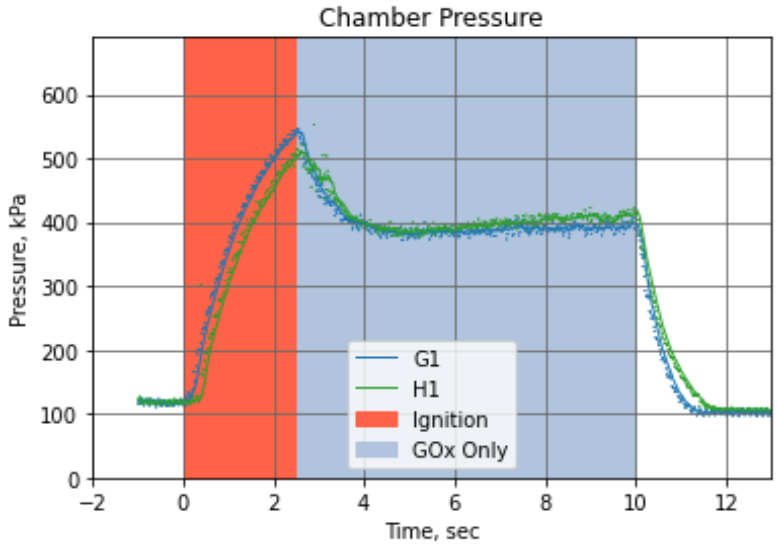

Figure 6.3. Chamber Pressure for High Equivalence Ratio and Hydrogen (G1) vs Methane (H1)

When comparing the pressure for when Hydrogen vs Methane were used at the same equivalence ratios, the peak pressure difference is visually apparent. This result is expected based on the theoretical flame temperatures, c*, and heat of combustion being larger for Hydrogen and therefore allowing it to burn with more energy and pressurize the combustion chamber more than Methane.

It would naturally follow that the peak c* would be larger when using Hydrogen not only because of the c* graphs in figure 3.4 but because the experimentally measured c* and chamber pressure are directly proportional, according to equation 5.3. The average maximum c* values for each configuration are presented in the table below along with the maximum pressures.

Table 6.6. Average Peak Pressure and c* for each Run Configuration

Configuration	Fuel	ϕ	Peak Pressure (kPa)	Peak c* (m/sec)
E	Hydrogen	0.50	550.2	1403.1
F	Methane	0.50	464.0	1131.8
G	Hydrogen	0.67	539.9	1319.1
H	Methane	0.67	501.2	1197.6

Since a smaller flow rate of Hydrogen is needed to reach the same equivalence ratio as Methane, it would seem that dividing the experimental c* equation by a smaller denominator would further increase the c* value and thus the fuel choice would have a more significant effect on the maximum c* than the maximum pressure. However, the SNRs for maximum pressure and maximum c* are 8.588 and 6.406 respectively. This result is likely due to more variance in the c* results from more uncertainty in measuring two flow rates (the oxidizer and igniter fuel) and the pressure, rather than just measuring the maximum pressure.

6.2.2 Effect of Fuel Grain Condition on Pressure and c*

When comparing the chamber pressure and c* values for the fresh vs used fuel grains, it was found that the maximum pressure and c* were both larger for used fuel grains, and the steady state pressure and c* were larger for used fresh grains. Figure 6.4 below represents this by plotting the chamber pressure for one representative run from each configuration.

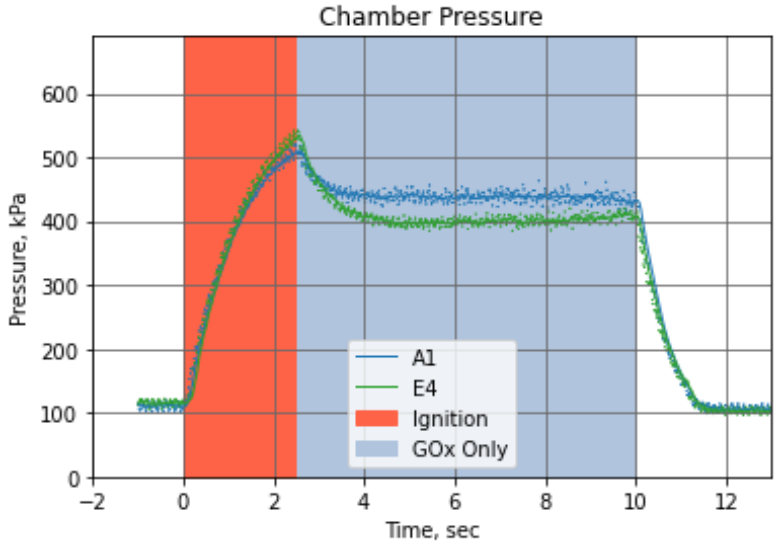

Figure 6.4. Chamber Pressure for Low Equivalence Ratio, Hydrogen and Fresh Fuel Grain (A1) vs Used Fuel Grain(E4)

The steady state pressure and c* being affected by the fuel grain condition makes sense because with different initial fuel port areas, the regression rates and therefore the overall rocket oxidizer to fuel ratio are different due to the oxidizer to fuel ratio shift phenomenon.

The oxidizer to fuel ratios for a single fuel grain across different tests are presented in table 6.7. Just like table 6.3, as the initial fuel port radius changes the oxidizer to fuel ratio changes. In this case, it is steadily increasing. The plots from figure 3.4 confirm that as the oxidizer to fuel ratio increases further from stoichiometric conditions the c* and pressure will steadily decrease. This means that throughout the testing campaign, as the fuel grains were used more and more, the steady state pressure and c* would decrease.

Table 6.7. Oxidizer to Fuel Ratio, Steady State Pressure, and c*

Run	O/F Ratio	Steady State Pressure (kPa)	Steady State c* (m/sec)
A-3	3.7	454.0	1137.8
E-3	4.3	427.5	1089.3
G-1	4.5	388.7	995.7
G-2	4.8	377.1	957.1
G-3	4.7	378.9	968.6

The runs chosen for table 6.7 are the same as in table 6.3 for consistency.

The larger peak chamber pressure and c* for the used fuel grains is potentially due to the first firing on each fuel grain needing to overcome moisture or other surface contaminants that hindered the ignition. Due to delays caused by the Energy Research Laboratory being moved from December 2022 to April 2023, the fuel grains in the lab were stored in a location unknown to the researchers. With the experiments not being conducted until October 2023, the extended period of time the fuel grains were stored could have likely picked up moisture and other surface contaminants. The initial fuel port holes were drilled out in the summer of 2022, well before the move. This is similar but to a lesser extent to Bulcher and Whitmore's Undergraduate Student Instrumentation Project incident where it took 3+ ignition events to clear out entrapped moisture from the fuel grains being exposed to a "Nor-Easter" storm for a few days [41].

6.3 Ignition Performance

6.3.1 Effect of Fuel Type on Ignition

With a SNR of -4.472, the effect of fuel type on the rising pressure time constant indicates that it takes longer for the chamber pressure to go from the cold flow pressure to the peak pressure at the end of the ignition event when using Methane. A negative SNR means the time constant is larger for Methane since Methane was defined as the "lower" value. A larger time constant translates to longer time to reach steady state value. To illustrate this, one run from the 'E' configuration using Hydrogen and one run from the 'F' configuration using Methane are plotted below.

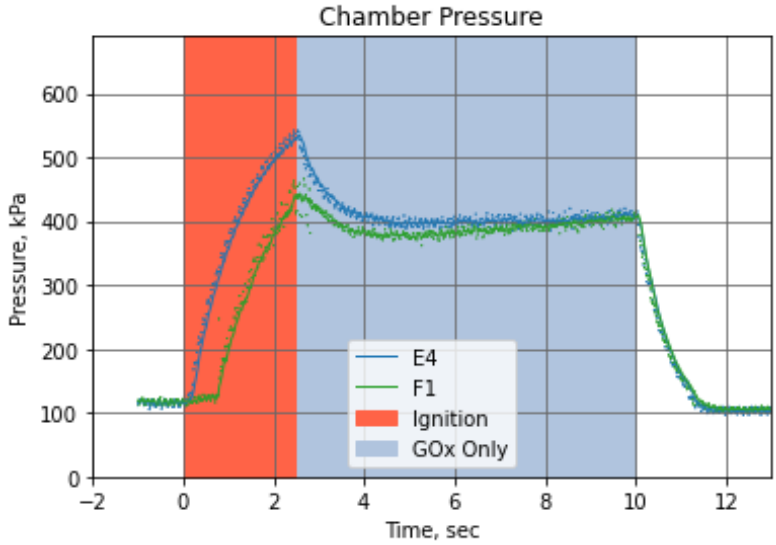

Figure 6.5. Chamber Pressure for Low Equivalence Ratio with Hydrogen (E4) vs Methane (F1)

Both runs reach the peak pressure at the same time at 2.5 seconds, coinciding with the closing of the igniter fuel valve however, the peak pressure is larger when using hydrogen. Therefore the change in pressure was much faster, resulting in a smaller time constant. The same effect and trend was observed with the time constant for the falling pressure from peak to steady state with a SNR of -6.704. The average time constants for the four configurations are summarized in the table below.

Table 6.8. Rising and Falling Time Constants

Configuration	Fuel	ϕ	τ_r (sec)	τ_f (sec)
E	Hydrogen	0.50	1.178	0.495
F	Methane	0.50	1.490	0.863
G	Hydrogen	0.67	1.293	0.577
H	Methane	0.67	1.320	0.927

When looking at the observed ignition delay, only the fuel type had a significant effect, with the ignition delay being larger when Methane is used. The run with the most significant delay at 0.855 seconds was H-3 (Methane, high equivalence ratio). The run with the smallest ignition delay was E-1 (Hydrogen, low equivalence ratio) at 0.095 seconds. The difference in when the pressure rises can be seen in figure 6.6.

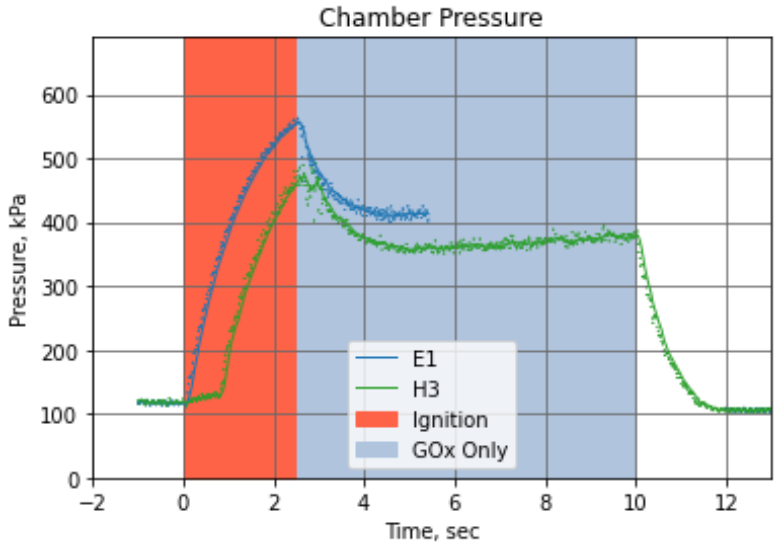

Figure 6.6. Chamber Pressure of Lowest (E1) and Highest (H3) Ignition Delay

It was found later that the reason for the observed ignition delays was likely due to the severe spark plug degradation. The same spark plug was used for all the tests in the experiment campaign. Due to the randomization of the runs for the 'F', 'G', and 'H' configurations at the end, the Hydrogen and Methane had multiple tests igniting the motor with the degraded spark plug.

Figure 6.7. New (left) vs Used (right) Spark Plug

Finally, while not included in the statistical analysis, the success rate of each fuel when attempting to ignite the motor should be discussed. In total, there were 11 runs that used Hydrogen and 6 runs that used Methane. Hydrogen was able to successfully ignite the motor on every attempt, while 4 misfires when using Methane were observed. A misfire is defined as when an experiment run was being conducted and the ignition event failed to light the solid fuel and the chamber pressure never climbed above $140kPa$. The table below summarizes the success rate of igniting the motor with each igniter fuel.

Table 6.9. Ignition Success Rate for Hydrogen and Methane

Fuel	Ignition Attempts	Ignition Successes	Success Rate
Hydrogen	11	11	100%
Methane	10	6	60%

6.4 Hydrogen Flow Time Study

Finally, after all the experiment runs in the original design matrix were completed, left-over material was available to conduct another study. Two additional configurations were run where the conditions were exactly the same as in configuration E, with the exception of the amount of time the Hydrogen would be flowing. All of the tests in the original

design space had a Hydrogen flow time of 2.5 seconds. To look into what effects changing the flow time can have, two tests where the Hydrogen was flowing for 1 second and 10 seconds were run. The chamber pressure plots for these two additional runs are shown in the figure below and compared with one of the runs from configuration E.

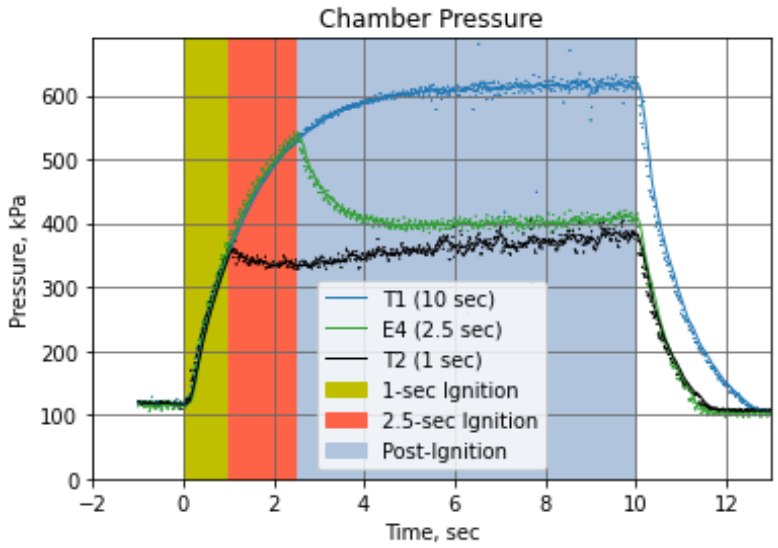

Figure 6.8. Chamber Pressure for 10 vs 2.5 vs 1 second Hydrogen Flow Time

From figure 6.8, it can be seen that the initial pressure rise, and therefore ignition characteristics for all three curves are qualitatively the same, with the pressure from the E4 and T2 runs only dropping off when the Hydrogen valve was closed. After processing the data, most of the performance metrics were found to have a strong dependence on the Hydrogen flow time with increasing performance as the Hydrogen flow time increases.

The 10 seconds flow of Hydrogen (T1) more than doubled the regression rate to $0.01010 cm/sec$ compared to the 1 second flow of Hydrogen (T2) which produced a regression rate of $0.00421 cm/sec$. The regression rate with the 2.5 seconds flow of Hydrogen (E4) was in between at $0.00710 cm/sec$. As stated before, the initial fuel port radius also has an effect on the regression rate, with smaller fuel initial fuel port radii yielding larger regression rates. Despite this fact and the initial fuel port radius of run T1 being larger than the initial fuel port radius of run E4, the regression rate for T1 was still greater than the regression rate for run E4. This is also despite the fact that with Hydrogen present

and burning with the Oxygen, there is less available Oxygen to burn with the Nylon-6 fuel. In other words, when more Oxygen was available to burn with the Nylon-6 due to no competition with Hydrogen, the regression rate was found to be lower. Furthermore, the base flow rate of Nylon-6 exhibited the same trend as the regression rate with the largest flow rate found when flowing Hydrogen for 10 seconds. The Nylon-6 flow rate in this run was also more than double the rate when Hydrogen was run for only 1 second. The data is summarized in the table below.

Table 6.10. Performance Parameters of 10 vs 2.5 vs 1 second Flow of Hydrogen

Run	T-1	E-4	T-2
Hydrogen Flow Time	10 sec	2.5 sec	1 sec
Initial Fuel Port Radius	2.525 cm	1.825 cm	2.507 cm
Regression Rate (cm/sec)	0.01010	0.00710	0.00421
Nylon-6 Flow Rate (g/sec)	6.210	3.170	2.540
Steady State Pressure (kPa)	609.8	401.3	367.1
Steady State c* (m/sec)	1334.6	1048.4	1000.1
Ignition Delay (sec)	0.150	0.175	0.155

The maximum pressure and c* were not considered here because in both of the runs where the Hydrogen flow time was changed, the maximum pressure and c* were found at the very end of the run, instead of at the end of the ignition transient. The steady state values still follow the same trends as the regression and Nylon-6 flow rates. Since Hydrogen was flowing during the steady state in run T1, the pressure and c* were found to be much higher than the steady state values in runs T2 and E4 where the values between these two runs were much closer together. This result shows the significant role augmenting the normal operation of a hybrid rocket motor with Hydrogen plays on the overall rocket performance. The steady state chamber pressure when Hydrogen was run for only 1 second or 2.5 seconds was 367.7kPa and 401.3kPa. When Hydrogen was flowing during the steady state operation, the average pressure skyrocketed to over 600kPa. Similarly, the c* increased by roughly 300m/sec when Hydrogen was present in the steady state.

This is up from the $1000 m/sec$ and $1048 m/sec$ c^* achieved when running Hydrogen for only 1 second and 2.5 seconds respectively.

Chapter 7

Conclusions and Recommendations for Future Work

7.1 Conclusions

After previous efforts to study a Hydrogen-Oxygen torch were completed, a new study was done where testing was expanded to include another fuel, Methane, to further characterize the overall ignition system performance, and do a direct side-by-side comparison of the two igniter fuels. In this study, it was found that varying the flow rate of the igniter fuel, and thus the equivalence ratio of the igniter mixture, had little to no effects on the system performance, potentially because of a small range used. Changing the fuel used, on the other hand, exhibited more major performance differences. Isolating the fuel grain condition variable was also done to check for drift in the data as the fuel grains in the experiment campaign were used more and more.

It was found that using Hydrogen significantly increased the solid Nylon-6 fuel regression rates and the base flow rate of pyrolysis by 30% and 17% respectively. While the statistical analysis showed that lowering the igniter flow rate would increase the regression rate as well, the study on the fuel grain condition and namely, the initial fuel port radius, was found to be responsible for the apparent increase in regression rate. When looking at the base Nylon-6 flow rate, changing the equivalence ratio had little to no effect. Varying the igniter fuel flow rate was found to have a significant effect on the regression rate in [50]. The difference in this study is the range of igniter fuel flow rates was much smaller

so the results at a smaller range were not as significantly different. While it is standard in the literature to measure the performance of a hybrid rocket motor through its regression rate, it is only helpful if all tests are done with fuel grains of equal initial fuel port radii. Studying the base flow rate of pyrolyzed solid fuel can remove the bias of having different fuel port radii.

In only the regression and Nylon-6 flow rate did changing the igniter fuel have any effect on the steady state performance of the rocket. When looking at the chamber pressure and characteristic exhaust velocity, the steady state values remained the same across different equivalent ratios and among both igniter fuels. The peak values at the end of the ignition event were significantly larger when Hydrogen was used compared to Methane by 13% for the pressure and 17% for c^*. This means using Hydrogen for the ignition allows the rocket to burn with more energy and have a more impulsive ignition event. This is important to note because typically, an orifice is placed in between the injector chamber and main combustion chamber to decouple the combustion processes and ensure repeatable start up transients [43]. This makes sense for missions where precise thrust control is desired, however in missions where total impulse is the higher priority such as for interplanetary travel, it would make sense to reduce the mechanical complexity of adding in the orifice and just "harvesting" the extra impulse the Hydrogen can provide during ignition.

When looking at the ignition characteristics, it was found that no variable had a statistically significant effect on the time constant of the rising portion of the pressure data. Methane was found to slightly decrease this time constant but this is potentially due to the fact that Methane is unable to reach as high of a peak pressure as Hydrogen. Also some of the runs for Methane had a delay in the initial ignition which meant that less data was available to accurately fit a first order response curve. For all the runs, however, the curves were able to fully develop from the peak pressure to a steady state value after the end of the ignition event. This means the falling portion of the pressure data was able to be more accurately fitted with a first order response curve. Due to all runs reaching roughly the same steady state pressure at around the same time and Hydrogen producing a larger peak pressure thereby having a larger difference between the initial and steady

state pressure, Hydrogen was found to have a significantly smaller time constant that was less than half than Methane. Either way, it appeared that when the pressure in the chamber reached the peak and steady state values was more of a function of the timing of the valves opening and closing rather than the type of fuel used. If the igniter fuel valve would close later, the peak pressures would be larger and appear later in the burn. On the other hand, if the igniter valve had closed earlier the peak pressures would be smaller and appear earlier.

Hydrogen was found to have fewer startup delays in the ignition process than Methane as well as a higher success rate of ignition. The ignition start up delays were attributed to spark plug degradation as only one spark plug was used to conduct all the tests. Although to have more consistent pressure graphs the spark plug should have been replaced one or more times during the experiment campaign, having both Hydrogen and Methane used on the same spark plug and only observing significant ignition delays with Methane shed light on the robustness of using Hydrogen as an igniter fuel over Methane.

Finally, varying the amount of time that Hydrogen was flowing was found to have a significant effect on the motor's performance. Comparing when Hydrogen was present in the steady state operation versus not, the regression rate was more than doubled despite having less available oxygen available to burn with the solid Nylon-6 fuel. The chamber pressure increased by 66%, and c^* also increased by more than 33%.

In this study Hydrogen increased the solid fuel regression rates, provided a more energetic and impulsive ignition event, and operated more consistently and reliably than Methane. This comes at the cost of being less volumetrically efficient than Methane as figure 3.5 shows Methane to be more dense than Hydrogen for a given temperature and pressure.

7.2 Recommendations for Future Work

7.2.1 Determination of Minimum Igniter Fuel for Successful Ignition

In this study, only a small range of igniter fuel flow rates were used to characterize the igniter performance over this range. For future propulsion system designers where the ignition fuel would need to be carried on the mission, it would be beneficial to know what the smallest possible flow rate to use for consistent and reliable ignition. Metrics to define what counts as a successful ignition would need to be developed. In a study like this, the flammability limits of the igniter fuel would have a greater impact on the results. For example, because of Hydrogen's wide flammability limits, it's possible to find that a much smaller amount of Hydrogen would be needed to be stored in a tank compared to Methane which could potentially outweigh the volumetric inefficiency drawback.

7.2.2 Spark Plug Operation Study

All of the experiments conducted were done with the spark plug being operated by hand. The spark rate and amount of time the spark plug was operated therefore had no no way to be tracked nor precisely regulated. In order to estimate and minimize the total electrical energy used to ignite the motor, future experiments can automate the timing of the spark plug, deciding how long and at what rate to operate it. Just like the previously recommended study, the minimum ignition could be found and would likely depend on factors such as the flammability limits and ignition energy of the igniter fuels used. As seen in the pressure graphs in this study, depending on the igniter conditions the amount of time it takes after beginning the operation of the spark plug can vary.

7.2.3 Injector Design Study

The reason for running the igniter in these experiments at only fuel lean conditions was to reduce the competition between the igniter fuel and the pyrolyzed Nylon-6 fuel to react with the incoming oxidizer. The injector geometry was simple with the axially injected oxidizer and the igniter fuel being injected perpendicular to the main oxidizer flow. Optimized injector designs such as the one designed in [44] could potentially change

the ignition performance due to added propellant mixing (in the case of swirl injectors) or strategically place the oxidizing species on the outside around a core flow of igniter fuel so that the oxidizer can form a barrier between the two fuel species and reduce competition.

References

[1] Oscar Biblarz and George P. Sutton. *Rocket Propulsion Elements*. Wiley and Sons, 2000.

[2] Paweł Surmacz and Grzegorz Rarata. "Hybrid Rocket Propulsion Development and Application". In: *Progress in Astronautics* (Jan. 2009).

[3] NASA. *Liquid Rocket Engine*. URL: https://www.grc.nasa.gov/WWW/K-12/rocket/lrockth.html (visited on 02/17/2022).

[4] Don Edberg and Willie Costa. *Design of Rockets and Space Launch Vehicles*. AIAA, 2022.

[5] Stephen A. Whitmore, Zachary W. Peterson, and Shannon D. Eilers. "Comparing Hydroxyl Terminated Polybutadiene and Acrylonittrile Styrene as Hybrid Rocket Fuels". In: *Journal of Propulsion and Power* 29 (2013).

[6] Md Akhter and md ashique Hassan. "Energetic Additives for Hybrid Rocket Propulsion - Review". In: Feb. 2020. DOI: 10.1109/ASET48392.2020.9118206.

[7] Grant Risha et al. "Combustion of HTPB-based solid fuels containing nano-sized energetic powder in a hybrid rocket motor". In: *37th Joint Propulsion Conference and Exhibit*. DOI: 10.2514/6.2001-3535. eprint: https://arc.aiaa.org/doi/pdf/10.2514/6.2001-3535. URL: https://arc.aiaa.org/doi/abs/10.2514/6.2001-3535.

[8] George T. Story et al. "Mars Ascent Vehicle Hybrid Propulsion Effort". In: *AIAA Propulsion and Energy 2020 Forum*. DOI: 10.2514/6.2020-3727. eprint: https://arc.aiaa.org/doi/pdf/10.2514/6.2020-3727. URL: https://arc.aiaa.org/doi/abs/10.2514/6.2020-3727.

[9] Donghee Lee, Seongjoo Han, and Heejang Moon. "Development of 200 N-class throttleable hybrid rocket motor for lunar module application". In: *FirePhysChem* 1.4 (2021). Progress in Hybrid Rocket Propulsion, pp. 251–259. ISSN: 2667-1344. DOI: https://doi.org/10.1016/j.fpc.2021.11.014. URL: https://www.sciencedirect.com/science/article/pii/S2667134421000602.

[10] Stephen A. Whitmore et al. “Consumable Spacecraft Structure with Integrated, 3-D Printed Acrylonitril Butadiene Styrene (ABS) Thrusters”. In: *AIAA Propulsion and Energy Forum* (July 2017).

[11] Grzegorz Rarata, Paweł Surmacz, and Piotr Wolanski. “Development of a Hybrid Propulsion System for Attitude Control and Orbit Change of Small Satellites”. In: Jan. 2010.

[12] Gregory Zilliac and Laura Simurda. “Continued Testing of a High Performance Hybrid Propulsion System for Small Satellites”. In: July 2015. DOI: 10.2514/MJPC15.

[13] Elizabeth T. Jens et al. “Design of Interplanetary Hybrid CubeSat and SmallSat Propulsion Systems”. In: *2018 Joint Propulsion Conference*. DOI: 10.2514/6.2018-4668. eprint: https://arc.aiaa.org/doi/pdf/10.2514/6.2018-4668. URL: https://arc.aiaa.org/doi/abs/10.2514/6.2018-4668.

[14] Sasi Kiran Palateerdham et al. “Design and Experimental Set-up of a Paraffin Based Hybrid Rocket Engine To Brake A 24U Microsatellite in a Mars Orbit”. In: Jan. 2020.

[15] G. Marxman and M. Gilbert. “Turbulent boundary layer combustion in the hybrid rocket”. In: *Symposium (International) on Combustion* 9.1 (1963), pp. 371–383. ISSN: 0082-0784. DOI: https://doi.org/10.1016/S0082-0784(63)80046-6. URL: https://www.sciencedirect.com/science/article/pii/S0082078463800466.

[16] Martin Chiaverini. “Review of Solid-Fuel Regression Rate Behavior in Classical and Nonclassical Hybrid Rocket Motors”. In: *Fundamentals of Hybrid Rocket Combustion and Propulsion*. Ed. by Martin J. Chiaverini and Kenneth K. Kuo. American Institute of Aeronautics and Astronautics, 2007. Chap. 2, pp. 37–126.

[17] Stephen A. Whitmore et al. “High Regression Rate Hybrid Rocket Fuel Grains with Helical Port Structures”. In: *Journal of Propulsion and Power* (2015).

[18] Zezhong Wang et al. “Combustion performance of a novel hybrid rocket fuel grain with a nested helical structure”. In: *Aerospace Science and Technology* 97 (2020),

p. 105613. ISSN: 1270-9638. DOI: https://doi.org/10.1016/j.ast.2019.105613. URL: https://www.sciencedirect.com/science/article/pii/S1270963819325076.

[19] Nur Arifah Binti Mohamad Jamil et al. "High entropy alloy as metal additive for hybrid rocket propellant". In: *Materials Today: Proceedings* 75 (2023). Innovative Manufacturing, Mechatronics Material Forum 2022 (iM3F 2022), pp. 140–146. ISSN: 2214-7853. DOI: https://doi.org/10.1016/j.matpr.2022.10.257. URL: https://www.sciencedirect.com/science/article/pii/S2214785322067761.

[20] Yash Pal and V. Ravi Kumar. "Thermal decomposition study of paraffin based hybrid rocket fuel containing Aluminum and Boron additives". In: *Thermochimica Acta* 655 (2017), pp. 63–75. ISSN: 0040-6031. DOI: https://doi.org/10.1016/j.tca.2017.06.002. URL: https://www.sciencedirect.com/science/article/pii/S0040603117301466.

[21] Jérôme Messineo and Toru Shimada. "Theoretical Investigation on Feedback Control of Hybrid Rocket Engines". In: *Aerospace* 6.6 (2019). ISSN: 2226-4310. DOI: 10.3390/aerospace6060065. URL: https://www.mdpi.com/2226-4310/6/6/65.

[22] Stephen A. Whitmore, Zachary W. Peterson, and Shannon D. Eilers. "Closed-Loop Precision Throttling of a Hybrid Rocket Motor". In: *Journal of Propulsion and Power* 30.2 (2014), pp. 325–336. DOI: 10.2514/1.B34924. eprint: https://doi.org/10.2514/1.B34924. URL: https://doi.org/10.2514/1.B34924.

[23] Stephen A. Whitmore and Stephen L. Merkley. "Effects of Radiation Heating on Additively Printed Hybrid Fuel Grain O/F Shift". In: *AIAA Propulsion and Energy Forum* (July 2016).

[24] Guy Langelle. "Solid-Fuel Pyrolysis Phenomena and Regression Rate, Part 1: Mechanisms". In: *Fundamentals of Hybrid Rocket Combustion and Propulsion*. Ed. by Martin J. Chiaverini and Kenneth K. Kuo. American Institute of Aeronautics and Astronautics, 2007. Chap. 3, pp. 127–166.

[25] Jason Rabinovitch et al. "Characterization of PolyMethylMethAcrylate as a Fuel for Hybrid Rocket Motors". In: July 2018. DOI: 10.2514/6.2018-4530.

[26] Bonnie J Mcbride Sanford Gordon. "Computer program for calculation of complex chemical equilibrium compositions and applications. Part 1: Analysis". In: (1996).

[27] Gregory Zilliac and Arif Karabeyoglu. "Hybrid Rocket Fuel Regression Rate Data and Modeling". In: *Collection of Technical Papers - AIAA/ASME/SAE/ASEE 42nd Joint Propulsion Conference* 3 (July 2006). DOI: 10.2514/6.2006-4504.

[28] Arif Karabeyoğlu, Elena Toson, Brian Evans, et al. "'O/F shift'in hybrid rockets". In: *50th AIAA/ASME/SAE/ASEE Joint Propulsion Conference 2014*. Curran Associates. 2014, pp. 5237–5255.

[29] Stephen A. Whitmore and Cara I. Frishkorn. "Analyzing and Reducing Ignition Latency of a Nytrox/ABS Hybrid Propulsion System". In: *AIAA Propulsion and Energy Forum* (Aug. 2020).

[30] Stephen A. Whitmore. "Three-Dimensional Printing of "Green" Fuels for Low-Cost Small Spacecraft Propulsion Systems". In: *Journal of Spacecraft and Rockets* 55 (2018).

[31] Robert Shanks and Mitchell Hudson. "A Labscale Hybrid Rocket Motor for Instrumentation Studies". In: (July 2023).

[32] David M. Dyrda, Veronika Korneyeva, and Brian J. Cantwell. "Diode Laser Ignition Mechanism for Hybrid Propulsion Systems". In: *Journal of Propulsion and Power* 36.6 (2020), pp. 901–911. DOI: 10.2514/1.B37834. eprint: https://doi.org/10.2514/1.B37834. URL: https://doi.org/10.2514/1.B37834.

[33] David Dyrda et al. "Diode Laser Ignition Testing for PMMA/GOX Hybrid Motors". In: *AIAA Propulsion and Energy 2019 Forum*. DOI: 10.2514/6.2019-4095. eprint: https://arc.aiaa.org/doi/pdf/10.2514/6.2019-4095. URL: https://arc.aiaa.org/doi/abs/10.2514/6.2019-4095.

[34] David Dyrda and Brian J. Cantwell. "Development of a Laser Ignition Scheme for Hybrid Rocket Motors". In: *2018 Joint Propulsion Conference*. DOI: 10.2514/6.2018-4444. eprint: https://arc.aiaa.org/doi/pdf/10.2514/6.2018-4444. URL: https://arc.aiaa.org/doi/abs/10.2514/6.2018-4444.

[35] John J. Rusek. "New decomposition catalysts and characterization techniques for rocket-grade hydrogen peroxide". In: *Journal of Propulsion and Power* 12.3 (1996), pp. 574–579. DOI: 10.2514/3.24071. eprint: https://doi.org/10.2514/3.24071. URL: https://doi.org/10.2514/3.24071.

[36] Vadim Zakirov et al. "Surrey research on nitrous oxide catalytic decomposition for space applications". In: *In, Proceedings of the 14th Annual AIAA/USU Conference on Small Satellite* (Jan. 2000).

[37] E. J. Wernimont and S. D. Heister. "Combustion Experiments in Hydrogen Peroxide/Polyethylene Hybrid Rocket with Catalytic Ignition". In: *Journal of Propulsion and Power* 16.2 (2000), pp. 318–326. DOI: 10.2514/2.5571. eprint: https://doi.org/10.2514/2.5571. URL: https://doi.org/10.2514/2.5571.

[38] Stephen A. Whitmore, Nathan R. Inkley, and Daniel P. Merkley. "Development of a Power Efficient, Restart-Capable Arc Ignitor for Hybrid Rockets". In: *AIAA Propulsion and Energy Forum* (July 2014).

[39] Spencer D. Mathias, Stephen A. Whitmore, and Richard Harvey. "High Voltage Breakdown and Arc-Tracking Mechanism of Thermoplastics with Applications to Hybrid Rocket Arc-Ignition". In: *AIAA Propulsion and Energy Forum* (July 2017).

[40] Stephen A. Whitmore et al. "Development of a Power-Efficient, Restart-Capable Arc Ignitor for Hybrid Rockets". In: *Journal of Propulsion and Power* 31 (2015).

[41] Anthony M. Bulcher and Stephen A. Whitmore. "A Green Hybrid Thruster Using Moderately Enriched Compressed Air as the Oxidizer". In: *AIAA Propulsion and Energy Forum* (July 2018).

[42] Luis E. Sanchez et al. "Development and Testing of a O ¡sub¿2¡/sub¿/CH ¡sub¿4¡/sub¿ Torch Igniter for Propulsion Systems". In: *52nd AIAA/SAE/ASEE Joint Propulsion Conference*. DOI: 10.2514/6.2016-4975. eprint: https://arc.aiaa.org/doi/pdf/10.2514/6.2016-4975. URL: https://arc.aiaa.org/doi/abs/10.2514/6.2016-4975.

[43] Antonietta Conte et al. "Design, Modeling and Testing of a O_2/CH_4 Igniter for a Hybrid Rocket Motor". In: *AIAA Aviation Forum* (2018).

[44] Olexiy Shynkarenko and Domenico Simone. "Oxygen-Methane Torch Ignition System for Aerospace Applications". In: *Aerospace* (Aug. 2020).

[45] Elizabeth T. Jens et al. "Low Pressure Ignition Testing of a Hybrid SmallSat Motor". In: *AIAA Propulsion and Energy 2019 Forum*. DOI: 10.2514/6.2019-4009. eprint: https://arc.aiaa.org/doi/pdf/10.2514/6.2019-4009. URL: https://arc.aiaa.org/doi/abs/10.2514/6.2019-4009.

[46] Ryan W. Conversano et al. "SmallSat Missions Enabled by Paired Low- Thrust Hybrid Rocket and Low-Power Long-Life Hall Thruster". In: *2019 IEEE Aerospace Conference*. 2019, pp. 1–8. DOI: 10.1109/AERO.2019.8741678.

[47] Flora S. Mechentel and Brian J. Cantwell. "Small-scale Gaseous Oxygen Hybrid Rocket Testing Facility Upgrades for Regression Rate and Combustion Efficiency Studies". In: *2018 Joint Propulsion Conference*. DOI: 10.2514/6.2018-4439. eprint: https://arc.aiaa.org/doi/pdf/10.2514/6.2018-4439. URL: https://arc.aiaa.org/doi/abs/10.2514/6.2018-4439.

[48] Flora S. Mechentel and Brian J. Cantwell. "Small-scale Gaseous Oxygen Hybrid Rocket Testing Facility Upgrades for Regression Rate and Combustion Efficiency Studies". In: *2018 Joint Propulsion Conference*. DOI: 10.2514/6.2018-4439. eprint: https://arc.aiaa.org/doi/pdf/10.2514/6.2018-4439. URL: https://arc.aiaa.org/doi/abs/10.2514/6.2018-4439.

[49] Kevin Breisacher and Kumud Ajmani. *LOX/Methane Main Engine Glow Plug Igniter Tests and Modeling*. Tech. rep. NASA, 2009.

[50] Kellen K. Ochi and Paul A. Erickson. "Effects of hydrogen–oxygen torch igniter combustion to an ABS-GOx hybrid rocket system". In: *International Journal of Hydrogen Energy* 48.14 (2023), pp. 5668–5680. ISSN: 0360-3199. DOI: https://doi.org/10.1016/j.ijhydene.2022.11.145. URL: https://www.sciencedirect.com/science/article/pii/S0360319922054398.

[51] George A. Repas. "Hydrogen-Oxygen Torch Igniter". In: (1994).

[52] Irvin Glassman, Richard A. Yetter, and Nick G. Glumac. *Combustion, 5th Edition*. Academic Press, 2015.

[53] F. Amrouche et al. "An experimental analysis of hydrogen enrichment on combustion characteristics of a gasoline Wankel engine at full load and lean burn regime". In: *International Journal of Hydrogen Energy* 43.41 (2018), pp. 19250–19259. ISSN: 0360-3199. DOI: https://doi.org/10.1016/j.ijhydene.2018.08.110. URL: https://www.sciencedirect.com/science/article/pii/S0360319918326545.

[54] F. Amrouche et al. "An experimental investigation of hydrogen-enriched gasoline in a Wankel rotary engine". In: *International Journal of Hydrogen Energy* 39.16 (2014), pp. 8525–8534. ISSN: 0360-3199. DOI: https://doi.org/10.1016/j.ijhydene.2014.03.172. URL: https://www.sciencedirect.com/science/article/pii/S0360319914008647.

[55] "Boundary-layer combustion in propulsion". In: *Symposium (International) on Combustion* 11.1 (1967), pp. 269–289. ISSN: 0082-0784. DOI: https://doi.org/10.1016/S0082-0784(67)80153-X. URL: https://www.sciencedirect.com/science/article/pii/S008207846780153X.

[56] Bonnie J Mcbride Sanford Gordon. "Computer program for calculation of complex chemical equilibrium compositions and applications. Part 1: Analysis". In: (1994).

[57] D. Cecere, E. Giacomazzi, and A. Ingenito. "A review on hydrogen industrial aerospace applications". In: *International Journal of Hydrogen Energy* 39.20 (2014), pp. 10731–10747. ISSN: 0360-3199. DOI: https://doi.org/10.1016/j.ijhydene.2014.04.126. URL: https://www.sciencedirect.com/science/article/pii/S0360319914011847.

[58] H. F. Coward and G. W. Jones. *Limits of Flammability of Vapors and Gases*. United States Government Printing Office, 1952.

[59] National Institute of Standards and Technology. *Thermophysical Properties of Fluid Systems*. URL: https://webbook.nist.gov/chemistry/fluid/ (visited on 06/22/2023).

[60] Jeannette Plante and Brandon Lee. *Environmental Conditions for Space Flight Hardware - A Survey*. Tech. rep. NASA, 2004.

[61] Valcor Engineering. *Valcor Debuts New CubeSat Propellant Tanks*. URL: https://www.valcor.com/valcor-debuts-new-cubesat-propellant-tanks/ (visited on 06/23/2023).

[62] Luis Eduardo Snachez. "Development and Testing of Oxygen/Methane Torch Igniter Technologies for Propulsion Systems". PhD thesis. University of Texas at El Paso, 2016.

[63] Virginia P. Dawson and Mark D. Bowles. *Taming Liquid Hydrogen: The Centaur Upper Stage Rocket 1958-2002*. National Aeronautics and Space Administration Office of External Relations, 2004.

[64] Thomas A. Sullivan et al. "In-situ-produced methane and methane/carbon monoxide mixtures for return propulsion from Mars". In: *Journal of Propulsion and Power* 11.5 (1995), pp. 1056–1062. DOI: 10.2514/3.23935. eprint: https://doi.org/10.2514/3.23935. URL: https://doi.org/10.2514/3.23935.

[65] Adrien J. Boiron and Brian Cantwell. "Hybrid Rocket Propulsion and In-Situ Propellant Production for Future Mars Missions". In: *49th AIAA/ASME/SAE/ASEE Joint Propulsion Conference*. DOI: 10.2514/6.2013-3899. eprint: https://arc.aiaa.org/doi/pdf/10.2514/6.2013-3899. URL: https://arc.aiaa.org/doi/abs/10.2514/6.2013-3899.

[66] John S. Lawson and John Erjavec. *Modern Statistics for Engineering and Quality Improvement*. Duxbury Press, 2000.

[67] Kellen K. Ochi. *Effects of Hydrogen-Oxygen Torch Igniter Combustion Applied to an ABS/GOx Hybrid Rocket System*. 2022.

[68] Frank M. White. *Fluid Mechanics, 8th Edition*. McGraw Hill Education, 2016.

[69] San Jose State University. *t-table*. URL: https://www.sjsu.edu/faculty/gerstman/StatPrimer/t-table.pdf.

Appendix A

Tabulated Data

Table A.1. Tabulated Data (Initial Fuel Port Radius, Nylon-6 Flow Rate, Regression Rate, Steady State Pressure, and Maximum Pressure) for All Runs

Run	r_i (mm)	$\dot{m}_{Nylon-6}$ (g/sec)	$\dot{r}$ (cm/sec)	P_{ss} (kPa)	P_{max} (kPa)
A-1	12.81	3.65	0.01142	437.7	510.8
A-2	12.76	3.78	0.01186	429.8	508.4
A-3	12.93	3.81	0.01181	454.1	526.4
A-4	13.27	3.31	0.01007	422.6	503.3
E-1	18.42	3.29	0.00734	413.3	557.2
E-2	18.44	3.38	0.00753	329.1	567.0
E-3	18.28	3.31	0.00744	427.5	541.4
E-4	18.25	3.17	0.00710	401.3	535.4
F-1	21.36	3.02	0.00584	388.5	443.3
F-2	23.00	2.75	0.00496	369.6	486.7
F-3	24.64	2.74	0.00462	368.2	463.1
G-1	20.68	3.17	0.00633	388.5	542.0
G-2	23.05	3.07	0.00552	377.2	541.9
G-3	24.32	3.08	0.00525	378.6	535.5
H-1	21.46	2.63	0.00508	397.8	510.7
H-2	22.75	2.82	0.00514	366.7	518.8
H-3	24.23	2.60	0.00446	366.9	473.8

Table A.2. Tabulated Data (Steady State c*, Maximum c*, Rising Portion Time Constant, Falling Portion Time Constant, Ignition Delay) for All Runs

Run	c^*_{ss} (m/sec)	c^*_{max} (m/sec)	τ_r (sec)	τ_f (sec)	t_{ig} (sec)
A-1	1123.8	1256.6	1.17	0.41	0.085
A-2	1103.7	1271.5	1.22	0.55	0.160
A-3	1137.8	1289.2	1.15	0.39	0.155
A-4	1101.0	1253.1	1.08	0.53	0.175
E-1	997.8	1335.4	1.21	0.55	0.095
E-2	1071.7	1577.8	1.12	0.53	0.165
E-3	1089.1	1343.7	1.22	0.35	0.320
E-4	1048.4	1355.3	1.17	0.55	0.175
F-1	1008.0	1071.6	1.56	1.04	0.770
F-2	957.1	1163.9	1.54	0.59	0.270
F-3	986.0	1159.7	1.37	0.96	0.650
G-1	995.7	1330.8	1.28	0.57	0.190
G-2	957.1	1315.4	1.25	0.59	0.200
G-3	968.6	1311.0	1.35	0.57	0.245
H-1	1050.9	1232.7	1.30	0.94	0.370
H-2	947.5	1235.1	1.47	0.93	0.180
H-3	961.4	1124.8	1.19	0.91	0.855

Appendix B

All Pressure Plots

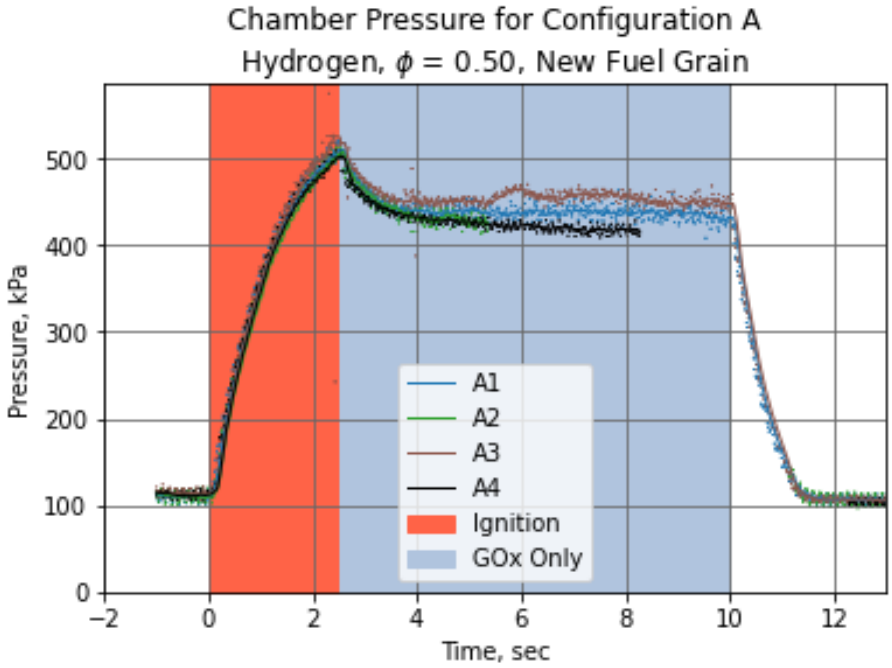

Figure B.1. Pressure for All 'A' Configuration Runs

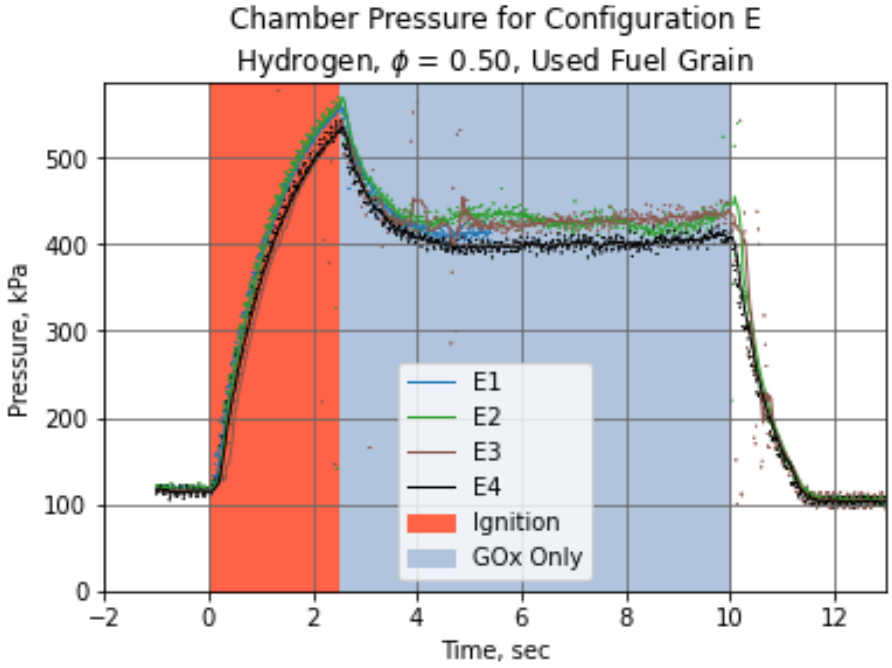

Figure B.2. Pressure for All 'E' Configuration Runs

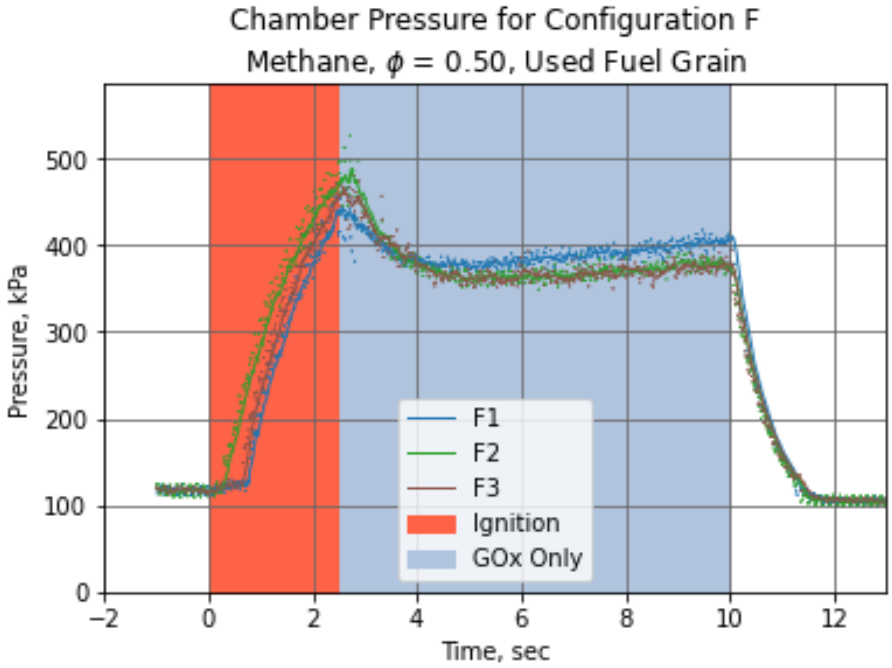

Figure B.3. Pressure for All 'F' Configuration Runs

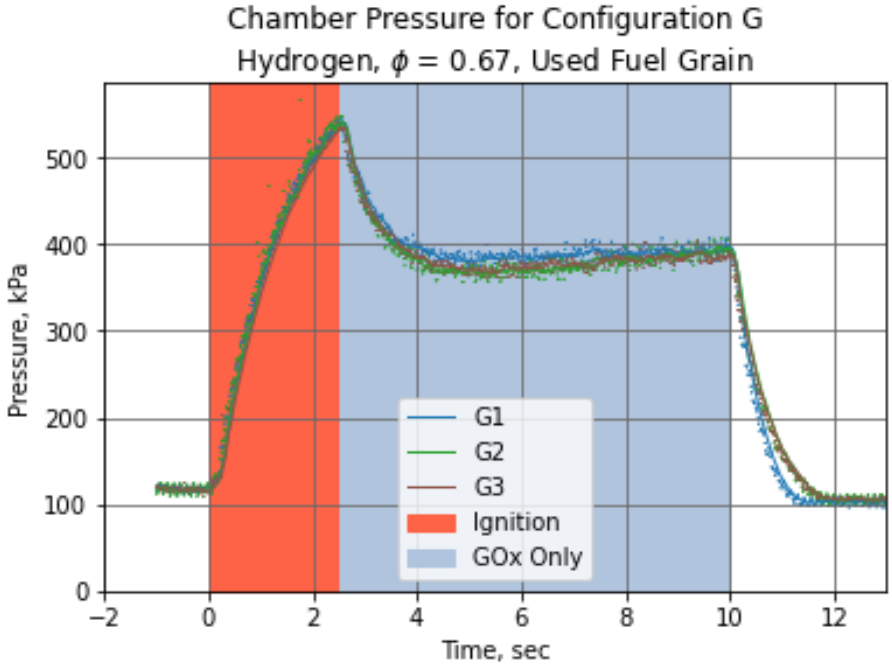

Figure B.4. Pressure for All 'G' Configuration Runs

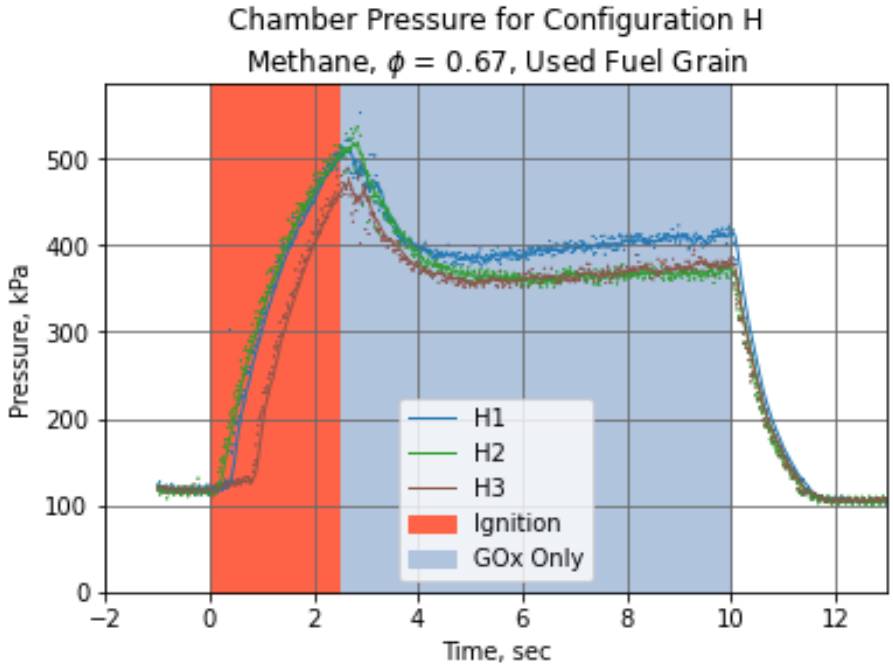

Figure B.5. Pressure for All 'H' Configuration Runs

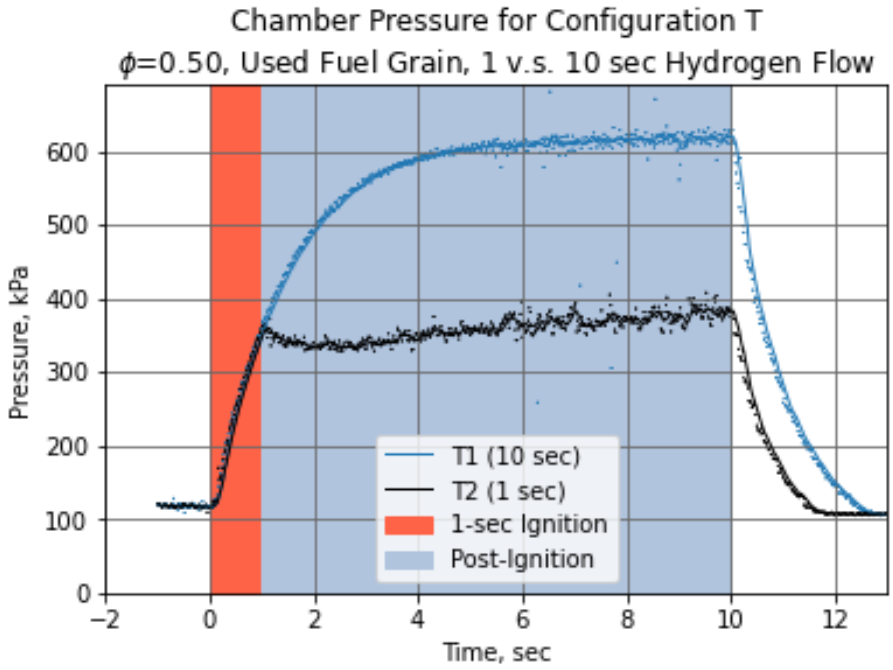

Figure B.6. Chamber Pressure for Both 'T' Configuration Runs (Hydrogen Flow Time Study)

Appendix C

Pressure Transducer Data Sheet

HIGH-ACCURACY FULL BRIDGE OUTPUT PRESSURE TRANSDUCER

0-10 to 0-7500 psi
0-0.70 to 0-517 bar

PX931 Series

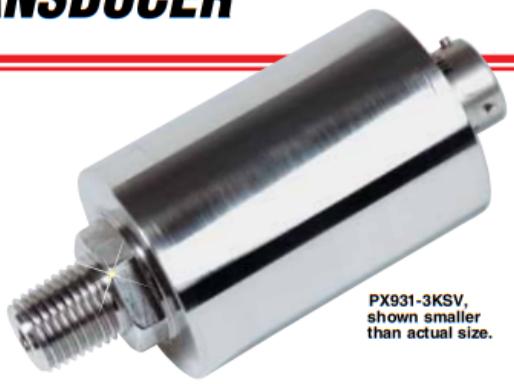

PX931-3KSV, shown smaller than actual size.

- **Rugged Stainless Steel Case Protects Components in Industrial Environments**
- **Connects to a PT06F10-6S-R Connector for Easy Field Connections**
- **Stainless Steel Diaphragm Welded for Compatibility with Most Media**
- **Uses a Standard 10 Vdc Regulated Power Supply for Maximum Versatility**
- **¼ NPT Process Fitting for Fast, Easy, and Secure Installation**
- **Excellent Temperature Stability**
- **Units 100 psi and Below are Vented Gage for High Precision**

SPECIFICATIONS

Excitation: 10 Vdc (15 Vdc max) @ 30 mA
Output: 30 mV ±0.25% @ 10 Vdc
Sensitivity: 3 mV/V
Input Impedance: 350 Ω min
Output Resistance: 350 ±5 Ω
Insulation Resistance: >5 MΩ @ 75 Vdc
Accuracy: 0.15%
Hysteresis: ±0.10%
Repeatability: ±0.05%
Zero Balance: ±1.0%
Shunt Calibration: 59 kΩ
Operating Temperature Range: -73 to 163°C (-100 to 325°F)
Compensated Temperature Range: 16 to 71°C (60 to 160°F)

Thermal Zero Effect: ±0.005% FS/°F
Thermal Sensitivity Effect: ±0.005% rdg/°F
Proof Pressure: 150% of range
Burst Pressure: 300% of range
Body Material: 17-4 PH stainless steel, hermetically sealed
Diaphragm Material: 17-4 PH SS

Pressure Port: ¼-18 NPT
Male Thread: 10 to 1000 psi
Female Thread: 3000 to 7500 psi
Mating Connector PT06F10-6S-R (not included)
Pressure Cavity Volume: 0.171 in³
Weight: 290 g (10 oz)

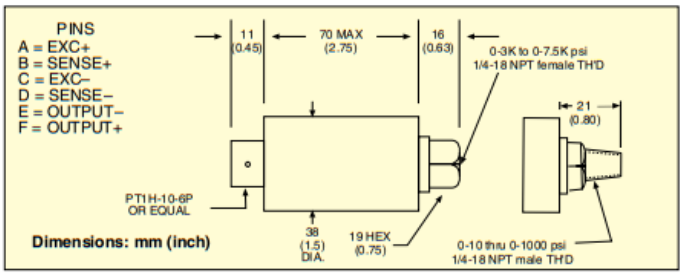

To Order

RANGE		MODEL NO.	COMPATIBLE METERS*
0 to 10 psi	0 to 0.69 bar	**PX931-010GV**	DP41-S, DP25B-S, DP3002-S
0 to 25 psi	0 to 1.72 bar	**PX931-025GV**	DP41-S, DP25B-S, DP3002-S
0 to 50 psi	0 to 3.4 bar	**PX931-050GV**	DP41-S, DP25B-S, DP87
0 to 100 psi	0 to 6.9 bar	**PX931-100SV**	DP41-S, DP25B-S, DP87
0 to 200 psi	0 to 13.8 bar	**PX931-200SV**	DP41-S, DP25B-S, DP3002-S
0 to 500 psi	0 to 34.5 bar	**PX931-500SV**	DP41-S, DP25B-S, DP87
0 to 1000 psi	0 to 68.9 bar	**PX931-1KSV**	DP41-S, DP25B-S, DP87
0 to 3000 psi	0 to 207 bar	**PX931-3KSV**	DP41-S, DP25B-S, DP41-S
0 to 5000 psi	0 to 345 bar	**PX931-5KSV**	DP41-S, DP25B-S,DP87
0 to 7500 psi	0 to 517 bar	**PX931-7.5KSV**	DP41-S, DP25B-S, DP87

Comes with 5-point calibration.
** Visit us online for compatible meters.*
*Absolute ranges available. Change **"G"** to **"A"** in model number, for additional cost.*
***Ordering Examples: PX931-500SV,** 500 psi sealed gage pressure transducer. **PX931-025GV,** 25 psi gage pressure transducer. **PT06F10-6S-R,** mating connector (sold separately).*

Appendix D

Compression Load Cell Data Sheet

25.4 mm (1") DIAMETER STAINLESS STEEL COMPRESSION LOAD CELL

STANDARD AND METRIC MODELS

OMEGA™

Compression
0-100 lb to 0-10,000 lb
0-500 to 0-50,000 N

1 Newton = 0.2248 lb
1 daNewton = 10 Newtons
1 lb = 454 g
1 t = 1000 kg = 2204 lb

LC304/LCM304 Series

NIST RoHS
Standard

- **Heavy-Duty Design**
- **Built-In Load Button for Easy Installation**
- **Miniature 25 mm (1") Diameter and 25 mm (1") High Case**
- **5-Point Calibration Provided**

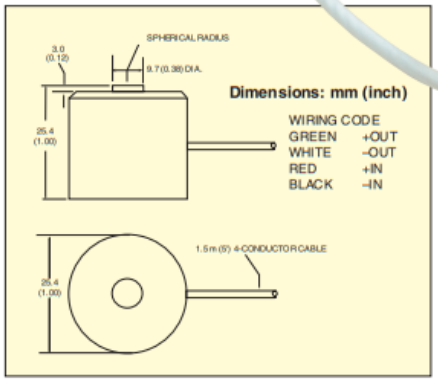

LC304-1K,
shown actual size.

OMEGA's LC304/LCM304 Series load cells offer the highest output of all miniature load cells. Their small 25 mm (1") diameter makes it easy to mount them in a pocket or on a flat surface. The rugged stainless steel case and high-quality construction ensure reliability.

Deflection: 0.025 to 0.076 mm (0.001 to 0.003")
Protection Class: IP65
Safe Overload: 150% of capacity
Ultimate Overload: 300% of capacity

Bridge Resistance: 350 Ω minimum
Construction: Stainless steel
Electrical: 1.5 m (5') 4-conductor cable

STANDARD MODELS

To Order

CAPACITY		MODEL NO.	COMPATIBLE METERS
lb	N		
100	445	**LC304-100**	iSeries, DP41-S, DP25B-S
500	2224	**LC304-500**	iSeries, DP41-S, DP25B-S
1000	4448	**LC304-1K**	iSeries, DP41-S, DP25B-S
3000	13,345	**LC304-3K**	iSeries, DP41-S, DP25B-S
5000	22,242	**LC304-5K**	iSeries, DP41-S, DP25B-S
7500	33,363	**LC304-7.5K**	iSeries, DP41-S, DP25B-S
10,000	44,484	**LC304-10K**	iSeries, DP41-S, DP25B-S

SPECIFICATIONS

Excitation: 10 Vdc, 15 Vdc maximum
Output: 2 mV/V nominal
Accuracy: ±0.5% FSO linearity, hysteresis, repeatability combined
5-Point Calibration:
0%, 50%, 100%, 50%,0%
Zero Balance: ±2% FSO
Operating Temp Range:
-54 to 107°C (-65 to 225°F)
Compensated Temp Range:
16 to 71°C (60 to 160°F)
Thermal Effects:
Zero: 0.009% FSO/°C
Span: 0.036% FSO/°C

METRIC MODELS

CAPACITY		MODEL NO.	COMPATIBLE METERS
N	lb		
500	112	**LCM304-500N**	DP41-S, DP25B-S, iSeries
2000	450	**LCM304-2KN**	DP41-S, DP25B-S, iSeries
5000	1124	**LCM304-5KN**	DP41-S, DP25B-S, iSeries
10,000	2248	**LCM304-10KN**	DP41-S, DP25B-S, iSeries
20,000	4496	**LCM304-20KN**	DP41-S, DP25B-S, iSeries
50,000	11,240	**LCM304-50KN**	DP41-S, DP25B-S, iSeries

Comes complete with 5-point NIST-traceable calibration and 59 kΩ shunt data.
Ordering Examples: LC304-100, *100 lb capacity load cell.*
LC304-5K, *5000 lb capacity load cell.*
LCM304-5KN, *5000 N capacity load cell.*

Appendix E

Selected Pages of Flow Meter Data Sheet

⚠ CAUTION: WIRING THE GFM METER WITH THE POWER ON MAY RESULT IN INTERNAL DAMAGE! PLEASE MAKE ALL WIRING CONNECTIONS BEFORE SWITCHING ON THE POWER.

All GFM models require power supplies with nominal current rating of at least 200 mA. The operating power input is supplied via the DC power jack or the 9-pin "D" connector located at the side of the flow transducer enclosure. On GFM's pur-chased without an LCD readout, a readout panel meter, digital multimeter, or other equivalent device is required to observe the flow signal.

Based on the GFM transducer's serial number it may require a different power sup-ply voltage. GFM flow meters with serial numbers below 340621-1 may require 12 or 24 Vdc power supplies. Before connecting power supply check the meter power supply requirements label located on the flow meter back cover. If the power supply requirements label states that the power supply requirement is 12 Vdc, do not connect power supply with voltage above 15 Vdc. Exceeding spec-ified maximum power supply voltage limit will result in device permanent damage.

The GFM flow meters with serial numbers above 340621-1 have universal power input and can be used with any power supply voltage between +12 and +26 Vdc.

⚠ CAUTION: BEFORE CONNECTING POWER SUPPLY CHECK YOUR METER SERIAL NUMBER AND POWER SUPPLY REQUREMENTS LABEL LOCATED ON THE FLOW METER BACK COVER. DO NOT CONNECT 24Vdc POWER SUPPLY UNLESS YOUR GFM METER WAS ORDERED AND CONFIGURED FOR 24Vdc. EXCEEDING SPECIFIED MAXIMUM POWER SUPPLY VOLTAGE LIMIT MAY RESULT IN DEVICE PERMANENT DAMAGE.

PIN FUNCTION

1	Remote LCD display signal
2	0 to 5 VDC output indication
3	0 to 5 VDC common
4	Power supply, positive
5	Power supply, common
6	Remote LCD display reference
7	(unassigned)
8	4 to 20 mA output indication self-powered (sourcing type, non-isolated)
9	4 to 20 mA common (return)

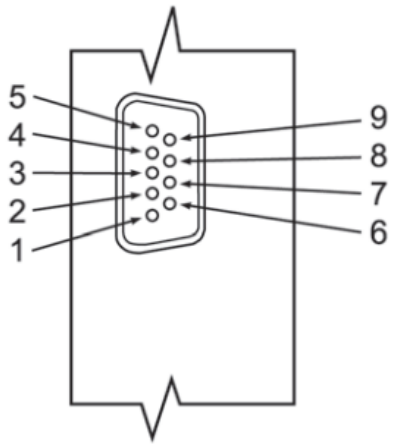

FIGURE 2.a - 9-PIN "D" CONNECTOR PINOUTS FOR GFM TRANSDUCER.

4. SPECIFICATIONS

FLOW MEDIUM: Please note that GFM17/37/47/57/67/77 Mass Flow Meters are designed to work with clean gases only. Never try to meter or control flow rates of liquids with any GFM's.

CALIBRATIONS: Performed at standard conditions [14.7 psia (1.01 bars) and 70 °F (21.1 °C)] unless otherwise requested or stated.

ENVIRONMENTAL (per IEC 664): Installation Level II; Pollution Degree II.

ACCURACY: GFM 17, 37, 47 ±1.0% F.S.
GFM 57, 67, 77 ±1.5% F.S.

REPEATABILITY: ±0.25% of full scale.

TEMPERATURE COEFFICIENT: 0.15% of full scale/ °C.

PRESSURE COEFFICIENT: 0.01% of full scale/psi (0.07 bar).

RESPONSE TIME: 800 ms time constant; approximately 2 seconds to within ±2% of set flow rate for 25% to 100% of full scale flow rate.

GAS PRESSURE: 1000 psig (69 bars) GFM 17, 37 and 47; 500 psig (34.5 bars) GFM 57, 67 and 77. Optimum pressure is 20 psig (1.4 bars).

GAS AND AMBIENT TEMPERATURE: 32 °F to 122 °F (0 °C to 50 °C).
14 °F to 122 °F (-10 °C to 50 °C) - Dry gases only.

RELATIVE GAS HUMIDITY: Up to 70%.

LEAK INTEGRITY: 1 x 10^{-9} sccs He max. to the outside environment.

ATTITUDE SENSITIVITY: No greater than ±15 degree rotation from horizontal. Standard calibration is in horizontal position.

OUTPUT SIGNALS: Linear 0-5 VDC (1000 Ω minimum load impedance) and 4-20 mA self-powered sourcing type, non-isolated (0-500 loop Ω resistance); 20 mV peak to peak max noise.

Contact your distributor or Aalborg® for optional RS232 or RS-485 interfaces.

TRANSDUCER INPUT POWER:

GFM models with 12 VDC power input (serial numbers below 340621-1):
12 VDC, 200 mA maximum;
GFM models with 24 VDC power input (serial numbers below 340621-1):
+24 VDC, 200 mA maximum;
GFM models with universal power input (serial numbers above 340621-1):
any voltage between +12 and +26 VDC, 200 mA maximum;

Power input is protected by a 750 mA (GFM models with serial numbers below 340621-1) or 300 mA (GFM models with serial numbers above 340621-1) M (medium time-lag) resettable fuse, and a rectifier diode for polarity protection.

WETTED MATERIALS:

GFM17/37/47/57/67/77: Anodized aluminum, brass, and 316 stainless steel with VITON® O-rings seals; BUNA®, EPR or KALREZ® O-rings are optional.

GFM17S/37S/47S/57S/67S/77S: 316 stainless steel with VITON® O-rings seals; BUNA®, EPR or KALREZ® O-rings are optional.

Aalborg® makes no expressed or implied guarantees of corrosion resistance of mass flow meters as pertains to different flow media reacting with components of meters. It is the customers' sole responsibility to select the model suitable for a particular gas based on the fluid contacting (wetted) materials offered in the different models.

INLET AND OUTLET CONNECTIONS:

GFM 17 and 37:	1/4" compression fittings. Optional: 6mm compression, 1/4" VCR®, 3/8" or 1/8" compression fittings (GFM 17).
GFM 47:	3/8" compression fittings.
GFM 57:	3/8" compression fittings.
GFM 67:	1/2" compression fittings.
GFM 77:	3/4" FNPT fittings or 3/4" compression fittings.

LCD DISPLAY: 3½ digit LCD (maximum viewable digits "1999"), 0.5 inch high characters. On GFM171/371/471/571/671/771 aluminum or stainless steel models the LCD display is built into the upper block element and may be tilted over 90 degrees for optimal viewing comfort. Remote or panel mounting remote reading is optional.

Standard readings are in direct engineering units for the given gas and flow rate (i.e. liters/minute [slpm], standard cubic centimeters/minute [sccm], standard cubic feet/hour [scfh], etc.). 0 to 100% LCD calibration scaling is available upon request at time of order. Contact your distributor or Aalborg® when non-standard display settings are desired.

TRANSDUCER INTERFACE CABLE: Optional shielded cable is available mating to the GFM transducer 9-pin "D" connector. In order to operate flow meter within the specification the cable length for analog 0-5 Vdc output and remote LCD display may not exceed 9.5 feet (3 meters).

4.1 CE Compliance

Any model GFM bearing a CE marking on it, is in compliance with the below stated test standards currently accepted.

EMC Compliance with 89/336/EEC as amended; Emission Standard: EN 55011:1991, Group 1, Class B Immunity Standard: EN 55082-2:1992.

FLOW RANGES

TABLE I GFM 17
LOW FLOW
MASS FLOW METER*

CODE	mL/min [N_2]
01	0 to 10
02	0 to 20
03	0 to 50
04	0 to 100
05	0 to 200
06	0 to 500
CODE	**L/min [N_2]**
07	0 to 1
08	0 to 2
09	0 to 5
10	0 to 10

* Flow rates are stated for Nitrogen at STP conditions [i.e. 70 °F (21.1 °C) at 1 atm].

For other gases use the K factor as a multiplier from APPENDIX 2.

TABLE II GFM 37
MEDIUM FLOW
MASS FLOW METER*

CODE	L/min [N_2]
11	0 to 15
30	20
31	30
32	40
33	50

TABLE III GFM 47
HIGH FLOW
MASS FLOW METER*

CODE	L/min [N_2]
40	60
41	80
42	100
50	200
60	500
70	1000

TABLE IV PRESSURE DROPS

MODEL	FLOW RATE [L/min]	MAXIMUM PRESSURE DROP		
		[mm H_2O]	[psid]	[mbar]
GFM 17	up to 10	58	0.083	5.7
GFM 37	15	63	0.09	6.4
	20	300	0.44	30
	30	800	1.18	81
	40	1480	2.18	150
	50	2200	3.23	223
GFM 47	60	3100	4.56	314
	100	5500	8.08	557
GFM 57	200	2720	4.0	280
GFM 67	500	3400	5.0	340
GFM 77	1000	6120	9.0	620

9. CALIBRATION CONVERSIONS FROM REFERENCE GASES

The calibration conversion incorporates the K factor. The K factor is derived from gas density and coefficient of specific heat. For diatomic gases:

$$K_{gas} = \frac{1}{d \times C_p}$$

where d = gas density (gram/liter)
C_p = coefficient of specific heat (cal/gram)

Note in the above relationship that d and Cp are usually chosen at the same conditions (standard, normal or other).

If the flow range of a Mass Flow Meter remains unchanged, a relative K factor is used to relate the calibration of the actual gas to the reference gas.

$$K = \frac{Q_a}{Q_r} = \frac{K_a}{K_r}$$

where Q_a = mass flow rate of an actual gas (sccm)
Q_r = mass flow rate of a reference gas (sccm)
K_a = K factor of an actual gas
K_r = K factor of a reference gas

For example, if we want to know the flow rate of oxygen and wish to calibrate with nitrogen at 1000 SCCM, the flow rate of oxygen is:

$$Q_{O2} = Q_a = Q_r \times K = 1000 \times 0.9926 = 992.6 \text{ sccm}$$

where K = relative K factor to reference gas (oxygen to nitrogen)

ACTUAL GAS	K FACTOR Relative to N_2	Cp [Cal/g]	Density [g/l]
Deuterium D_2	1.00	1.722	1.799
Diborane B_2H_6	.4357	.508	1.235
Dibromodifluoromethane CBr_2F_2	.1947	.15	9.362
Dichlorodifluoromethane (Freon-12) CCl_2F_2	.3538	.1432	5.395
Dichlofluoromethane (Freon-21) $CHCl_2F$	.4252	.140	4.592
Dichloromethylsilane $(CH_3)_2SiCl_2$	.2522	.1882	5.758
Dichlorosilane SiH_2Cl_2	.4044	.150	4.506
Dichlorotetrafluoroethane (Freon-114) $C_2Cl_2F_4$	.2235	.1604	7.626
1,1-Difluoroethylene (Freon-1132A) $C_2H_2F_2$	.4271	.224	2.857
Dimethylamine $(CH_3)_2NH$	.3714	.366	2.011
Dimethyl Ether $(CH_3)_2O$	.3896	.3414	2.055
2,2-Dimethylpropane C_3H_{12}	.2170	.3914	3.219
Ethane C_2H_6	.50	.420	1.342
Ethanol C_2H_6O	.3918	.3395	2.055
Ethyl Acetylene C_4H_6	.3225	.3513	2.413
Ethyl Chloride C_2H_5Cl	.3891	.244	2.879
Ethylene C_2H_4	.60	.365	1.251
Ethylene Oxide C_2H_4O	.5191	.268	1.965
Fluorine F_2	.9784	.1873	1.695
Fluoroform (Freon-23) CHF_3	.4967	.176	3.127
Freon-11 CCl_3F	.3287	.1357	6.129
Freon-12 CCl_2F_2	.3538	.1432	5.395
Freon-13 $CClF_3$	.3834	.153	4.660
Freon-13B1 $CBrF_3$	.3697	.1113	6.644
Freon-14 CF_4	.4210	.1654	3.926
Freon-21 $CHCl_2F$	.4252	.140	4.592
Freon-22 $CHClF_2$	.4589	.1544	3.858
Freon-113 CCl_2FCClF_2	.2031	.161	8.360
Freon-114 $C_2Cl_2F_4$	.2240	.160	7.626
Freon-115 C_2ClF_5	.2418	.164	6.892
Freon-C318 C_4F_8	.1760	.185	8.397
Germane GeH_4	.5696	.1404	3.418
Germanium Tetrachloride $GeCl_4$	.2668	.1071	9.565
Helium He	1.454	1.241	.1786
Helium He-1 (>50 L/min)	2.43	1.241	.1786
Helium He-2 (>10-50 L/min)	2.05	1.241	.1786
Hexafluoroethane C_2F_6 (Freon-116)	.2421	.1834	6.157
Hexane C_6H_{14}	.1792	.3968	3.845
Hydrogen H_2-1	1.0106	3.419	.0899
Hydrogen H_2-2 (>10-100 L)	1.35	3.419	.0899
Hydrogen H_2-3 (>100 L)	1.9	3.419	.0899

ACTUAL GAS	K FACTOR Relative to N_2	Cp [Cal/g]	Density [g/l]
Hydrogen Bromide HBr	1.000	.0861	3.610
Hydrogen Chloride HCl	1.000	.1912	1.627
Hydrogen Cyanide HCN	.764	.3171	1.206
Hydrogen Fluoride HF	.9998	.3479	.893
Hydrogen Iodide HI	.9987	.0545	5.707
Hydrogen Selenide H_2Se	.7893	.1025	3.613
Hydrogen Sulfide H_2S	.80	.2397	1.520
Iodine Pentafluoride IF_5	.2492	.1108	9.90
Isobutane $CH(CH_3)_3$	.27	.3872	3.593
Isobutylene C_4H_8	.2951	.3701	2.503
Krypton Kr	1.453	.0593	3.739
Methane CH_4 Methane CH_4-1 (>10 L/min)	.7175 .75	.5328 .5328	.715 .715
Methanol CH_3	.5843	.3274	1.429
Methyl Acetylene C_3H_4	.4313	.3547	1.787
Methyl Bromide CH_3Br	.5835	.1106	4.236
Methyl Chloride CH_3Cl	.6299	.1926	2.253
Methyl Fluoride CH_3F	.68	.3221	1.518
Methyl Mercaptan CH_3SH	.5180	.2459	2.146
Methyl Trichlorosilane $(CH_3)SiCl_3$	.2499	.164	6.669
Molybdenum Hexafluoride MoF_6	.2126	.1373	9.366
Monoethylamine $C_2H_5NH_2$	.3512	.387	2.011
Monomethylamine CH_3NH_2	.51	.4343	1.386
Neon NE	1.46	.246	.900
Nitric Oxide NO	.990	.2328	1.339
Nitrogen N_2	1.000	.2485	1.25
Nitrogen Dioxide NO_2	.737	.1933	2.052
Nitrogen Trifluoride NF_3	.4802	.1797	3.168
Nitrosyl Chloride NOCl	.6134	.1632	2.920
Nitrous Oxide N_2O	.7128	.2088	1.964
Octafluorocyclobutane (Freon-C318) C_4F_8	.176	.185	8.397
Oxygen O_2	.9926	.2193	1.427
Oxygen Difluoride OF_2	.6337	.1917	2.406
Ozone	.446	.195	2.144
Pentaborane B_5H_9	.2554	.38	2.816
Pentane C_5H_{12}	.2134	.398	3.219
Perchloryl Fluoride ClO_3F	.3950	.1514	4.571
Perfluoropropane C_3F_8	.174	.197	8.388
Phosgene $COCl_2$	.4438	.1394	4.418
Phosphine PH_3	.759	.2374	1.517

Appendix F

Data Acquisition Program

```
// Include Required Libraries
#include <Adafruit_ADS1X15.h>
#include <Wire.h>

// Define/Initialize Variables
const byte trigger_pin_on  = 2;        //Pin D2 used to trigger
                                       //start of logging
                                       //operation
volatile int m_sec   = -10000;         //Counter for
                                       //milliseconds
                                       //passed initialized to
                                       // -10sec

int16_t force_dig = 1;    //Digital integer input from A0/A1
                          //ports on Adafryit ADS1115 for foce
                          //transducer
int16_t press_dig = 1;    //Digital integer input from A2/A3
                          //ports on Adafruit ADS1115 for
                          //pressure transducer
int     flow_o_dig = 0;   //Digital integer input from A1 port
                          //on Arduino board for first flow
                          //meter
int     flow_h_dig = 0;   //Digital integer input from A3 port
                          //on Arduino board for second flow
                          //meter


Adafruit_ADS1115 ads1115;
```

```
void setup() {
// Stop interrupts
noInterrupts();
cli();

// Set Up Timer 1 to 200Hz based on ATMega328 Microprocessor
  TCCR1A = 0; // set entire TCCR1A register to 0
  TCCR1B = 0; // set entire TCCR1B register to 0

  TCNT1 = 0;  // initialize counter register to 0

  OCR1A = 9999;  // set compare match register for 200 Hz
                 // increments when TCNT1 == OCR1A interrupt is
                 // triggered

  TCCR1B |= (1<<WGM12); // Turn on CTC mode

  TCCR1B |= (1<< CS11); // Set 8 prescaler

  TIMSK1 |= (1<<OCIE1A); // enable timer compare interrupt


attachInterrupt(digitalPinToInterrupt(trigger_pin_on), dtarst,
  RISING);

// Resume interrupts
sei();
interrupts();
```

```
Serial.begin(115200);
ads1115.begin();

//Set gain to 16 to amplify transduer sugnals
ads1115.setGain(GAIN_SIXTEEN);

//Set trigger pin to input mode to read digital value
pinMode(trigger_pin_on, INPUT);

}


ISR(TIMER1_COMPA_vect){
  //occurs every 5 milliseconds for effective
  //sampling rate of 200Hz
  Serial.print(m_sec);
  Serial.print(",");
  Serial.print(force_dig);
  Serial.print(",");
  Serial.print(press_dig);
  Serial.print(",");
  Serial.print(flow_o_dig);
  Serial.print(",");
  Serial.println(flow_h_dig);
  m_sec += 5;
}

void loop() {
  force_dig = ads1115.readADC_SingleEnded(0);
```

```
  press_dig = ads1115.readADC_Differential_2_3();
  flow_o_dig = analogRead(A1);
  flow_h_dig = analogRead(A3);
}

void dtarst() {
  delayMicroseconds(4000); //wait 4 milliseconds
  if(digitalRead(trigger_pin_on)){//when trigger pin is set to
    // HIGH print data log header
    Serial.println("\nMSEC,FRCE,PRES,MFMO,MFMF");
    m_sec = -1995;
  }
  else {
    // don't run interrupt service request
  }
}
```

Appendix G

Solenoid Valve Timing and Control Program

```
// Define/Initialize Variables
int hydrogen = 13;      //H2 valve control signal will come from
                        //digital pin D13 (red)
int oxygen = 12;        //O2 valve control signal will come from
                        //digital pin D12 (blue)
int nitrogen = 11;      //N2 valve control signal will come from
                        //digital pin D11 (yellow)
int comm_pin = 5;       //Signal start to data logging signal
                        //will come from digital pin D5
int msfr_pin = 3;       //Signal to indicate misfire will be
                        //received by digital pin D3
int n2_ctrl  = 2;       //Signal to control n2 valve will be
                        //recieved by pin digital D2
int m_sec    = -10000;  //Counter for milliseconds passed
                        //initialized to absolute value of
                        //initial delay
int o_dlay   = -2000;   //Negative value of number of
                        //milliseconds to open oxygen valve and
                        //start data logging before run
                        //starts (hydrogen valve open)
int h_on_time = 2000;   //specify number of milliseconds hydrogen
                        //valve will be open (increment of 5
                        //milliseconds)
                        //Value will change based on current run
                        //configuration


int total_run_time = 10000; //specify number of milliseconds
                            //oxygen valve will be open which is
                            //the total burn time
```

```
int n_time_on   = 10000;      //specify nymber of milliseconds
                              //nitrogen valve will be open to
                              //purge the system
bool cycl_flag = false;       //Flag indicator to not let the
                              //m_sec value restart count and
                              //commence solenoid control sequence
                              //again

void setup() {
// Stop interrupts
cli();

// Set Up Timer 1 to 200Hz
  TCCR1A = 0; // set entire TCCR1A register to 0
  TCCR1B = 0; // set entire TCCR1B register to 0

  TCNT1 = 0;  // initialize counter register to 0

  OCR1A = 9999;  // set compare match register for 200HZ
                 // increments when TCNT1 == OCR1A interrupt is
                 // triggered

  TCCR1B |= (1<<WGM12); // Turn on CTC mode

  TCCR1B |= (1<< CS11); // Set 8 prescaler

  TIMSK1 |= (1<<OCIE1A); // enable timer compare interrupt

// Resume interrupts
```

```
sei();

pinMode(nitrogen, OUTPUT);
pinMode(hydrogen, OUTPUT);
pinMode(oxygen, OUTPUT);
pinMode(comm_pin, OUTPUT);

pinMode(msfr_pin, INPUT);
pinMode(n2_ctrl, INPUT);

digitalWrite(nitrogen, LOW);
digitalWrite(hydrogen, LOW);
digitalWrite(oxygen, LOW);
digitalWrite(comm_pin, LOW);

Serial.begin(115200);
}

ISR(TIMER1_COMPA_vect){ //occurs every .001 second
  Serial.println(m_sec);
  m_sec += 5;
}

void loop() {
  if (digitalRead(msfr_pin) == HIGH) {
    //E-STOP sequence
    //First turn off all propellant valves
    digitalWrite(hydrogen, LOW);
    digitalWrite(oxygen, LOW);
```

```
    digitalWrite(comm_pin, LOW);
    delay(500);
    //Purge system with Nitrogen
    digitalWrite(nitrogen, HIGH);
    delay(5000);
    //Exit timer cycle and go to manual control mode
    cycl_flag = true;
  }
  else {
    //do nothing
  }

  if (m_sec == o_dlay){
    digitalWrite(comm_pin, HIGH);   //sends signal to trigger
                                    //start of data logging at
                                    //t - dlay
    digitalWrite(oxygen, HIGH);     //open oxygen valve at
                                    //t - o_dlay sec;
  }
  else if(m_sec == 0){
    digitalWrite(hydrogen, HIGH);    //open hydrogen valve at
                                     //t = 0 sec;
  }
  else if(m_sec == h_on_time){
    digitalWrite(hydrogen, LOW);     //close hydrogen valve at
                                     //t + h_time_on
                                     //change this value on line
                                     //21 of code
  }
```

```
else if(m_sec == total_run_time){
  digitalWrite(oxygen, LOW);        //close oxygen valve at
                                    //t + total_run_time
                                    //this value should not
                                    //change
  digitalWrite(comm_pin, LOW);      //turn off communication pin
                                    //to prevent premature
                                    //inititalization of data
                                    //log start caused by event
                                    //interrupt
  digitalWrite(nitrogen, HIGH);     //open nitorgen valve at
                                    //t + total_run_time to
                                    //purge the system
}
else if(m_sec == (total_run_time + n_time_on)){
  digitalWrite(nitrogen, LOW);//close nitrogen valve at
                              //t + total_run_time + n_time_on
  cycl_flag = true;
}
else{// do nothing
}
while (cycl_flag == true){ //once one cycle is finished
                           //the program will enter this
                           //infinite loop so the valves do
                           //not open again
  while (digitalRead(n2_ctrl) == HIGH){
    digitalWrite(nitrogen, HIGH);
  }
  digitalWrite(nitrogen, LOW)}};
```